



HAL
open science

Multiscale modeling of ice deformation behavior

Maurine Montagnat, O. Castelnau, P. D. Bons, S.H. Faria, O. Gagliardini, F. Gillet-Chaulet, Fanny Grennerat, A. Griera, Ricardo A. Lebensohn, Hervé Moulinec, et al.

► **To cite this version:**

Maurine Montagnat, O. Castelnau, P. D. Bons, S.H. Faria, O. Gagliardini, et al.. Multi-scale modeling of ice deformation behavior. *Journal of Structural Geology*, 2014, 61, pp.78-108. 10.1016/j.jsg.2013.05.002 . hal-00904919

HAL Id: hal-00904919

<https://hal.science/hal-00904919>

Submitted on 1 Dec 2013

HAL is a multi-disciplinary open access archive for the deposit and dissemination of scientific research documents, whether they are published or not. The documents may come from teaching and research institutions in France or abroad, or from public or private research centers.

L'archive ouverte pluridisciplinaire **HAL**, est destinée au dépôt et à la diffusion de documents scientifiques de niveau recherche, publiés ou non, émanant des établissements d'enseignement et de recherche français ou étrangers, des laboratoires publics ou privés.

Multiscale modeling of ice deformation behavior

M. Montagnat^a, O. Castelnau^b, P. D. Bons^c, S. H. Faria^{d,e}, O. Gagliardini^{a,i}, F. Gillet-Chaulet^a, F. Grennerat^a, A. Gierera^f, R. A. Lebensohn^g, H. Moulinec^h, J. Roessiger^c, P. Suquet^h

^a*Laboratoire de Glaciologie et Géophysique de l'Environnement, CNRS, UJF - Grenoble I, 38402 Saint-Martin d'Hères, France*

^b*Procédés et Ingénierie en Mécanique et Matériaux, CNRS, Arts & Métiers ParisTech, 151 Bd de l'hôpital, 75013 Paris, France*

^c*Department of Geosciences, Eberhard Karls University Tübingen, Wilhelmstr. 56, 72074 Tübingen, Germany.*

^d*Basque Centre for Climate Change (BC3), Alameda Urquijo 4, 48008 Bilbao, Spain*

^e*Ikerbasque, Basque Foundation for Science, 48011 Bilbao, Spain*

^f*Departament de Geologia, Universitat Autònoma de Barcelona, 08193 Bellaterra (Cerdanyola del V.), Spain*

^g*Los Alamos National Laboratory, MS G755, Los Alamos, NM 87545, USA*

^h*Laboratoire de Mécanique et d'Acoustique, CNRS, UPR 7051, 13402, Marseille cedex 20, France.*

ⁱ*Institut Universitaire de France (IUF), Paris, France*

Abstract

Understanding the flow of ice in glaciers and polar ice sheets is of increasing relevance in a time of potentially significant climate change. The flow of ice has hitherto received relatively little attention from the structural geological community. This paper aims to provide an overview of methods and results of ice deformation modeling from the single crystal to the polycrystal scale, and beyond to the scale of polar ice sheets. All through these scales, various models have been developed to understand, describe and predict the processes that operate during deformation of ice, with the aim to correctly represent ice rheology and self-induced anisotropy. Most of the modeling

Email address: montagnat@lgge.obs.ujf-grenoble.fr (M. Montagnat)

URL: <http://lgge.osug.fr/montagnat-rentier-maurine> (M. Montagnat)

tools presented in this paper originate from the material science community, and are currently used and further developed for other materials and environments. We will show that this community has deeply integrated ice as a very useful "model" material to develop and validate approaches in conditions of a highly anisotropic behavior. This review, by no means exhaustive, aims at providing an overview of methods at different scales and levels of complexity.

Keywords: ice mechanical behavior, multiscale modeling, viscoplastic anisotropy, fabric development

1	Contents	
2	1 Introduction	4
3	1.1 Mechanical properties of ductile ice	5
4	1.2 Main objectives	8
5	2 Modeling ice single crystal behavior	9
6	2.1 Dislocation Dynamics modeling	10
7	2.2 Field Dislocation Mechanics (FDM)	12
8	2.3 Crystal plasticity modeling	13
9	2.3.1 Data for elasticity	16
10	2.3.2 Data for basal slip	16
11	3 Mean field approaches for the mechanical response of ice	
12	polycrystals	18
13	3.1 Microstructure characterization	18
14	3.2 Linear thermo-elasticity	20
15	3.3 Reuss and Voigt approximations	22

16	3.4	The Self-Consistent (SC) scheme	23
17	3.5	Nonlinear viscoplasticity	25
18	3.5.1	Application to natural ices: effective behavior	29
19	3.5.2	Application to natural ices: texture development	32
20	3.6	Modeling the elasto-viscoplastic behavior	35
21	4	Full field approaches for the polycrystal	38
22	4.1	Viscoplastic approach - FFT	39
23	4.1.1	Viscoplastic FFT-based formulation	39
24	4.1.2	Application to columnar ice deforming in the secondary	
25		creep regime.	43
26	4.2	Elasto-viscoplastic FFT approach	47
27	4.2.1	The mechanical problem	48
28	4.2.2	Application to strain field prediction in a 2D-1/2 con-	
29		figuration.	50
30	5	Modeling of dynamic recrystallization mechanisms	52
31	5.1	Dynamic recrystallization within mean-field approaches	53
32	5.2	Dynamic recrystallization within full-field approaches	57
33	5.2.1	The Elle modeling platform	58
34	5.2.2	Coupling Elle platform to FFT approach	62
35	5.2.3	Application to creep experiments and natural ice	65
36	6	Toward large scale ice flow modeling	67
37	6.1	Continuous Diversity and the CAFFE model	69
38	6.2	GOLF law and Elmer/Ice	74
39	7	Synthesis and perspectives	79

41 **1. Introduction**

42 Ice is a common mineral on the Earth's surface, where it occurs as ice
43 Ih. As ice is relatively close to its melting temperature, glaciers and polar
44 ice sheets deform by ductile dislocation creep at strain rates in the order
45 of 10^{-12} to 10^{-6} s⁻¹. Research on the flow of ice is of direct importance
46 to society as it is needed to understand and predict the effects that global
47 warming could have on sea level rise, glacier retreat, etc. There is also an
48 increasing awareness that ice is a valuable analogue for other minerals and
49 crystalline materials, as it is the only common mineral where this creep can
50 be readily observed in nature and in the laboratory. Numerical modeling
51 has become a key method to link the mechanics of ice from the dislocation
52 scale to that of flowing ice masses.

53 Most of the efforts made to simulate the ductile mechanical behavior of
54 polycrystalline ice are related to the modeling of ice flow and fabric evolution
55 in the conditions of polar ice sheets or glaciers. Ice is increasingly considered
56 a model material to validate micro-macro mechanical approaches for mate-
57 rials with a high viscoplastic anisotropy. Most of the modeling techniques
58 presented in this paper are currently used or further developed for other
59 materials. For geological applications, one main limitation could be related
60 to the "one phase" approach for most of these techniques, well adapted to
61 ice. The reader will find, at the end of the paper, a table summarizing the
62 main aspects of each techniques, with application ranges and limitations.

63 *1.1. Mechanical properties of ductile ice*

64 Ice Ih has an hexagonal crystal structure with a c/a ratio of 1.628. This
65 c/a ratio is very close to the 1.633 value for a closely packed structure, but
66 ice is not closely packed (see Schulson and Duval (2009) for a recent review).
67 The elastic anisotropy of ice single crystals is small. The Young modulus E
68 only varies by about 30%, depending on the direction of the loading axis with
69 respect to the c -axis. The highest value is along the c -axis with $E = 11.8$
70 GPa at -16°C (Gammon et al., 1983).

71 Single crystals deform plastically essentially by glide of dislocations on
72 the basal plane. There are three equivalent $\langle 1\bar{2}10 \rangle$ directions for the
73 Burgers vector, but slip on the basal plane is almost isotropic. In conditions
74 where basal slip is favored, the stress-strain rate relationship after a strain of
75 about 5% can be expressed by a power law with a stress exponent $n = 2 \pm 0.3$
76 (Higashi et al., 1965; Jones and Glen, 1969; Mellor and Testa, 1969). At
77 similar strain rates, the equivalent stress requested for non-basal slip is about
78 60 times larger than for basal slip (Duval et al., 1983).

79 For ice polycrystals deformed under the laboratory conditions (strain rate
80 between about 10^{-8} s^{-1} and 10^{-6} s^{-1} and temperature generally higher
81 than -30°C), strain is essentially due to intracrystalline dislocation glide.
82 The transient creep regime is characterized by a strong directional hardening
83 until the strain-rate minimum is reached for an overall strain of 1% (Duval
84 et al., 1983). This strain-rate decrease can reach three orders of magnitude.
85 It is associated to the development of a strong internal stress field due to
86 plastic incompatibility between grains (Ashby and Duval, 1985; Duval et al.,
87 1983; Castelnau et al., 2008b). A significant part of the transient creep is
88 recoverable, i.e., on unloading a creep specimen, a reverse creep is observed,
89 with reverse strain which can be more than ten times the initial elastic strain

90 (Duval, 1976; Duval et al., 1983). In the secondary creep regime, isotropic
 91 polycrystals deform (at similar stress levels) a 100 times slower than a single
 92 crystal optimally oriented for basal slip. In this regime, the minimum strain
 93 rate and the stress are linked by a power law, referred to as Glen’s law in
 94 glaciology (Glen, 1955), expressed through a relationship of the form (1) for
 95 temperatures lower than -10°C .

$$\dot{\epsilon}_{min} = A\bar{\sigma}^n \exp(-E_p/k_B T) \quad (1)$$

96 with $\bar{\sigma}$ the applied stress, $E_p = 0.72$ eV and the stress exponent $n = 3$
 97 (Barnes et al., 1971; Budd and Jacka, 1989). A is a constant, k_B the Boltz-
 98 mann constant and T the temperature. Above -10°C , $\dot{\epsilon}_{min}$ rises more rapidly
 99 with increasing temperature and cannot be described by this equation (Mor-
 100 gan, 1991). No grain-size effect is expected for power-law secondary creep
 101 at laboratory conditions (see Duval and Le Gac (1980); Jacka (1994) for
 102 instance). But a grain size effect was, however, measured during transient
 103 creep (Duval and Le Gac, 1980).

104 At strains larger than 1 to 2% (tertiary creep regime), dynamic recrystalliza-
 105 tion is predominant, and new grain microstructures and crystal orientations
 106 are generated (Jacka and Maccagnan, 1984; Duval et al., 2000).

107 At stresses lower than 0.1 MPa, relevant to deformation conditions in glaciers,
 108 ice sheets or planetary bodies, there is a clear indication of a creep regime
 109 with a stress exponent lower than two. This indication results from both
 110 the analysis of field data and laboratory tests, although the difficulty of
 111 obtaining reliable data at strain rates lower than 10^{-10}s^{-1} is at the ori-
 112 gin of contradictory results (Mellor and Testa, 1969; Barnes et al., 1971;
 113 Dahl-Jensen and Gundestrup, 1987; Pimienta et al., 1987; Lipenkov et al.,
 114 1997; Goldsby and Kohlstedt, 1997). In particular, Goldsby and Kohlstedt

115 (1997) suggest a grain-size dependence of the ice viscosity associated with
116 this low stress regime, based on laboratory experiments performed on very
117 small grain-size samples. This grain-size effect would be associated with
118 a grain boundary-sliding dominated creep. Its extrapolation to polar ice-
119 core deformation conditions remains controversial (Duval and Montagnat,
120 2002). Diffusional creep, commonly associated with such conditions in many
121 materials yields a viscosity much higher than that deduced from field data
122 (Lliboutry and Duval, 1985). For a review on ice behavior, see (Duval et al.,
123 2010).

124 Ice as a model material exhibits a challenging viscoplastic anisotropy ow-
125 ing to the presence of only two independent easy slip systems for the dis-
126 locations (basal plane). While five independent systems are required to
127 accommodate an arbitrary deformation in a single crystal (Taylor, 1938),
128 Hutchinson (1977) showed that four systems are required for allowing an
129 hexagonal polycrystal such as ice to deform. Being able to represent and to
130 take into account this anisotropy in micro-macro models which aim at link-
131 ing the single crystal scale to the polycrystal scale, is of primary interest to
132 the material science community. This anisotropy needs to be accounted for
133 at the dislocation scale in order to build physically-based model for the acti-
134 vation of (poorly known) secondary slip systems. The impact of dislocation
135 induced internal stress fields, but also the characterization and development
136 of highly heterogeneous strain and stress fields within polycrystals, and their
137 impact on fabric development turn out to be of strong importance (Castel-
138 nau et al., 1996a; de la Chapelle et al., 1998).

139 During gravity-driven flow of glaciers and ice sheets, the macroscopic
140 behavior of ice becomes progressively anisotropic with the development of
141 fabrics (or textures, c-axis preferred orientations). This anisotropy and its

142 development depends on the flow conditions, but strongly influences the re-
143 sponse of ice layers to imposed stress (see Gundestrup and Hansen (1984);
144 Van der Veen and Whillans (1990); Mangeney et al. (1997) for pioneer field
145 work and modeling on the subject). Indeed, a polycrystal of ice with most
146 of its c-axes oriented in the same direction deforms at least ten times faster
147 than an isotropic polycrystal, when sheared parallel to the basal planes.
148 Fabrics basically develop as the result of lattice rotation by intracrystalline
149 slip (Azuma and Higashi, 1985; Alley, 1988, 1992). Dynamic recrystalliza-
150 tion can have a major impact on fabric development, especially at temper-
151 atures above -10°C close to bedrocks or within temperate glaciers (Alley,
152 1992; Duval and Castelnau, 1995; de la Chapelle et al., 1998; Montagnat
153 et al., 2009), see Section 5. Questions, however, remain to what extent dif-
154 ferent recrystallization processes operate as a function of depth in polar ice
155 sheets (Kipfstuhl et al., 2006, 2009; Weikusat et al., 2009).

156 *1.2. Main objectives*

157 Accurate modeling of ice flow under natural conditions is relevant for
158 many scientific objectives, such as the response of ice sheet to climate
159 changes (Seddik et al., 2012), the interpretation of climate signals extracted
160 from ice cores (Faria et al., 2010), the energy balance in extraterrestrial
161 satellites (Sotin et al., 2009), and since a few years, the accurate prediction
162 of sea-level rise that is linked to the behavior of fast-moving coastal glaciers
163 (Gillet and Durand, 2010). In this context, challenges are mainly (i) to
164 establish an ice flow law adapted to low stress conditions, changes in tem-
165 peratures and impurity content, (ii) to consider the macroscopic anisotropy
166 due to fabric development at the given conditions, (iii) to be able to inte-
167 grate processes such as dynamic recrystallization that can strongly influence

168 fabric development and the flow law.

169

170 The aim of this paper is to present a general overview of the main mod-
171 eling techniques adapted to ice, and the main modeling results obtained
172 from the single crystal scale to the large scale that is relevant to ice sheet
173 flow modeling. Techniques are highly diverse, from dislocation dynamics
174 (micron scale) to Finite Element methods that are adapted to the whole ice
175 sheet (km scale), via mean-field and full-field micro-macro approaches and
176 coupling with a microstructure evolution models (cm to m scale, limited to
177 a 2D configuration, see 5.2). We will mostly focus on recent advances and
178 topics that are still under development.

179

180 **2. Modeling ice single crystal behavior**

181 Owing to its high viscoplastic anisotropy, with dislocations gliding mostly
182 on the basal plane, studying and modeling ice single crystal behavior is a
183 challenge for regular approaches.

184 Recent efforts focused on three main objectives; (i) understanding, repre-
185 senting and taking into account the dislocation dynamics, (ii) improving our
186 knowledge about secondary slip systems in ice, (iii) providing an accurate
187 crystal plasticity constitutive law that can be implemented in mean-field and
188 full-field approaches for micro-macro polycrystal models. For the two first
189 objectives, Dislocation Dynamic models (DD) were used at the scale of the
190 interaction between dislocation populations (Section 2.1). At a larger scale,
191 the Field Dislocation Mechanic modeling approach (FDM) was applied to
192 ice to evaluate the role of internal stresses associated with dislocation fields

193 and arrangements (Section 2.2). Section 2.3 presents a crystal-plasticity
194 model adapted to the transient creep behavior of ice single crystals.

195 *2.1. Dislocation Dynamics modeling*

196 Dislocation dynamics in ice was shown to be scale free and intermit-
197 tent, thanks to dislocation avalanche measurements via acoustic emissions
198 (Weiss and Grasso, 1997; Weiss et al., 2001; Weiss and Marsan, 2003; Weiss
199 and Montagnat, 2007). Ice was used as a model material for the following
200 reasons: (i) transparency allows direct verification that acoustic emission
201 activity is not related to microcracking, (ii) with the range of stress and
202 temperature considered, diffusion creep is not a significant mechanism, and
203 deformation occurs by dislocation glide only. DD modeling tools were used
204 to better understand and characterize this scale free and intermittent be-
205 havior (for example Miguel et al. (2001); Weiss and Miguel (2004)).

206 Miguel et al. (2001) made use of a discrete dislocation dynamics model with
207 a two-dimensional cross-section of the crystal. This 2D space is randomly
208 filled with edge dislocations gliding along a single slip direction parallel to
209 their respective Burgers vector. This simplification is an effective way to
210 describe materials like ice crystals owing to their strong plastic anisotropy
211 with a single slip system dominating. A basic feature common to most DD
212 models is that dislocations interact with each other through the long-range
213 elastic stress field they produce in the host material. In (Miguel et al.,
214 2001), dislocation velocity depends linearly on this effective stress, and the
215 Peierls stress is set to zero. Mechanisms for dislocation annihilation and
216 multiplication are classically taken into account.

217 Within this simplified scheme the authors found that dislocations gener-
218 ate a slowly evolving configuration landscape which coexists with rapid col-

219 lective rearrangements. These arrangements involve a comparatively small
220 fraction of dislocations and lead to an intermittent behavior of the net plastic
221 response. The model was therefore able to reproduce the fact that disloca-
222 tions themselves, through the various structures such as dipoles and walls,
223 generate a pinning force landscape that is virtually frozen into a slow state.
224 Creation and annihilation mechanisms allow the system to jump between
225 slow dynamics states through bursts of activity.

226 More recently, Chevy et al. (2007, 2012) used DD simulations to analyze
227 torsion tests performed on ice single crystals. The tests were performed
228 with the ice-crystal *c*-axis oriented parallel to the torsion axis so that basal
229 screw dislocations were mainly activated. With synchrotron topography
230 analyses of the deformed samples, it was possible to show that dislocation
231 arrangements were highly heterogeneous, with a scale-invariant character
232 and long-range correlations (Montagnat et al., 2006; Weiss and Montagnat,
233 2007; Chevy et al., 2010). Although these tests were performed in a way that
234 highly favored basal glide, the double-cross slip mechanisms was invoked to
235 explain this scale invariant dislocation arrangement.

236 Three-dimensional DD simulations, based on the TRIDIS code (Verdier
237 et al., 1998), were adapted to these torsion tests on ice and the hexago-
238 nal structure. Screw dislocation sources were positioned within one slip
239 plane at the periphery of a cylinder submitted to a constant torque. Cross-
240 slip on prismatic planes was made possible thanks to the internal stress
241 induced by the pile-up of basal dislocations in the center of the cylinder
242 (where $\sigma_{app} = 0$), which produces the out-of-plane component needed (see
243 Fig. 1). Simulation results allowed to test this hypothesis, and explain the
244 power law relationship between stress and strain rate (Chevy et al., 2012).

245 *2.2. Field Dislocation Mechanics (FDM)*

246 Field dislocation theory is a mesoscale approach, which aims at tak-
247 ing into account the inhomogeneous distribution of dislocations in plasticity
248 modeling. Therefore, FDM modeling makes it possible to represent and con-
249 sider the internal stress field created by the dislocation arrangements within
250 the crystal. FDM is a continuous approach able to deal simultaneously with
251 long-range correlations associated with distortion fields, internal stresses due
252 to dislocation arrangements, and short-range correlations (Acharya, 2001).
253 The reader is referred to (Acharya and Roy, 2006; Varadhan et al., 2006;
254 Fressengeas, 2010) for details.

255 The first application to ice samples was performed in the configuration of
256 the torsion test presented in part 2.1 (Taupin et al., 2007). This test is
257 by itself highly heterogeneous, and this heterogeneity was shown to induce
258 unexpected non-basal slip. Taking into account the coupled dynamics of
259 geometrically necessary screw dislocations gliding in the basal plane (also
260 called "excess" dislocations) and statistical dislocations developed through
261 cross slip in prismatic planes, the model was able to reproduce the creep
262 curves during torsion, and the size effect measured experimentally (see Fig.
263 2). More recently, the model was used to reproduce the complex scale-
264 invariant character of dislocation arrangements forming during torsion tests
265 on ice single crystals (Chevy et al., 2010). In particular, the fact that the
266 model takes into account both the long-range elastic interactions due to
267 the presence of dislocations and the short-range interactions inherent to the
268 transport of dislocations (obstacles, cross-slip, etc.) allowed to reproduce
269 the shift in control of the dislocation distribution by long-range correlations
270 at low strain to a control by short-range correlations at strain as high as
271 50%. It was shown that non-basal dislocations activated by the internal

272 stress fields induce a screening potential at large strain, through obstacles
 273 such as twist sub-boundaries. However, this screening was shown to be too
 274 small to hinder creep acceleration prevailing during torsion creep test on ice
 275 single crystals (Chevy et al., 2010).

276 2.3. Crystal plasticity modeling

277 Constitutive relations to describe the transient creep of ice single crystals
 278 have been proposed by Castelnau et al. (2008b) and then used in a modified
 279 version in Suquet et al. (2011). One of the difficulty here is the description
 280 of the softening of basal slip in the transient regime, as discussed above.
 281 As is usual in crystal plasticity at infinitesimal strains, the strain tensor is
 282 decomposed into the sum of an elastic $\boldsymbol{\varepsilon}^e$ and a viscoplastic $\boldsymbol{\varepsilon}^{vp}$ part

$$\boldsymbol{\varepsilon} = \boldsymbol{\varepsilon}^e + \boldsymbol{\varepsilon}^{vp} . \quad (2)$$

283 The elastic strain is related to the local stress tensor $\boldsymbol{\sigma}$ with the local com-
 284 pliance tensor \mathbf{S} , and the viscoplastic strain results from slips on a total of
 285 M different slip systems:

$$\boldsymbol{\varepsilon}^e = \mathbf{S} : \boldsymbol{\sigma} , \quad \boldsymbol{\varepsilon}^{vp} = \sum_{k=1}^M \gamma^{(k)} \boldsymbol{\mu}^{(k)} . \quad (3)$$

286 Here, $\boldsymbol{\mu}^{(k)} = \frac{1}{2}(\mathbf{n}^{(k)} \otimes \mathbf{b}^{(k)} + \mathbf{b}^{(k)} \otimes \mathbf{n}^{(k)})$ is the (purely geometric) Schmid
 287 tensor depending on the orientation of the slip system (k), \mathbf{n} being the slip
 288 plane normal and \mathbf{b} the slip direction (parallel to the Burgers vector and
 289 orthogonal to \mathbf{n}) in that plane, with \otimes the dyadic product.

290 Ice crystals, which have an hexagonal symmetry, deform easily by shear
 291 on the basal plane, on the three systems $\{0001\} \langle 11\bar{2}0 \rangle$ which provide only
 292 two independent systems. The three prismatic systems $\{1\bar{1}00\} \langle 11\bar{2}0 \rangle$
 293 provide two more independent systems. An additional independent slip

294 system is thus required to attain any isochoric deformation at the single
 295 crystal level and this is achieved by adding the six $\langle c + a \rangle$ pyramidal
 296 systems $\{11\bar{2}2\} \langle 11\bar{2}\bar{3} \rangle$. In total, $M = 12$ slip systems are taken into
 297 account in the present analysis.

298 In the constitutive relations originally proposed by Castelnau et al.
 299 (2008b), the slip rate on the k -th system is related to the resolved shear
 300 stress $\tau^{(k)}$ on that system through:

$$\dot{\gamma}^{(k)} = \dot{\gamma}_0^{(k)} \left(\frac{|\tau^{(k)}|}{\tau_0^{(k)}} \right)^{n^{(k)}} \text{sgn}(\tau^{(k)}), \quad \tau^{(k)} = \boldsymbol{\sigma} : \boldsymbol{\mu}^{(k)}, \quad (4)$$

301 where $\tau_0^{(k)}$, the reference resolved shear stress on system k , depends on the
 302 activity of the other systems through:

$$\dot{\tau}_0^{(k)} = \sum_{\ell=1}^M H^{(k,\ell)} \left(\frac{\tau_{sta}^{(\ell)} - \tau_0^{(\ell)}}{\tau_{sta}^{(\ell)} - \tau_{ini}^{(\ell)}} \right) |\dot{\gamma}^{(\ell)}|. \quad (5)$$

303 The two material parameters $\tau_{ini}^{(\ell)}$ and $\tau_{sta}^{(\ell)}$ refer, respectively, to the initial
 304 value of $\tau_0^{(\ell)}$ at the onset of plasticity (when the $\gamma^{(k)}$'s are small) and to the
 305 stationary value of $\tau_0^{(\ell)}$ at saturation when the plasticity is fully developed
 306 (*i.e.* when the $\gamma^{(k)}$'s are large). Therefore the contribution of system ℓ in
 307 the hardening (or softening) of system k vanishes when $\tau_0^{(\ell)}$ is close to $\tau_{sta}^{(\ell)}$.
 308 The hardening matrix $H^{(k,\ell)}$ expresses the influence of the plastic activity
 309 of system ℓ on the hardening of system k and is taken to be symmetric.
 310 Material data for this model are given in Castelnau et al. (2008b).

311 In (Suquet et al., 2011), Eqs (4) and (5) are improved in two ways:

312 1. Kinematic hardening is introduced in (4) through a back stress $X^{(k)}$:

$$\dot{\gamma}^{(k)} = \dot{\gamma}_0^{(k)} \left(\frac{|\tau^{(k)} - X^{(k)}|}{\tau_0^{(k)}} \right)^{n^{(k)}} \text{sgn}(\tau^{(k)} - X^{(k)}), \quad (6)$$

313 where the back stress evolves with the plastic activity according to an
 314 Armstrong-Frederick type law (Chaboche, 2008):

$$\dot{X}^{(k)} = c^{(k)}\dot{\gamma}^{(k)} - d^{(k)}X^{(k)} \left| \dot{\gamma}^{(k)} \right| - e^{(k)}X^{(k)}, \quad (7)$$

315 including static recovery through coefficient $e^{(k)}$. The introduction
 316 of a back stress on each slip system is motivated by the experimen-
 317 tal observation of recovery strain developing in single crystals when
 318 specimens are subjected to recovery tests (see Section 2.3.2 and Fig.
 319 4).

320 2. The equation governing the reference resolved shear stress $\tau_0^{(k)}$ is mod-
 321 ified into

$$\dot{\tau}_0^{(k)} = \left(\tau_{sta}^{(k)} - \tau_0^{(k)} \right) \dot{p}^{(k)}, \quad \dot{p}^{(k)} = \sum_{\ell=1}^M H^{(k,\ell)} \left| \dot{\gamma}^{(\ell)} \right|. \quad (8)$$

322 The motivation for the change in the evolution rule for the reference
 323 resolved shear stresses $\tau_0^{(k)}$ is that with the original rule (5) they never
 324 reach their stationary value, unless all systems do so at the same time,
 325 a condition which cannot be met in a polycrystal (see details in (Su-
 326 quet et al., 2011)). By contrast, the law (8) ensures convergence of
 327 $\tau_0^{(k)}$ towards its stationary value, provided all coefficients $H^{(k,\ell)}$ are
 328 positive. Indeed, in this case, $\dot{p}^{(k)}$ is always positive and $p^{(k)}$ is in-
 329 creasing with time, acting on system k in a similar way as the classical
 330 cumulated plastic strain of von Mises plasticity. The differential Eq.
 331 (8) can be integrated into

$$\tau_0^{(k)}(p^{(k)}) = \tau_{sta}^{(k)} + (\tau_{ini}^{(k)} - \tau_{sta}^{(k)}) \exp(-p^{(k)}), \quad (9)$$

332 which shows that $\tau_0^{(k)} - \tau_{sta}^{(k)}$ has the same sign as $\tau_{ini}^{(k)} - \tau_{sta}^{(k)}$. Further-
 333 more $\tau_0^{(k)}$ tends to $\tau_{sta}^{(k)}$ when $p^{(k)}$ becomes large.

334 *2.3.1. Data for elasticity*

335 As mentioned in Section 1, ice crystals exhibit a low elastic anisotropy,
 336 the largest stiffness ($E \sim 11.8\text{GPa}$) being along the c -axis (Fig. 3). The
 337 tensor of elastic moduli (in Kelvin’s notations) at -16°C is given by (10)
 338 (Gammon et al., 1983),

$$\begin{pmatrix} \sigma_{11} \\ \sigma_{22} \\ \sigma_{33} \\ \sqrt{2}\sigma_{23} \\ \sqrt{2}\sigma_{13} \\ \sqrt{2}\sigma_{12} \end{pmatrix} = \begin{pmatrix} 13930. & 7082. & 5765. & 0. & 0. & 0. \\ 7082. & 13930. & 5765. & 0. & 0. & 0. \\ 5765. & 5765. & 15010. & 0. & 0. & 0. \\ 0. & 0. & 0. & 6028. & 0. & 0. \\ 0. & 0. & 0. & 0. & 6028. & 0. \\ 0. & 0. & 0. & 0. & 0. & 6848. \end{pmatrix} \begin{pmatrix} \varepsilon_{11}^e \\ \varepsilon_{22}^e \\ \varepsilon_{33}^e \\ \sqrt{2}\varepsilon_{23}^e \\ \sqrt{2}\varepsilon_{13}^e \\ \sqrt{2}\varepsilon_{12}^e \end{pmatrix}, \quad (10)$$

339 where all entries are in MPa and 3 is the axis of transverse isotropy (c -axis of
 340 the hexagonal crystalline structure). For conditions prevailing in ice sheets
 341 and glaciers, elastic constants vary little with temperature: a temperature
 342 change of 5°C only modifies the elastic constants by about 1.5%.

343 *2.3.2. Data for basal slip*

344 The literature provides a number of experimental data for the behavior
 345 of ice crystals deformed in such a way that only basal slip is activated. Due
 346 to the very large viscoplastic anisotropy of ice single crystals, it is stressed
 347 that mechanical tests have to be carried out very carefully to avoid any
 348 heterogeneity of the stress field within the specimen (Boehler et al., 1987).

349 Mechanical tests on single crystals where solely non-basal systems are
 350 activated have not been reported so far. This would require straining the
 351 crystal along or perpendicular to the c -axis, but unfortunately any unavoi-
 352 dable deviation from perfect alignment activates basal slip. Duval et al. (1983)
 353 has given upper bounds for the flow stress on non-basal systems.

354 Consequently, only the material parameters of Eq. (6) relevant for basal
355 slip can be identified with confidence from experimental data on single crys-
356 tals :

- 357 • First, data compiled by Duval et al. (1983) were used to determine the
358 stationary flow stress and the stress-sensitivity exponent $n^{(k)}$ of basal
359 slip. There is quite a large spread in these experimental results from
360 different authors. Despite these uncertainties, the stress-sensitivity
361 exponent for basal slip can be directly identified from these experi-
362 mental data (numerical values are reported in Table 1), whereas the
363 stationary flow stress depends on both the stationary reference stress
364 $\tau_{sta}^{(k)}$ and the stationary backstress $X^{(k)}$.

- 365 • Next, data from Weertman (1973) were used for the identification of
366 the transient creep regime of basal systems. Single crystals were de-
367 formed under uniaxial compression at different strain rates, with c -axis
368 oriented at 45° from the loading direction (Fig. 4). The observed stress
369 peak is associated with the increase in density of mobile dislocations
370 (Duval et al., 1983), a behavior typical for material with very low ini-
371 tial dislocation density (see Sauter and Leclercq (2003); Cochard et al.
372 (2010)). These tests shed light on the softening of basal slip in the
373 transient regime. The static recovery term $e^{(k)}$ in the constitutive law
374 (7) helps achieving the correct stationary stress at very small strain
375 rates (since $X^{(k)}$ tends to a constant value $c^{(k)}/d^{(k)}$ at large shear $\gamma^{(k)}$
376 if static recovery is not introduced).

- 377 • Finally, the recovery test of Taupin et al. (2008) performed on sin-
378 gle crystals under uniaxial compression was considered. Here the c -
379 axis orientation was not precisely defined experimentally, but it made

380 an angle “less than 10° ” with the compression direction. The sin-
381 gle crystal was submitted to four creep loadings for 30 minutes sepa-
382 rated by unloading stages for respectively 1 minute, 10 minutes, and
383 100 minutes (Fig. 4). Upon reloading, the strain rate is larger than
384 just before the last unloading, indicating that dislocations are rear-
385 ranging during the time intervals where the specimen is unloaded.
386 This is accounted for in the model by the back stress $X^{(k)}$, and by
387 $e^{(k)}$.

388 Fig. 4 shows the good match between the model (constitutive Eq. (6)) with
389 the set of parameters given in Table 1 and these experimental results.

390 **3. Mean field approaches for the mechanical response of ice poly-** 391 **crystals**

392 *3.1. Microstructure characterization*

393 From the mechanical point of view, polycrystalline materials have to be
394 considered as a specific class of composites. They are composed of many
395 grains, with grain size in the range of mm to cm for natural ice. Grains are
396 assembled in a random way, *i.e.* their size, shape, and lattice orientation do
397 generally not depend on the size, shape, and orientation of the surrounding
398 grains (Fig. 5). Therefore, the microstructure of ice polycrystals can hardly
399 be described exactly in 3-D, unless one makes use of tomography techniques
400 (Rolland du Roscoat et al., 2011). From (2-D) thin sections, one can at best
401 access a statistical characterization of the 3-D grain arrangement *e.g.* with
402 the help of cross-correlation functions, although the description is generally
403 limited to a few parameters, such as the average grain size and grain shape
404 (aspect ratio). In the Euler orientation space, microstructure description is

405 based on the distribution of crystal lattice orientations (Orientation Distri-
406 bution Function, ODF, or crystallographic texture, often denoted "fabric"
407 in the geophysical community). The complex behavior of polycrystalline
408 materials comes from the anisotropic behavior at the grain scale, closely re-
409 lated to the symmetry of the crystal lattice. This is true for all quantities of
410 interest here, such as elasticity, viscoplasticity and thermal dilation. Grains
411 with different lattice orientations react differently to a given stress level.
412 As far as grain boundaries maintain the cohesion of the material, the *local*
413 stress (*i.e.* inside a grain) differs from the *overall* one (the applied stress),
414 leading to a heterogeneous distribution of stress and strain fields within the
415 polycrystal.

416 Most research efforts in the past years have focussed on the understand-
417 ing of the build-up of these heterogeneities, in relation with the microstruc-
418 ture and local (grain) behavior, since they greatly influence the overall be-
419 havior (for ice, see Grennerat et al. (2012) for instance). For instance, plas-
420 ticity in a polycrystal can start far below the macroscopic yield stress, as it
421 is sufficient that the local stress reaches the local yield stress somewhere in
422 the structure where stress concentration is large enough, such as along grain
423 boundaries (Brenner et al., 2009).

424 There are basically two strategies to get the mechanical response: mean-
425 field (this section) and full-field (next section) approaches. For both of
426 them, the key issue is the estimation of the stress or strain localization
427 (or heterogeneities), in relation to the microstructure and local behavior of
428 grains. Basically, the problem to be solved is to find an equilibrated stress
429 field, related to a compatible strain field with the local constitutive relation,
430 both fields fulfilling the applied boundary conditions. In the following, we
431 review (not in an exhaustive way) some homogenization techniques used for

432 the investigation of the mechanical behavior of ice polycrystals.

433 3.2. Linear thermo-elasticity

434 For reasons that will become evident below, let us consider the case of
 435 thermo-elastic ice polycrystals. The local constitutive relation at point (\mathbf{x})
 436 reads

$$\boldsymbol{\varepsilon}(\mathbf{x}) = \mathbf{S}(\mathbf{x}) : \boldsymbol{\sigma}(\mathbf{x}) + \boldsymbol{\varepsilon}_0(\mathbf{x}), \quad (11)$$

437 with $\boldsymbol{\varepsilon}_0$ a stress-free thermal strain (*e.g.* a dilation), due to temperature
 438 changes. The local stress $\boldsymbol{\sigma}(\mathbf{x})$ can be related to the overall stress (applied
 439 at the polycrystal scale) by means of the stress-concentration tensor $\mathbf{B}(\mathbf{x})$
 440 for the purely elastic problem

$$\boldsymbol{\sigma}(\mathbf{x}) = \mathbf{B}(\mathbf{x}) : \bar{\boldsymbol{\sigma}} + \boldsymbol{\sigma}_{\text{res}}(\mathbf{x}), \quad (12)$$

441 with $\boldsymbol{\sigma}_{\text{res}}$ the residual stress, *i.e.* the stress field remaining locally when
 442 the overall load is suppressed ($\bar{\boldsymbol{\sigma}} = \mathbf{0}$). It can be shown that the overall
 443 polycrystal behavior takes a similar form as Eq. (11)

$$\bar{\boldsymbol{\varepsilon}} = \tilde{\mathbf{S}} : \bar{\boldsymbol{\sigma}} + \tilde{\boldsymbol{\varepsilon}}_0, \quad (13)$$

444 with symbols $\tilde{\cdot}$ and $\bar{\cdot}$ denoting the homogenized (or effective) property and
 445 the volume average over the whole polycrystal volume (also denoted $\langle \cdot \rangle$),
 446 respectively. Therefore, one has $\bar{\boldsymbol{\sigma}} = \langle \boldsymbol{\sigma}(\mathbf{x}) \rangle$ and $\bar{\boldsymbol{\varepsilon}} = \langle \boldsymbol{\varepsilon}(\mathbf{x}) \rangle$, and it can be
 447 shown that the effective compliance $\tilde{\mathbf{S}}$ and the effective thermal strain $\tilde{\boldsymbol{\varepsilon}}_0$
 448 are given by (Laws, 1973)

$$\tilde{\mathbf{S}} = \langle \mathbf{S}(\mathbf{x}) : \mathbf{B}(\mathbf{x}) \rangle, \quad \tilde{\boldsymbol{\varepsilon}}_0 = \langle \boldsymbol{\varepsilon}_0(\mathbf{x}) : \mathbf{B}(\mathbf{x}) \rangle. \quad (14)$$

449 Since, for thermo-elastic polycrystals, the elastic compliance and the
 450 thermal dilation coefficients are uniform properties inside grains, the quan-
 451 tities $\mathbf{S}(\mathbf{x})$ and $\boldsymbol{\varepsilon}_0(\mathbf{x})$ in Eq. (11) can be replaced by the corresponding

452 homogeneous values $\mathbf{S}^{(r)}$ and $\boldsymbol{\varepsilon}_0^{(r)}$ of the considered phase (r). A similar
 453 substitution can be made in Eq. (14), leading to

$$\tilde{\mathbf{S}} = \sum_r c^{(r)} \mathbf{S}^{(r)} : \bar{\mathbf{B}}^{(r)}, \quad \tilde{\boldsymbol{\varepsilon}}_0 = \sum_r c^{(r)} \boldsymbol{\varepsilon}_0^{(r)} : \bar{\mathbf{B}}^{(r)} \quad (15)$$

454 with $\bar{\cdot}^{(r)}$ indicating the average over the volume of phase (r), *e.g.* $\bar{\mathbf{B}}^{(r)} =$
 455 $\langle \mathbf{B}(\mathbf{x}) \rangle^{(r)}$, and $c^{(r)}$ the volume fraction of phase (r). Here, a *mechanical*
 456 *phase* (r) denotes the set of all grains of the polycrystal having the same
 457 crystal orientation; those grains have different shape and environment but
 458 their elastic and thermal properties are identical. From (15), it can be
 459 observed that the sole knowledge of the mean (phase average) values $\bar{\mathbf{B}}^{(r)}$ is
 460 sufficient to estimate the overall polycrystal behavior. It can be anticipated
 461 that, if the quantities $\bar{\mathbf{B}}^{(r)}$ can be calculated without having to know the
 462 complete field of $\mathbf{B}(\mathbf{x})$, computation will be way faster. Hence the name of
 463 "mean-field" approaches presented here.

464 With the effective behavior (Eq. 14) in hand, statistical averages over
 465 crystal orientations (r) can be estimated. Basically, two quantities can be
 466 obtained from mean-field approaches:

- 467 1. The phase average stress (or first moment) $\bar{\boldsymbol{\sigma}}^{(r)} = \langle \boldsymbol{\sigma}(\mathbf{x}) \rangle^{(r)}$

$$\bar{\boldsymbol{\sigma}}^{(r)} = \bar{\mathbf{B}}^{(r)} : \bar{\boldsymbol{\sigma}} + \bar{\boldsymbol{\sigma}}_{\text{res}}^{(r)}, \quad (16)$$

468 with $\bar{\boldsymbol{\sigma}}_{\text{res}}^{(r)}$ the average residual stress of phase (r). The knowledge
 469 of $\bar{\boldsymbol{\sigma}}^{(r)}$ for all phases (r) allows investigating the so-called *interphase*
 470 heterogeneities, *i.e.* the variation of the phase average stress with
 471 respect to the crystal orientation.

- 472 2. Deeper insight into the stress distribution can be obtained from the
 473 second moment $\langle \boldsymbol{\sigma} \otimes \boldsymbol{\sigma} \rangle^{(r)}$ of the stress. This second moment can be

474 obtained by a derivation of the effective energy with respect to lo-
475 cal compliances, see (Bobeth and Diener, 1987; Kreher, 1990; Ponte-
476 Castañeda and Suquet, 1998; Brenner et al., 2004).

477 The standard deviation of the stress distribution within a given crystal ori-
478 entation (r) can be estimated from these two moments as the square root
479 of $\langle \boldsymbol{\sigma} \otimes \boldsymbol{\sigma} \rangle^{(r)} - \langle \boldsymbol{\sigma} \rangle^{(r)} \otimes \langle \boldsymbol{\sigma} \rangle^{(r)}$ (*i.e.* the mean of the square of
480 the stress minus the square of the mean); it is related to the width of the
481 stress distribution in crystal orientation (r), and accounts for both the het-
482 erogeneity of stress distribution *inside* grains but also for the heterogeneity
483 *between* grains of identical orientation but exhibiting different shapes and
484 having different neighborhood. Similar relations can be derived for the strain
485 statistics.

486 3.3. Reuss and Voigt approximations

487 First, two very basic models can be derived, namely *Reuss* (also called
488 *static* in the viscoplastic context) and *Voigt* (or *Taylor*) models. The Reuss
489 model is constructed by considering a uniform stress throughout the poly-
490 crystal, *i.e.* $\boldsymbol{\sigma}(\mathbf{x}) = \bar{\boldsymbol{\sigma}} \quad \forall \mathbf{x}$, or equivalently $\mathbf{B}(\mathbf{x}) = \mathbf{I}$ (with \mathbf{I} the identity ten-
491 sor), and leads to vanishing intra- and inter-granular stress heterogeneities,
492 and uniform strain within grains. The Voigt model considers uniform strain,
493 *i.e.* $\boldsymbol{\varepsilon}(\mathbf{x}) = \bar{\boldsymbol{\varepsilon}} \quad \forall \mathbf{x}$, *i.e.* no intra- and inter-granular strain heterogeneities,
494 and uniform stress within grains. These models violate strain compatibility
495 and stress equilibrium, respectively, and are of limited accuracy when the
496 local behavior is highly nonlinear and/or highly anisotropic, as will be il-
497 lustrated in the next section. Besides simplicity, the main interest of Reuss
498 and Voigt models is based on their bounding character, since they provide,
499 respectively, a lower and an upper bound for the effective stress potential.

500 *3.4. The Self-Consistent (SC) scheme*

501 Unlike full-field approaches detailed in the Section 4, mean-field methods
502 are based on a statistical description of the microstructure, *e.g.* based on
503 few n -points correlation functions, so that the exact position and shape of
504 a specific grain with respect to its neighbors is not known. However, as al-
505 ready introduced, all grains exhibiting the same crystallographic orientation
506 are treated as a single mechanical phase. Owing to the random character
507 of the microstructure with all grains playing geometrically similar roles, the
508 Self-Consistent (SC) scheme (Hershey, 1954; Kröner, 1958; Willis, 1981) is
509 especially well suited for polycrystals. This model, which provides a rela-
510 tively simple expression for $\bar{\mathbf{B}}^{(r)}$, relies on specific microstructures exhibiting
511 perfect disorder and infinite size graduation (Kröner, 1978). The SC scheme
512 has often been described as if the interaction between each grain and its sur-
513 rounding could be approximated by the interaction between one ellipsoidal
514 grain with the same lattice orientation as the original grain and a homoge-
515 neous equivalent medium whose behavior represents that of the polycrystal,
516 taking thus advantage of the analytical solution of Eshelby (1957) for the in-
517 clusion/matrix interaction. This reasoning led to the conclusion that the SC
518 scheme implicitly considers uniform stress and strain rate inside grains. This
519 interpretation turns out to be incorrect, since intraphase stress and strain
520 heterogeneities do not vanish as explained above, see Ponte-Castañeda and
521 Suquet (1998) for a review.

522 The ability of the SC scheme to estimate polycrystal behavior is shown
523 in Fig. 6. Numerical reference solutions from the full-field FFT method
524 (see Section 4) have been generated for many randomly generated Voronoi
525 microstructures, and ensemble average over these random microstructures
526 has been calculated in order to attain results that are representative for

527 a Representative Volume Element, *i.e.* a volume sufficiently large to be
 528 statistically representative of the material (Kanit et al., 2003; Lebensohn
 529 et al., 2004b). In Fig. 6, we provide results for the effective behavior, that
 530 is entirely defined by the effective reference stress $\tilde{\sigma}_0$ which enters in the
 531 effective constitutive relation

$$\frac{\dot{\tilde{\epsilon}}_{eq}}{\dot{\tilde{\epsilon}}_0} = \frac{\bar{\sigma}'_{eq}}{\bar{\sigma}_0} \quad (17)$$

532 with $\dot{\tilde{\epsilon}}_0$ a reference strain rate (taken here equal to $\dot{\gamma}_0$), and $\bar{\sigma}'_{eq}$ and $\dot{\tilde{\epsilon}}_{eq}$ the ef-
 533 fective equivalent stress and strain rate respectively ($\bar{\sigma}'_{eq} = \sqrt{3\bar{\sigma} : \bar{\sigma}}/2$, $\dot{\tilde{\epsilon}}_{eq} =$
 534 $\sqrt{2\dot{\tilde{\epsilon}} : \dot{\tilde{\epsilon}}/3}$). Calculations are performed for various viscoplastic anisotropy
 535 contrasts (or slip system contrasts) at the grain level, defined by the ratio
 536 between non-basal and basal reference shear stresses, *i.e.* $\tau_0^{(Pr)}/\tau_0^{(Ba)}$ for
 537 $\tau_0^{(Pr)} = \tau_0^{(Pr)}$. It can be observed that the SC model perfectly reproduces
 538 the reference full-field (FFT) results. Note also that the Reuss bound, of-
 539 ten used for highly anisotropic materials like ice, predicts a much too soft
 540 overall behavior. This simple approach does not allow to make a realis-
 541 tic link between local and overall rheologies. We also report in this figure
 542 the standard deviations (or overall heterogeneities) of equivalent stress and
 543 strain rate. These standard deviations have been calculated over the whole
 544 polycrystal. Recall that they account for both intra- and inter-granular field
 545 heterogeneities for both SC and FFT approaches. It can be observed that
 546 the increase of standard deviation with the slip system contrast is well re-
 547 produced by the SC scheme, although some discrepancies with FFT results
 548 arise at very large contrasts (mostly for the strain-rate fluctuation). Note
 549 again that Reuss and Voigt bound do not reproduce these results, even in
 550 a qualitative way, since they predict, by construction, vanishing fluctuation
 551 of stress and strain rate, respectively. Unlike these simple approaches, the

552 SC scheme not only predicts the correct effective stress, but also accurately
 553 captures the field heterogeneities within the polycrystal. Similar agreement
 554 have been obtained for Voronoi and EBSD 2-D microstructures under an-
 555 tiplane shear by Lebensohn et al. (2005).

556 3.5. Nonlinear viscoplasticity

557 The mean-field estimate of *nonlinear materials* is significantly more com-
 558 plex than the thermo-elastic case treated above. We consider the case of a
 559 viscoplastic polycrystal of ice in which grains are deforming by glide of dis-
 560 locations on specific slip planes, as discussed above, with slip rates given by
 561 Eq. (4), so that the local strain rate reads, since elastic deformations are
 562 neglected:

$$\dot{\boldsymbol{\epsilon}}(\mathbf{x}) = \sum_k \boldsymbol{\mu}_{(k)}^{(r)} \dot{\gamma}_{(k)}(\mathbf{x}) . \quad (18)$$

563 Here, reference stresses τ_0 and stress sensitivities n are supposed to be con-
 564 stant. The constitutive Eq. (18) can also be written

$$\dot{\boldsymbol{\epsilon}}(\mathbf{x}) = \mathbf{M}(\mathbf{x}) : \boldsymbol{\sigma}(\mathbf{x}) \quad (19)$$

565 with

$$\mathbf{M}(\mathbf{x}) = \sum_k \frac{\dot{\gamma}_0^{(k)}}{\tau_0^{(k)}} \left| \frac{\boldsymbol{\mu}^{(k)}(\mathbf{x}) : \boldsymbol{\sigma}(\mathbf{x})}{\tau_0^{(k)}} \right|^{n^{(k)}-1} \boldsymbol{\mu}^{(k)}(\mathbf{x}) \otimes \boldsymbol{\mu}^{(k)}(\mathbf{x}) . \quad (20)$$

566 Obviously, the viscous compliance \mathbf{M} relating $\dot{\boldsymbol{\epsilon}}(\mathbf{x})$ and $\boldsymbol{\sigma}(\mathbf{x})$ – which plays
 567 a similar role as \mathbf{S} in Eq. (11) – is not uniform within a phase, owing to the
 568 stress sensitivities $n \neq 1$ and the heterogeneity of $\boldsymbol{\sigma}$ in the phases. Conse-
 569 quently, (14) cannot be replaced by (15) for nonlinear behavior. The basic
 570 method to deal with such nonlinear behavior is to define a *Linear Compari-*
 571 *son Polycrystal* (LCP) having the same microstructure as the real nonlinear

572 polycrystal, and to which the linear homogenization scheme applies (Ponte-
573 Castañeda and Suquet, 1998). Of course, the effective behavior estimated
574 this way remains nonlinear, since the definition of the LCP depends on the
575 applied macroscopic stress. The difficult part of the problem consists of
576 finding the best *linearization* procedure leading to the optimal selection of
577 the LCP. Since decades, there has been quite a number of propositions in
578 the literature dealing with this issue, leading to a *generalization* of the SC
579 scheme for nonlinear behavior. The local constitutive relation given by Eqs
580 (18-20) has to be linearized in a suitable way to obtain a form similar to
581 (11), with \mathbf{S} and $\dot{\boldsymbol{\varepsilon}}_0$ uniform per phase (and where $\boldsymbol{\varepsilon}$ is replaced everywhere
582 by $\dot{\boldsymbol{\varepsilon}}$). Generally speaking, the linearization can be expressed in the form
583 depicted in Fig. 7, (Liu and Ponte Castañeda, 2004).

$$\dot{\gamma}_{(k)}(\mathbf{x}) = \alpha_{(k)}^{(r)} \tau_{(k)}(\mathbf{x}) + \dot{\varepsilon}_{(k)}^{(r)}, \quad (21)$$

584 thus leading to the following expressions for $\mathbf{S}^{(r)}$ and $\dot{\boldsymbol{\varepsilon}}_0^{(r)}$

$$\mathbf{S}^{(r)} = \sum_k \alpha_{(k)}^{(r)} \boldsymbol{\mu}_{(k)}^{(r)} \otimes \boldsymbol{\mu}_{(k)}^{(r)}, \quad \dot{\boldsymbol{\varepsilon}}_0^{(r)} = \sum_k \dot{\varepsilon}_{(k)}^{(r)} \boldsymbol{\mu}_{(k)}^{(r)}, \quad (22)$$

585 where the shear compliance $\alpha_{(k)}^{(r)}$ and stress-free slip-rate $\dot{\varepsilon}_{(k)}^{(r)}$ can be easily
586 expressed with respect to two reference shear stresses $\check{\tau}_{(k)}^{(r)}$ and $\hat{\tau}_{(k)}^{(r)}$, see Fig.
587 7. The optimal choice (from the point of view of the variational mechanical
588 problem) of those reference stresses is not straightforward; this is the main
589 reason why several extensions of the SC scheme have been proposed in the
590 literature. Obviously, all of them reduce to the same SC model in the linear
591 case $n = 1$.

592 Following Ponte Castañeda (1996), Masson et al. (2000) proposed the
593 so-called “affine” (AFF) linearization scheme which is based on the simple

594 idea of a linear behavior (21) tangent to the nonlinear one (4) at the mean
 595 shear stress, leading to

$$\tilde{\tau}_{(k)}^{(r)} = \hat{\tau}_{(k)}^{(r)} = \langle \tau_{(k)} \rangle^{(r)}, \quad \alpha_{(k)}^{(r)} = \left. \frac{\partial \dot{\gamma}}{\partial \tau} \right|_{\tau = \tilde{\tau}_{(k)}^{(r)}}. \quad (23)$$

596 The main limitations of this procedure are discussed in detail in Masson
 597 et al. (2000) and Bornert and Ponte Castañeda (1998). One of them is the
 598 violation of rigorous upper bounds for the effective behavior. More generally,
 599 the affine extension is known to overestimate the overall viscosity, *i.e.* to
 600 predict an effective behavior that is too stiff. This negative feature can be
 601 alleviated by means of the energy formulation originally proposed by Ponte
 602 Castañeda (1996) (see Bornert et al. (2001)).

603 Alternative, more sophisticated ways to generalize the SC scheme have
 604 been proposed by Ponte Castañeda and co-workers during the last decades.
 605 The basic idea of these methods is to guide the choice of the properties of the
 606 LCP by a suitably designed variational principle. An “optimal” solution has
 607 been obtained in the context of the so-called “variational” procedure (VAR)
 608 (Ponte Castañeda, 1991), which was extended to polycrystals by De Botton
 609 and Ponte Castañeda (1995), leading to the choice

$$\tilde{\tau}_{(k)}^{(r)} = 0, \quad \hat{\tau}_{(k)}^{(r)} = \left[\langle \tau_{(k)}^2 \rangle^{(r)} \right]^{1/2}. \quad (24)$$

610 The main advantage of this procedure is to provide a rigorous bound, sharper
 611 than the Voigt bound, for the effective potential. More recently, the “second-
 612 order” (SO) method of Ponte Castañeda (2002), extended to polycrystals in
 613 (Liu and Ponte Castañeda, 2004) has been proposed. It leads to reference
 614 shear stresses reading

$$\tilde{\tau}_{(k)}^{(r)} = \langle \tau_{(k)} \rangle^{(r)}, \quad \hat{\tau}_{(k)}^{(r)} = \tilde{\tau}_{(k)}^{(r)} \pm \left[\langle (\tau_{(k)} - \tilde{\tau}_{(k)}^{(r)})^2 \rangle^{(r)} \right]^{1/2}. \quad (25)$$

615 The main differences between AFF, VAR, and SO models may be sum-
 616 marized as follows. The AFF estimate can be regarded as a relatively simple
 617 model, allowing rapid computations which can even be rather accurate for
 618 polycrystals with weak grain anisotropy and small stress sensitivity. How-
 619 ever, its predictions can become unrealistic (*e.g.* bound violation) at a strong
 620 anisotropy or nonlinearity. Contrary to AFF, for which linearization only
 621 accounts for the phase average stress, VAR accounts for the second moments
 622 of the stress, whereas the SO procedure accounts for both the phase aver-
 623 age stress *and* intraphase standard deviation (first and second moments)
 624 to build the LCP. They can therefore provide better estimates in cases of
 625 highly heterogeneous stress distributions, such as for strongly nonlinear or
 626 anisotropic polycrystals. Applications of the VAR procedure to polycrystals
 627 with grains having cubic or hexagonal crystallographic structures can be
 628 found in (Nebozhyn et al., 2001; Liu et al., 2003).

629 Finally, the “tangent” (TGT) extension of the SC scheme (Molinari
 630 et al., 1987; Lebensohn and Tomé, 1993), often referred to as the “VPSC
 631 model” in the literature, is based on the same tangent linearization (23) as
 632 the AFF method. However, unlike the AFF extension, this procedure takes
 633 advantage of the fact that, for power-law polycrystals with a single stress
 634 exponent n for all slip systems, the tangent behavior (21) can be replaced
 635 by a secant-like relation, with $\dot{\epsilon}_{(k)}^{(r)} = 0$ and $\alpha_{(k)}^{(r)}$ replaced by $\alpha_{(k)}^{(r)}/n$. The
 636 same procedure is further applied at the macroscopic level, leading to an
 637 inconsistent definition for the stress localization tensor $\mathbf{B}^{(r)}$ that combines a
 638 secant description for the local and global behaviors but a tangent analysis
 639 for the inclusion/matrix interaction (Masson et al., 2000). When expressed
 640 in the form of tangent expressions, it can be shown that $\dot{\epsilon}_0$ differs from the
 641 exact relation given in (15).

642 3.5.1. Application to natural ices: effective behavior

643 Application of homogenization techniques to natural ices aims at un-
644 derstanding (and predicting) the anisotropic behavior of strongly textured
645 specimens, as encountered at depth in natural ice sheets. As will be seen in
646 section 6, the viscoplastic anisotropy of polycrystals significantly influences
647 ice flow at large scales (Mangeny et al., 1996; Gillet-Chaulet et al., 2006;
648 Pettit et al., 2007; Martín et al., 2009). Castelnau et al. (1998) reported
649 mechanical tests performed on specimens from the GRIP ice core (Central
650 Greenland). Along the ice core, the ice microstructure, and in particular
651 the crystallographic fabric, is evolving; with increasing depth, randomly ori-
652 ented c -axis at the surface of the ice sheet tend to concentrate towards the
653 *in situ* vertical direction down to a depth of ~ 2600 m. Beneath this depth,
654 less pronounced textures are observed due to the initiation of migration re-
655 crystallization (Thorsteinsson et al., 1997). In (Castelnau et al., 1998), the
656 experimental stationary creep behavior of those ices have been obtained for
657 two loading conditions (Fig. 8). The first one corresponds to an *in situ* ver-
658 tical compression, showing an increasing flow stress (decreasing strain rate
659 for a constant applied stress) with increasing depth, since the activation of
660 non-basal slip systems is necessary for pronounced fabrics. The second load-
661 ing condition corresponds to *in situ* horizontal shear, promoting basal slip
662 and resulting in a softening of the ice with increasing fabric strength. It can
663 be seen that for a given applied stress, strain rates can vary by more than
664 two orders of magnitude depending on the orientation of the applied stress
665 with respect to the specimen fabric, reflecting the very strong viscoplastic
666 anisotropic of ice specimens.

667 The effective behavior predicted by the affine (AFF) SC model is com-

668 pared to the experimental data in Fig. 8. It can be observed that the agree-
 669 ment is excellent, meaning that the relation between fabric and effective rhe-
 670 ology is very well captured by the model. The model captures correctly the
 671 increasing anisotropy from the surface down to ~ 2600 m depth, and the de-
 672 crease below. The difference by more than two orders of magnitude between
 673 the vertical and shear strain-rates at ~ 2600 m is also well reproduced, al-
 674 though this was a challenging feature for the model. To get these results, the
 675 reference shear stress $\tau_0^{(k)}$ entering the local constitutive relation, and also
 676 the stress sensitivity $n^{(k)}$, for each slip system (k), had to be identified from
 677 comparison with a database that included single-crystal experimental tests,
 678 and polycrystal ones on many different crystallographic textures (Castelnau
 679 et al., 2008b). The resulting single-crystal rheology, used as input in the SC
 680 model to get the effective behavior described above, is shown in Fig. 9. For
 681 basal slip, agreement with experimental data from the literature is almost
 682 perfect. Non-basal systems are much stiffer than the basal systems, and
 683 pyramidal slip is found to be much more difficult than prismatic slip. These
 684 results are in good agreement with the available data on single crystals, and
 685 in qualitative agreement with the known dislocation structure in ice. There-
 686 fore, it can be anticipated that the affine SC model does a good job in making
 687 the link between the grain and the polycrystal scales, and provides an ac-
 688 curate estimate of the mechanical interaction between deforming grains. In
 689 other words, one can anticipate that results shown in Fig. 8 are based on a
 690 realistic description of the mechanical interaction between grains and phys-
 691 ical deformation processes (dislocation glide) at the (sub)grain level. It can
 692 also be seen on Fig. 9 that this identification procedure leads to different
 693 stress sensitivities for the different slip system families. A value $n^{(k)} = 2$ was
 694 imposed for basal slip in accordance with experimental data, but values for

695 prismatic and pyramidal systems were considered as adjustable parameters.
696 It is also worth noting that the affine model perfectly reproduces an effective
697 stress sensitivity (i.e. at the polycrystal scale) $\tilde{n} = 3$ in agreement with ex-
698 perimental data, although the two major slip systems, basal and prismatic
699 slip, have stress sensitivities smaller than 3 ($n^{(bas)} = 2.0$, $n^{(pr)} = 2.85$). A
700 larger value was considered only for pyramidal slip ($n^{(py)} = 4.0$), but it is
701 worth mentioning that the contribution of pyramidal slip is only very mi-
702 nor (<2%). It can be concluded that, in ice, although basal slip is by far
703 the most active deformation mechanism, secondary slip systems are of great
704 importance for explaining the polycrystal behavior. Basal slip alone does
705 not allow for plastic deformation of ice polycrystals, since it only provides
706 two independent slip systems. Secondary slip systems, here prismatic and
707 pyramidal slip, *must* therefore be activated to add two more independent
708 slip systems. The strength of these stiffer mechanisms determines the vis-
709 coplastic anisotropy at the grain scale, and therefore they also control the
710 level of inter- and intra-granular heterogeneities of stress and strain(-rate),
711 and therefore the effective polycrystal rheology. Similar conclusions have
712 been drawn for olivine, a mineral with only three independent slip systems
713 (Castelnau et al., 2008a, 2009, 2010a,b). We therefore anticipate that the
714 strong effect of secondary deformation mechanisms observed here might be
715 a general feature for all polycrystalline materials with less than four inde-
716 pendent slip systems. The corollary of these results is that simple or *ad hoc*
717 polycrystal models, such as the Reuss (uniform stress) model, in which ice
718 polycrystals can deform with only basal slip, cannot be accurate. This has
719 been shown for example in (Castelnau et al., 1997): whatever the strength
720 used for prismatic and pyramidal systems, the Reuss model is not able to
721 reproduce the very large anisotropy of GRIP specimens shown in Fig. 8.

722 This comes from the fact that internal stresses, that have a large influence
723 on the material behavior, are ignored.

724 Finally, it is also worth mentioning that the TGT SC approach, used
725 in earlier studies, *e.g.* (Castelnau et al., 1997), does not provide as good a
726 match to experimental data as the AFF SC extension. There can be two
727 reasons for that: (i) first of all, it is now known that the inconsistency in
728 the formulation of the TGT SC version leads to an underestimation of the
729 internal stress level, predicting a too soft polycrystal behavior (Gilormini,
730 1995; Masson et al., 2000); (ii) second, by construction, the TGT model is
731 limited to grain behavior for which all slip systems exhibit the same stress
732 sensitivity $n^{(k)}$. When applied to ice, one must thus consider $n^{(k)} = 3.0$ for
733 all systems, including basal slip, in order to get an effective $\tilde{n} = 3$. The fact
734 that the AFF extension does not have this limitation might also explain a
735 better consistency with experimental data.

736 *3.5.2. Application to natural ices: texture development*

737 Using the Reuss approximation, Van der Veen and Whillans (1994) and
738 Castelnau and Duval (1994) described the fabric evolution under compres-
739 sion, tension, simple and pure shear. Van der Veen and Whillans (1994)
740 needed to impose a kind of "recrystallization" criterion (see Section 5.1) to
741 be able to correctly represent the single-maximum fabric (with c-axis ori-
742 ented along one direction) in ice deforming in pure shear. Nevertheless, the
743 Reuss approximation faces inconsistency to describe the fabric evolution at
744 the polycrystal scale, as it requires additional kinematical constraints to
745 link the grain rotation-rate with the polycrystal rotation-rate. In most of
746 the "Reuss" type models, these two rates are supposed to be equal, although
747 the velocity field is not continuous.

748 Models that modify this homogeneous stress assumption were proposed
749 by Azuma (1994) and Thorsteinsson (2002). They introduce some redistri-
750 bution of stress through neighborhood interaction to define the crystal strain
751 at a given bulk equivalent strain. In particular, Thorsteinsson (2002) defines
752 a crystal arrangement on a three-dimensional cubic grid, where each crystal
753 has six nearest neighbors. The nearest neighbor interaction (NNI) is taken
754 into account by defining a local softness parameter for each crystal which
755 modifies the stress acting on the central crystal compared to the macro-
756 scopic stress. This softness parameter further influences the rotation rate
757 of the crystal lattice compared to the bulk. For uniaxial compression tests,
758 the fabrics obtained with the NNI formulation are less concentrated than
759 the ones where no NNI is considered. The reason for this is that the NNI
760 formulation allows all crystals to deform to some extent, while only "soft"
761 crystals would deform in the no-NNI formulation. The fabric obtained after
762 50% shortening strain compares qualitatively well with the one measured
763 along the GRIP ice core at a depth where the strain is similar (1293 m)
764 (Thorsteinsson et al., 1997).

765 The VPSC model in its "tangent" version was applied to simulate the
766 fabric development along ice cores (Castelnau et al., 1996b,a, 1998). In
767 (Castelnau et al., 1996a), a comparison was made with bound estimates
768 (Reuss and Voigt). Fabrics simulated in uniaxial compression and extension
769 were found to be qualitatively similar for all models. However, large dif-
770 ferences in the rate of fabric development were found. This was explained
771 by the different interaction stiffness between grain and matrix for the three
772 approaches. The fabrics obtained with the VPSC model for uniaxial defor-
773 mation were in close agreement with the one measured along the ice core
774 (see Fig. 10). In particular, this model well reproduced the fabric evolution

775 along the GRIP ice core within the upper 650 m where dynamic recrystal-
776 lization is not supposed to strongly impact this evolution (Castelnau et al.,
777 1996b). Lower down, the modeled fabric concentration is too high. Al-
778 though Castelnau et al. (1996b) attributed this discrepancy to the effects
779 of rotation recrystallization along the core, it was later shown that the tan-
780 gent approximation overestimates the lattice rotation. In simple shear, the
781 single-maximum fabric found along the ice cores or experimentally could
782 not be reproduced with the VPSC scheme. To get close to this fabric, an
783 extensive (and probably unrealistic) activity of non-basal slip systems was
784 required. More recently, the "second order" (SO) mean field method of
785 Ponte Castañeda (2002) was used to simulate the fabric development along
786 the Talos Dome ice core (Montagnat et al., 2012). Although no recrystalliza-
787 tion mechanisms were implemented in this version, the fabric development
788 was astonishingly well reproduced, under the crude assumption of uniaxial
789 compression with a constant strain rate (see Fig. 11). In particular, a good
790 match was obtained when the initial fabric is non isotropic and similar to
791 the one measured in the top firn, at 18 m depth. The cumulated compres-
792 sive strain along the core was derived from the thinning function provided
793 by the TALDICE-1 chronology (Buiron et al., 2011). The good prediction
794 performed by the VP-SO scheme is probably due to the fact that this SO ap-
795 proach provides a better estimate of the effective behavior than the classical
796 tangent "VPSC" model does in the case of strongly anisotropic materials
797 such as ice (see Section 3.5). Nevertheless, the modeled fabric evolution
798 could not capture the strengthening rate associated with the Glacial to In-
799 terglacial climatic transition. At these transition, a change in ice viscosity
800 is expected. It induces an higher sensitivity to the impact of shear stress
801 increasing with depth, that the modeling approach did not considered.

802 It is also recalled that the heterogeneity of shear on slip systems at the
803 grain level gives rise to heterogeneities of lattice rotation, and therefore
804 generates intragranular misorientations that somehow spread crystal orien-
805 tations. It is however worth mentioning that *all* models presented above
806 do not consider this strain heterogeneity for estimating fabric evolutions at
807 finite strain. Even in VAR and SO procedures, intraphase strain hetero-
808 geneities are considered for defining the LCP, but so far not for estimating
809 microstructure evolutions. As a consequence, mean-field approaches gener-
810 ally predict too sharp textures. The same applies to the prediction of strain
811 hardening, associated with dislocation processes such as storage and an-
812 nealing. A quantitative study, based on comparisons with reference results
813 obtained by a FFT full-field approach, can be found in (Castelnau et al.,
814 2006).

815 Most of the efforts to simulate the fabric development in ice, and espe-
816 cially along ice cores, had to face the fact that recrystallization mechanisms
817 could impact this fabric development. This was, most of the time, the anal-
818 ysis made for the observed discrepancies between simulated and measured
819 fabrics (Van der Veen and Whillans, 1994; Wenk et al., 1997; Castelnau
820 et al., 1996b; Thorsteinsson, 2002). Some efforts to implement recrystal-
821 lization mechanisms in mean-field approaches will be described in Section
822 5.1.

823 *3.6. Modeling the elasto-viscoplastic behavior*

824 Transient creep is typically encountered when ice flow changes direction,
825 such as in glaciers flowing above irregular bedrock or submitted to tide forc-
826 ing close to the sea-shore or in icy satellites. During laboratory experiments,
827 transient creep is characterized by a strain-rate drop of more than two or-

828 ders of magnitude before reaching the secondary creep close to 1% strain,
829 following Andrade’s law (Duval, 1978). This decrease is associated with the
830 development of large internal stress fields due to intergranular interactions
831 and a strong kinematic hardening (Duval et al., 1983; Ashby and Duval,
832 1985; Castelnau et al., 2008b). To reproduce this transient behavior, one
833 has to consider the coupling between elasticity and viscoplasticity that gives
834 rise to the so-called ”long-term memory effect”, as explained below.

835 The application of homogenization schemes to the *elasto-viscoplasticity*
836 of polycrystals is more complicated than for viscoplasticity, see for instance
837 (Laws and McLaughlin, 1978). In short, it can be shown that, even in the
838 simple case of a polycrystal comprising grains whose behavior exhibits a sin-
839 gle relaxation time (so-called “short-term memory”), the effective behavior
840 exhibits a continuous spectrum of relaxation time (“long-term memory ef-
841 fect”) (Sanchez-Hubert and Sanchez-Palencia, 1978; Suquet, 1987). In other
842 words, the overall behavior of a polycrystal is not of the Maxwell type (par-
843 allel association of a spring and a dashpot with constant viscosity), even
844 though the individual grains do exhibit local Maxwell type behavior. The
845 basic difference between elasto-viscoplasticity and viscoplasticity is that, for
846 elasto-viscoplasticity, the local strain rate depends on both the stress (vis-
847 cous part) and the stress-rate (elastic part), whereas it only depends on the
848 stress for viscoplasticity. Therefore, the local strain rate not only depends
849 on the actual local stress, but also on the whole stress history from the
850 initial specimen loading at $t = 0$ up to the current time. To obtain the
851 exact effective mechanical response at time t , it is thus required to keep
852 track of all information (or internal variables) corresponding to the strains
853 at all previous times, and therefore the problem is not simple. Within mean-
854 field approaches, some approximations (with hopefully limited effects on the

855 accuracy of the solution) are thus necessary.

856 Basically, two approaches have been proposed to deal with this issue. A
857 promising method based on an incremental variational procedure has been
858 proposed by Lahellec and Suquet (2006, 2007). These authors have shown
859 that the homogenization of a *linear visco-elastic* material (*i.e.* with $n = 1$)
860 can be expressed in terms of a homogenization problem for a linear ther-
861 moelastic composite with non piecewise uniform eigenstrains. One advantage
862 of this formulation is that it can make use of the intraphase heterogeneities
863 of stress and strain (-rate), and it can therefore probably provide accurate
864 results even at high stress sensitivity and/or local anisotropy. An alternative
865 approach, which provides a good compromise between accuracy of the solu-
866 tion and simplicity of the formalism, is the so-called “affine” Self-Consistent
867 method of Masson and Zaoui (1999). It is based on the correspondence
868 principle (Mandel, 1966), which states that the elasto-viscoplastic problem
869 can be reduced to a simpler homogenization problem (in fact similar to a
870 standard thermo-elastic problem) if solved in Laplace space. One difficulty
871 of this approach is the calculation of the inverse Laplace transforms, that
872 has to be carried out numerically. An approximate inversion procedure,
873 adapted for creep, has been proposed by Brenner et al. (2002b). It has pro-
874 vided promising results for the creep behavior of Zirconium alloys (Letouzé
875 et al., 2002; Brenner et al., 2002a), since it retains the long-term memory
876 effect associated with the elasto-viscoplastic coupling. Recent developments
877 (Ricaud and Masson, 2009) have shown that an internal variable formulation
878 arises naturally from this affine method, providing results in perfect match
879 with reference FFT solutions in the case of linear viscoelasticity (Vu et al.,
880 2012).

881 To the best of our knowledge, this affine method is the only mean-field

882 approach that has been applied to simulate the transient creep of ice (Castel-
883 nau et al., 2008b). Applications make use of the crystal plasticity model
884 for single crystals detailed in Section 2.3. It was shown that the strong
885 hardening *amplitude* during the transient creep (*i.e.* the decrease of the
886 overall strain rate by several orders of magnitude) is explained by the stress
887 redistribution within the specimen: when the overall stress is applied in-
888 stantaneously, the instantaneous polycrystal response is purely elastic, and
889 since the elastic anisotropy is small, stress distribution within and between
890 grains is almost uniform. But plastic deformation comes into play rapidly to
891 cause a strong redistribution of stress (with large interphase and intraphase
892 heterogeneities) due to the strong viscoplastic anisotropy at the grain scale.
893 This significantly reduces the overall strain rate. On the other hand, the
894 experimental hardening rate (*i.e.* the time necessary to reach the secondary
895 creep regime) is much too slow to be explained by the same process, and is
896 attributed to the hardening of hard-glide slip systems (prismatic slip) in the
897 transient regime, associated with dislocation processes (Fig. 12).

898 **4. Full field approaches for the polycrystal**

899 Mean-field approaches have been extensively used to predict the mechan-
900 ical behavior of ice polycrystals, and the fabric development as measured
901 along ice cores. Due to its high viscoplastic anisotropy, deformation in ice is
902 expected to be strongly heterogeneous, with a strong impact of grain inter-
903 actions and kinematic hardening (Duval et al., 1983; Hamman et al., 2007;
904 Montagnat et al., 2011; Grennerat et al., 2012). The mean-field approaches
905 described above are based on the statistical characterization of the intragran-
906 ular mechanical fields (in terms of average grain stresses and strain rates,

907 and, in the most advanced formulations, also through the determination of
908 the intracrystalline average field fluctuations), but the actual micromechan-
909 ical fields remain inaccessible to these homogenization approaches. Model-
910 ing the full intracrystalline heterogeneity that develops in ice polycrystals
911 requires the use of full-field approaches. This part will concentrate on full-
912 field approaches that are using the Fast Fourier Transform method to solve
913 the constitutive equations in a discretized polycrystal. It aims at studying
914 the correlation between the heterogeneous deformation patterns that appear
915 inside the constituent single-crystal grains of an ice aggregate and their cor-
916 responding crystallographic orientations, along with the influence of other
917 factors, such as orientation and size of neighboring grains. Both viscoplastic
918 and elasto-viscoplastic behavior were investigated, and are presented in the
919 two following sections.

920 *4.1. Viscoplastic approach - FFT*

921 *4.1.1. Viscoplastic FFT-based formulation*

922 The intracrystalline states that are developed during creep of polycrys-
923 talline ice can be obtained using an extension of an iterative method based on
924 FFT, originally proposed by Moulinec and Suquet (1998) and Michel et al.
925 (2001) for linear and non-linear composites (Lebensohn et al., 2009; Mon-
926 tagnat et al., 2011). This formulation was later adapted to polycrystals and
927 applied to the prediction of texture development of fcc materials (Leben-
928 sohn, 2001), and in turn used for the computation of field statistics and
929 effective properties of power-law 2D polycrystals (Lebensohn et al., 2004a,
930 2005) and 3D cubic, hexagonal (Lebensohn et al., 2004b) and orthorhombic
931 (Castelnau et al., 2008a) materials. The FFT-based formulation was also ap-
932 plied to compute the development of local misorientations in polycrystalline

933 copper, with direct input from orientation images (Lebensohn et al., 2008).
 934 As will be detailed in Section 4.2 it was further extended to transient behav-
 935 ior with an elasto-viscoplastic formulation (Idiart et al., 2006; Suquet et al.,
 936 2011; Lebensohn et al., 2012). The FFT-based full-field formulation for vis-
 937 coplastic polycrystals is conceived for a periodic unit cell, provides an exact
 938 solution of the governing equations, and has better numerical performance
 939 than a FE calculation for the same purpose and resolution. The viscoplas-
 940 tic FFT-based formulation consists in finding a strain-rate field, associated
 941 with a kinematically-admissible velocity field, which minimizes the average
 942 of local work-rate, under the compatibility and equilibrium constraints. The
 943 method is based on the fact that the local mechanical response of a periodic
 944 heterogeneous medium can be calculated as a convolution integral between
 945 the Green function of a linear reference homogeneous medium and the ac-
 946 tual heterogeneity field. Such type of integrals reduce to a simple product
 947 in Fourier space, therefore the FFT algorithm can be used to transform the
 948 heterogeneity field into Fourier space and, in turn, to get the mechanical
 949 fields by antitransforming that product back to real space. However, since
 950 the actual heterogeneity field depends precisely on the a priori unknown me-
 951 chanical fields, an iterative scheme should be implemented to obtain, upon
 952 convergence, a compatible strain-rate field and a stress field in equilibrium.

953 The periodic unit cell representing the polycrystal is discretized by means
 954 of a regular grid $\{x^d\}$, which in turn determines a corresponding grid of the
 955 same dimensions in Fourier space $\{\xi^d\}$. Velocities and tractions along the
 956 boundary of the unit cell are left undetermined under the sole condition of
 957 periodicity. An average velocity gradient $V_{i,j}$ is imposed to the unit cell,
 958 which gives an average strain rate $\dot{\bar{\epsilon}}_{ij} = \frac{1}{2}(V_{i,j} + V_{j,i})$. The local strain-rate
 959 field is a function of the local velocity field, i.e. $\dot{\epsilon}_{ij}(\mathbf{v}_k(\mathbf{x}))$, and can be

960 split into its average and a fluctuation term: $\dot{\epsilon}_{ij}(\mathbf{v}_k(\mathbf{x})) = \dot{\bar{\epsilon}}_{ij} + \tilde{\epsilon}_{ij}(\tilde{\mathbf{v}}_k(\mathbf{x}))$,
 961 where $\mathbf{v}_i(\mathbf{x}) = \dot{\bar{\epsilon}}_{ij}x_j + \tilde{\mathbf{v}}_i(\mathbf{x})$. By imposing periodic boundary conditions, the
 962 velocity fluctuation field $\tilde{\mathbf{v}}_k(\mathbf{x})$ is assumed to be periodic across the boundary
 963 of the unit cell, while the traction field is antiperiodic, to meet equilibrium on
 964 the boundary between contiguous unit cells. The local constitutive equation
 965 that relates the deviatoric stress $\boldsymbol{\sigma}'(\mathbf{x})$ and the strain rate $\dot{\boldsymbol{\epsilon}}(\mathbf{x})$ at point \mathbf{x}
 966 is obtained from Eqs (18) to (20).

967 If $p(\mathbf{x})$ is the unknown pressure field introduced by the incompressibility
 968 constraint, the Cauchy stress field can be written as:

$$\boldsymbol{\sigma}(\mathbf{x}) = \mathbf{L}^0 : \dot{\boldsymbol{\epsilon}}(\mathbf{x}) + \boldsymbol{\varphi}(\mathbf{x}) - p(\mathbf{x})\mathbf{I} \quad (26)$$

969 where the polarization field $\boldsymbol{\varphi}(\mathbf{x})$ is given by:

$$\boldsymbol{\varphi}(\mathbf{x}) = \boldsymbol{\sigma}'(\mathbf{x}) - \mathbf{L}^0 : \dot{\boldsymbol{\epsilon}}(\mathbf{x}) \quad (27)$$

970 where \mathbf{L}^0 is the stiffness (viscosity) of a linear reference medium. Eqs. (26)
 971 and (27) amount to transform the actual heterogeneity problem into an
 972 equivalent one, corresponding to a homogenous medium with eigen-strain-
 973 rates. Note, however, that the above defined polarization field depends
 974 on the unknown $\dot{\boldsymbol{\epsilon}}(\mathbf{x})$. Combining Eq. (27) with the equilibrium and the
 975 incompressibility conditions gives:

$$L_{ijkl}^0 v_{k,lj}(\mathbf{x}) + \varphi_{ij,j}(\mathbf{x}) - p_{,i}(\mathbf{x}) = 0, v_{k,k}(\mathbf{x}) = 0 \quad (28)$$

976 Assuming for a moment that the polarization field $\boldsymbol{\varphi}(\mathbf{x})$ is known, the sys-
 977 tem of partial differential equations (28), with periodic boundary conditions
 978 across the unit cell boundary, can be solved by means of the Green function
 979 method.

980 If G_{km} and H_m are the periodic Green functions associated with the velocity

981 and hydrostatic pressure fields, the solutions of system (28) are convolution
 982 integrals between those Green functions and the actual polarization term.
 983 The velocity gradient, after some manipulation is given by:

$$\tilde{v}_{i,j}(\mathbf{x}) = \int_{R^3} G_{ik,jl}(\mathbf{x} - \mathbf{x}') \varphi_{kl}(\mathbf{x}') d\mathbf{x}'. \quad (29)$$

984 Convolution integrals in direct space are simply products in Fourier space.
 985 Hence:

$$\hat{\tilde{\epsilon}}_{ij}(\xi) = \hat{\Gamma}_{ijkl}^{sym}(\xi) \hat{\varphi}_{kl}(\xi), \quad (30)$$

986 where $\hat{\Gamma}_{ijkl}^{sym} = \text{sym}(\hat{G}_{ik,jl})$. The tensors $\hat{G}_{ik}(\xi)$ and $\hat{\Gamma}_{ijkl}^{sym}(\xi)$ are only func-
 987 tions of \mathbf{L}^0 and can be readily obtained for every point belonging to $\{\xi^d\}$
 988 (for details, see Lebensohn et al. (2008)). Now, taking into account the
 989 definition 27 of $\varphi(\mathbf{x})$, Eq. 29 is an integral equation where the velocity
 990 gradient appears in both sides, and, thus, it can be solved iteratively. As-
 991 signing initial guess values to the strain-rate field in the regular grid (e.g.
 992 $\tilde{\epsilon}(\mathbf{x}^d) = 0 \Rightarrow \dot{\epsilon}^{(0)}(\mathbf{x}^d) = \dot{\tilde{\epsilon}}$), and computing the corresponding stress field
 993 $\sigma^{(0)}(\mathbf{x}^d)$ from the local constitutive relation (18) allows to obtain an initial
 994 guess for the polarization field in direct space $\varphi^{(0)}(\mathbf{x}^d)$ (27), which in turn
 995 can be Fourier-transformed to obtain $\hat{\varphi}^{(0)}(\xi^d)$.

996 The rate of convergence of this fixed point technique is rather poor for
 997 nonlinear constitutive relations such as power-law relations between the
 998 stress and the strain-rate. Accelerated schemes based on augmented La-
 999 grangians have been proposed to improve this rate of convergence originally
 1000 by Michel et al. (2000, 2001) for composites, and later adapted by Lebensohn
 1001 (2001) for polycrystals to which the interested reader is referred for details.
 1002 Upon convergence, the stress at each material point can be used to calculate
 1003 the shear rates associated with each slip system (Eq. 4), from which fields
 1004 of relative activity of the basal, prismatic and pyramidal slip modes can be

1005 obtained, as well. While it is certainly possible to use the FFT-based for-
1006 mulation for the prediction of microstructure evolution, in this section we
1007 have restricted our analysis to the local fields that are obtained for a fixed
1008 configuration. In this sense, the high strain-rate regions predicted by the
1009 model (see below) should be regarded as precursors of localization bands.
1010 Evidently, microstructural changes that are not considered under this ap-
1011 proximation, like the eventual grain's and subgrain's morphologic evolution
1012 and rotation, as well as the possible occurrence of local strain hardening,
1013 may modify some of the trends observed in the initial micromechanical fields.
1014 In order to account for these microstructural changes, the FFT-based for-
1015 mulation has been coupled with the front-tracking numerical platform Elle
1016 (Bons et al., 2001). Results of this coupled model are reported in Section
1017 5.2.2.

1018 *4.1.2. Application to columnar ice deforming in the secondary creep regime.*

1019 Lebensohn et al. (2009) and Montagnat et al. (2011) applied this FFT
1020 method to simulate strain rate and stress fields, and local lattice misorienta-
1021 tions obtained at secondary creep in columnar ice polycrystals. Lebensohn
1022 et al. (2009) compared the simulated fields to a series of compression creep
1023 experiments performed by Mansuy et al. (2000, 2002) on laboratory-grown
1024 columnar ice samples characterized by multicrystals of controlled shape and
1025 orientations. The specimen used for this comparison (see Fig. 13) was a
1026 plate of 210×140 mm with a relatively thick (8 mm) section, consisting of
1027 a multicrystalline cluster, located in the center of the plate, with c-axes
1028 lying on the plane of the plate, and embedded in a matrix of fine-grained
1029 ice. This specimen was deformed under a compressive stress of 0.75 MPa
1030 exerted vertically in the plane at -10°C under plane strain conditions. Fig.

1031 13 shows, after 0.07 strain, three types of localization bands: basal shear
 1032 bands, kink bands and sub-boundaries, that change orientation to follow
 1033 crystallographic directions when they cross from one grain to another.
 1034 In this configuration, kink band boundaries are seen mainly inside grains
 1035 oriented close to 45° from the imposed compression direction. Kink bands,
 1036 described as a sharp or discontinuous change in orientation of the active
 1037 slip surface, had been reported in experimental studies conducted on 2-D
 1038 ice polycrystals (Wilson et al., 1986; Wilson and Zhang, 1994; Montagnat
 1039 et al., 2011). Sub-boundaries parallel to the c-axis were also observed.

1040

1041 The FFT-based calculation as described in the previous section was run
 1042 to obtain the overall and local mechanical response of the above-described
 1043 unit cell representing a columnar ice polycrystal, to the following imposed
 1044 strain-rate tensor (see also Fig. 14):

$$\dot{\epsilon}_{ij} = \begin{bmatrix} 1 \times 10^{-8} & 0 & 0 \\ 0 & -1 \times 10^{-8} & 0 \\ 0 & 0 & 0 \end{bmatrix} s^{-1} \quad (31)$$

1045 The crystallographic texture of the 2-D ice polycrystal consisting of colum-
 1046 nar grains with c-axes perpendicular to the axial (vertical) direction x_3 was
 1047 described in terms of a collection of Euler-angle triplets of the form $(\varphi_1, 90^\circ,$
 1048 $\varphi_2)$ (Bunge convention). The application of the FFT method required the
 1049 generation of a periodic unit cell or representative volume Element (RVE),
 1050 by repetition along x_1 and x_2 of a square domain. This square domain was
 1051 constructed in such a way that it contained the cross-sections of 200 colum-
 1052 nar grains, generated by Voronoi tessellation (see Fig. 14). This square do-
 1053 main is the cross-section of the unit cell, consisting of columnar grains with

1054 axes along x_3 and sections in the x_1 - x_2 plane. This unit cell was discretized
1055 using a $1024 \times 1024 \times 1$ grid of regularly-spaced Fourier points, resulting in
1056 an average of around 5250 Fourier points per grain. Note that the periodic
1057 repetition of this unit cell along x_3 determines infinitely long grains along
1058 this direction. Three specific orientations with c-axis respectively at 0° , 45° ,
1059 and 90° from the compression direction were forced to be among the set of
1060 200 (otherwise random) orientations assigned to the grains. For a plane-
1061 strain state, such that x_1 is the tensile direction and x_2 is the compression
1062 direction, the grain with $\varphi_1 = 45^\circ$ (45 deg grain in what follows) is theo-
1063 retically favorably oriented to deform by soft basal slip, while in the 0 deg
1064 and 90 deg grains, the hard pyramidal systems are the only ones favorably
1065 oriented to accommodate deformation. It is worth noting that due to the
1066 above plane-strain condition and the in-plane orientation of the c-axes, the
1067 prismatic slip systems are not well-oriented, for any φ_1 angle.

1068 The computed effective response of this kind of isotropic columnar ice
1069 polycrystal deformed in-plane is twice softer compared to an isotropic 3-D
1070 polycrystalline ice (Lebensohn et al., 2007). The computed overall relative
1071 activities of the different slip modes (i.e. 90.7%, 7.6% and 1.7% for basal,
1072 pyramidal and prismatic slip, respectively) show a preeminence of basal slip,
1073 a minor contribution of pyramidal slip and a very low activity of prismatic
1074 slip. Fig. 15 shows the computed equivalent strain-rate field for the entire
1075 unit cell, normalized with respect to the average equivalent strain rate ($\dot{\epsilon}_{eq} =$
1076 $1.15 \times 10^{-8} \text{s}^{-1}$). The main feature observed in this plot is a network of high
1077 strain-rate bands, precursors of localization bands (in what follows we will
1078 sometimes refer to them simply as "localization bands"). These bands are
1079 transmitted from grain to grain and are, in general, inclined with respect
1080 to the shortening and extension directions. They follow tortuous paths,

1081 sometimes with large deviations from $\pm 45^\circ$ (i.e. the macroscopic directions
1082 of maximum shear stress). They follow crystallographic directions (basal
1083 poles or basal planes) inside each grain. The predicted bands parallel or
1084 perpendicular to the c-axis were reasonably assumed to be kink or shear
1085 bands, respectively (see Lebensohn et al. (2009) for details). Some segments
1086 of these bands also follow favorably-oriented grain boundaries and frequently
1087 go through triple or multiple points between grains, in good agreement with
1088 some of the observations of (Mansuy et al., 2002) (Fig. 13). Fig. 16 shows in
1089 more details the predicted fields of equivalent strain rate (normalized to $\dot{\epsilon}_{eq}$),
1090 equivalent stress (in units of τ^{bas}) and relative basal activity, in the vicinities
1091 of the 45 deg grain. Two very intense (i.e. local strain rates higher than 10
1092 times the macroscopic strain rate) and parallel kink bands are seen inside
1093 the 45 deg grain, connected by several less intense shear bands (orthogonal
1094 to the pair of kink bands, lying on to the basal plane), in good agreement
1095 with Mansuy's experiments (see Fig. 13). The basal activity in the 45 deg
1096 grain is very high, although some regions of high non-basal activity can be
1097 observed between shear bands and immediately outside the kink bands. The
1098 latter is compatible with a low or even vanishing resolved shear stress on
1099 basal planes in those locations, which may be responsible for the formation
1100 of basal dislocation walls that are at the origin of a kink band (Mansuy
1101 et al., 2002). This correlation between kink band precursors and nearby
1102 localized high non-basal activity is systematic in these results. From the
1103 same detailed analysis performed around the 0 and 90 deg grains, a good
1104 match was found with experimental observations.

1105 In (Montagnat et al., 2011), the viscoplastic FFT-based approach was
1106 applied to the exact experimental microstructure of a compressive test per-
1107 formed on a 2D columnar sample. Samples (dimensions $\approx 10 \times 10 \times 1.5 \text{ cm}^3$)

1108 were grown in the laboratory under a uniaxial temperature gradient to reach
1109 a columnar microstructure with all c -axes lying parallel to the sample sur-
1110 face. In this work, the observed kink bands could be associated with mis-
1111 orientations between adjacent regions of a grain interior of more than 5° ,
1112 and their exact nature in term of dislocation arrangements were confirmed
1113 by EBSD measurements. Although the boundary conditions of the model-
1114 ing were slightly different from the experimental one, the model was able
1115 to predict the exact location of the localization bands. The bands were as-
1116 sociated with stress concentration that could reach five times the applied
1117 macroscopic stress, and to high levels of local non basal activity (see Fig.
1118 17). Nevertheless, the amplitude of the modeled lattice misorientations were
1119 always overestimated, and this was associated with the fact that very local
1120 grain boundary migration and new grain nucleation (dynamic recrystalliza-
1121 tion mechanisms) observed experimentally were not considered in the model
1122 (see Section 5.2.2).

1123 *4.2. Elasto-viscoplastic FFT approach*

1124 The full-field FFT approach described above has been extended very re-
1125 cently to the case of elasto-viscoplasticity, see (Idiart et al., 2006; Suquet
1126 et al., 2011; Lebensohn et al., 2012). As for purely viscoplastic behaviors,
1127 its application to highly anisotropic material like ice allows investigating the
1128 accuracy of elasto-viscoplastic mean-field models (see Section 3.6) since, as
1129 already mentioned, the FFT technique provides the “exact” (in a numerical
1130 sense) response of the specimen with the actual microstructure and local con-
1131 stitutive relations. Application to ice allows studying transient creep effects
1132 with more detail. Comparison with experimental strain field measured with
1133 an intragranular spatial resolution has been provided in (Grennerat et al.,

1134 2012) making use of the relative ease of producing samples with controlled
 1135 2-D microstructure, compared to other polycrystalline materials.

1136 *4.2.1. The mechanical problem*

1137 The method described in Suquet et al. (2011) considers the same mi-
 1138 crostructure description as in Section 4.1: a polycrystalline volume V com-
 1139 posed of several grains of different orientations, each grain obeying con-
 1140 stitutive relations defined in Section 2.3. The volume V is subjected to
 1141 a macroscopic loading path, which can be a prescribed history of average
 1142 strain, or a history of average stress or a combination of both. For simplicity,
 1143 the method is presented here assuming a prescribed history of macroscopic
 1144 strain $\bar{\boldsymbol{\varepsilon}}(t), t \in [0, T]$. Other types of loadings can be handled by different
 1145 methods described in (Michel et al., 1999) for instance.

1146 The local problem to be solved to determine the local stress and strain
 1147 fields in the volume element V consists of the equilibrium equations, com-
 1148 patibility conditions, constitutive relations and periodicity boundary condi-
 1149 tions:

$$\left\{ \begin{array}{ll} (\dot{\boldsymbol{\sigma}}, \dot{\boldsymbol{\tau}}_0, \dot{\mathbf{X}}) = \mathbf{F}(\dot{\boldsymbol{\varepsilon}}, \boldsymbol{\sigma}, \boldsymbol{\tau}_0, \mathbf{X}, \mathbf{x}, t), & \text{for } (\mathbf{x}, t) \in V \times [0, T], \\ \boldsymbol{\varepsilon}(\mathbf{x}, t) = \frac{1}{2}(\nabla \mathbf{u}(\mathbf{x}, t) + {}^T \nabla \mathbf{u}(\mathbf{x}, t)), & \\ \operatorname{div} \boldsymbol{\sigma}(\mathbf{x}, t) = 0 & \text{for } (\mathbf{x}, t) \in V \times [0, T], \\ \mathbf{u}(\mathbf{x}, t) - \bar{\boldsymbol{\varepsilon}}(t) \cdot \mathbf{x} \text{ periodic on } \partial V, & \text{for } t \in [0, T] \end{array} \right. \quad (32)$$

1150 The data of interest are the effective response $\bar{\boldsymbol{\sigma}}(t), t \in [0, T]$ of the poly-
 1151 crystal, the history of the average strain $\bar{\boldsymbol{\varepsilon}}(t), t \in [0, T]$, but also the local
 1152 fields $\boldsymbol{\sigma}(\mathbf{x}, t), \boldsymbol{\varepsilon}(\mathbf{x}, t)$ and other significant fields (internal variables, thermo-
 1153 dynamic forces etc...).

1154 The extension of the simplest version of the FFT-based method, also

1155 called the *basic scheme*, to constitutive relations including crystalline elasto-
1156 viscoplasticity relies on two ingredients:

- 1157 1. A time-integration scheme for the constitutive differential equations.
1158 The time interval of interest $[0, T]$ is split into time steps $[t_n, t_{n+1}]$. All
1159 quantities are assumed to be known at time t_n , and the quantities at
1160 time t_{n+1} are unknown. This time integration is performed at every
1161 point \mathbf{x}^d of the discretized polycrystal and the evolution problem is
1162 reduced to a problem for the stress and strain fields $\boldsymbol{\sigma}$ and $\boldsymbol{\varepsilon}$ at time
1163 t_{n+1} in the form

$$\boldsymbol{\sigma}_{n+1}(\mathbf{x}^d) = \mathcal{F}_{n+1}(\mathbf{x}^d, \boldsymbol{\varepsilon}_{n+1}(\mathbf{x}^d)) \quad (33)$$

- 1164 2. A FFT global scheme to solve the local problem for a nonlinear com-
1165 posite obeying Eq. (33).

1166 The algorithm developed applies to a wide class of constitutive relations,
1167 see (Suquet et al., 2011). As before, it is limited to specimens submitted
1168 to periodic boundary conditions. Results presented below are performed
1169 with the FFT-based program Craft (freely available at <http://craft.lma.cnrs->
1170 [mrs.fr](http://craft.lma.cnrs-mrs.fr)). For application to elastoviscoplasticity in ice, the local constitutive
1171 relation is the one provided above, see Eqs (2, 3, 6, 7, 8). It can also be
1172 formulated via the following differential equation:

$$\dot{\mathbf{Y}} = \mathbf{F}(\dot{\boldsymbol{\varepsilon}}, \mathbf{Y}, t), \quad (34)$$

1173 where

$$\mathbf{Y} = \begin{pmatrix} \boldsymbol{\sigma} \\ \tau_0^{(k)}, k = 1, \dots, M \\ X^{(k)}, k = 1, \dots, M \end{pmatrix},$$

$$\mathbf{F}(\dot{\boldsymbol{\varepsilon}}, \mathbf{Y}, t) = \begin{pmatrix} \mathbf{C} : \left(\dot{\boldsymbol{\varepsilon}} - \sum_{k=1}^M \dot{\gamma}^{(k)}(\mathbf{Y}) \boldsymbol{\mu}^{(k)} \right) \\ \left(\tau_{sta}^{(k)} - \tau_0^{(k)} \right) \sum_{\ell=1}^M h^{(k,\ell)} |\dot{\gamma}^{(\ell)}(\mathbf{Y})| \\ c^{(k)} \dot{\gamma}^{(k)}(\mathbf{Y}) - d^{(k)} X^{(k)} |\dot{\gamma}^{(k)}(\mathbf{Y})| - e^{(k)} |X^{(k)}|^m \text{sign} \left(X^{(k)} \right) \end{pmatrix} \quad (35)$$

1174 with \mathbf{C} the elastic stiffness ($\mathbf{C} = \mathbf{S}^{-1}$). The set of parameters used are
 1175 given in Table 1.

1176 *4.2.2. Application to strain field prediction in a 2D-1/2 configuration.*

1177 The elasto-viscoplastic FFT approach was used to predict strain and
 1178 stress field evolution during transient creep tests on ice polycrystals, in
 1179 comparison with experimental measurements performed by Grennerat et al.
 1180 (2012).

1181 Samples were grown following (Montagnat et al., 2011) (see Section 4.1.2).
 1182 This way, when compressed, (i) plastic deformation can be approximate as 2-
 1183 D, and (ii) strain fields measured at the specimen surface are representative
 1184 for the sample volume owing to the minimisation of in-depth microstructure
 1185 gradients. Average grain size (section perpendicular to the column direction)
 1186 was about 5 mm and most of the c-axes were oriented parallel to the surface

1187 ($\pm 15^\circ$). The microstructure and grain orientation were measured using an
1188 Automatic Fabric Analyzer (Russell-Head and Wilson, 2001) which provides
1189 orientation values with about $50 \mu\text{m}$ resolution, and 1° accuracy. A Digital
1190 Image Correlation technique (Vacher et al., 1999) was applied to measure
1191 the strain heterogeneities on the surface perpendicular to the column direc-
1192 tion. From displacement measurements performed during transient creep in
1193 ice, i.e. up to 1 to 2%, at -10°C , under 0.5 MPa, strain fields were evaluated
1194 with a resolution of about 0.2%, and at a spatial resolution of about 1 mm.

1195

1196 The experimental microstructures were implemented in the code using
1197 the fabric analyzer data of 2000×2000 pixels (but the model input does not
1198 need to be square). One pixel in the third dimension (column direction) is
1199 enough to reproduce the 2D-1/2 geometry thanks to the periodic boundary
1200 conditions.

1201 Fig. 18 presents the strain field measured experimentally at the end of
1202 the transient creep, and the simulated fields of strain and stress. Although
1203 simulated boundary conditions did not precisely match the experimental
1204 ones, the heterogeneities of the strain field that develop during transient
1205 creep of polycrystalline ice were reproduced well by the model (Grennerat
1206 et al., 2012). In particular, the model was able to reproduce the characteris-
1207 tic length of the heterogeneities being larger than the grain size, and scaling
1208 with the sample dimensions. Furthermore, both experimental and modeled
1209 results showed no correlation between the orientation of the c-axis and the
1210 strain intensity (see Fig. 19). This result casts doubt on the relevance of
1211 the distinction between "hard grains" and "soft grains" classically made for
1212 the analysis of ice mechanical behavior, and more generally for anisotropic
1213 materials.

1214 Fig. 20 represents the evolution of the simulated equivalent strain field from
1215 0.25 to 0.60% of compression during transient creep. As observed experi-
1216 mentally, the strain heterogeneities develop early during the transient creep
1217 and are reinforced up to about 10 times the imposed strain.

1218 **5. Modeling of dynamic recrystallization mechanisms**

1219 Under laboratory conditions (described in Section 1), dynamic recryst-
1220 tallization (DRX) dominates the changes of microstructures and fabrics in
1221 the tertiary creep regime, that is after about 1% macroscopic strain (Du-
1222 val, 1981; Jacka and Maccagnan, 1984; Jacka and Li, 1994). During DRX,
1223 grain nucleation and grain boundary migration are two processes that con-
1224 tribute to the reduction of the dislocation density, therefore of the stored
1225 deformation energy (Humphreys and Hatherly, 2004). In the laboratory,
1226 tertiary creep is a continuous sequence of deformation and recrystallization
1227 that gradually results in a steady state. This steady state is associated with
1228 an equilibrium grain size (Jacka and Li, 1994) and a girdle-type fabric with
1229 c-axes at about 30° from the compression axis (Jacka and Maccagnan, 1984),
1230 or with two maxima in simple shear (Bouchez and Duval, 1982).

1231 In polar ice sheets, DRX was identified from observation on ice thin sections
1232 along ice cores (Alley, 1992; Thorsteinsson et al., 1997; de la Chapelle et al.,
1233 1998; Kipfstuhl et al., 2006). Three regions are usually defined: (i) normal
1234 grain growth driven by the reduction of grain-boundary energy in the upper
1235 hundreds meters of the core, (ii) rotation recrystallization during which new
1236 grains are formed by the progressive lattice rotation of the subgrains in the
1237 main part of the core and (iii) migration recrystallization similar to the one
1238 observed in the laboratory, in the bottom part where the temperature is

1239 above -10°C (see Montagnat et al. (2009) and Faria et al. (this issue) for a
1240 review).

1241 Recrystallization and grain growth significantly influence the microstruc-
1242 ture, the fabric and therefore the mechanical properties. To be able to in-
1243 tegrate these mechanisms in the modeling of ice deformation is therefore
1244 crucial for an accurate prediction of its behavior.

1245 *5.1. Dynamic recrystallization within mean-field approaches*

1246 Several attempts were made to integrate dynamic recrystallization mech-
1247 anisms into mean-field approaches as described in Section 3.

1248 On the basis of the VPSC scheme (tangent version) described in Section 3
1249 for the description of the mechanical behavior, Wenk et al. (1997) developed
1250 a nucleation and grain-growth model to represent DRX in anisotropic ma-
1251 terials such as ice. The model is based on the hypothesis that grains with
1252 a high stored energy (highly deformed) are likely to nucleate new grains
1253 and become dislocation-free. They may also be invaded by their neighbors
1254 which have a lower stored energy. Depending on the respective importance
1255 of nucleation and grain boundary migration processes, the recrystallization
1256 textures are expected to favor either highly deformed components or less
1257 deformed ones.

1258 One must first remember that, in the VPSC scheme, grains are represented
1259 by inclusions in an homogenous equivalent medium (HEM). Grain interac-
1260 tions are therefore represented "averaged" through the interaction between
1261 the inclusion and the HEM.

1262 In this model, nucleation is represented, by a probability of nucleation P
1263 per time increment Δt for each deformation step:

$$P \propto \Delta t \times \exp(-A/E^2) \quad (36)$$

1264 The constant A depends on the grain boundary energy and was taken as
 1265 an adjustable parameter. E is a proxy of the stored energy, $E \propto \sum_s (\Delta\tau_0^s)$
 1266 with $\Delta\tau_0^s$ the variation of the critical resolved shear stress on the system s
 1267 during the deformation step. This calculation supposes a hardening law for
 1268 each slip system to be defined. An isotropic hardening law was chosen in the
 1269 form $\dot{\tau}_0^s = H \sum_s \dot{\gamma}^s$, with hardening matrix H being isotropic. A threshold
 1270 was then defined for the minimum strain energy to nucleate, and the new
 1271 grain completely replaced the old one (same size, same orientation), with a
 1272 stored energy equal to zero.

1273 The grain boundary migration rate was taken proportional to the difference
 1274 in stored energy between the grain and the average, i.e., the HEM. The de-
 1275 velopment of the microstructure is therefore a balance between nucleation
 1276 and growth. Adjustable parameters were varied arbitrarily for comparison
 1277 purpose.

1278 Applied to ice, this model resulted into weaker fabrics than the one ob-
 1279 tained by the classical VPSC tangent approach, mostly because grains near
 1280 the compression axis disappeared (high stored energy) and only a few girdle
 1281 grains, and a few grains exactly aligned with the compression axis from the
 1282 beginning, remained.

1283

1284 Thorsteinsson (2002) included some DRX in its Nearest-Neighbor Inter-
 1285 action (NNI) model described in Section 3. Polygonization associated with
 1286 rotation (or continuous) recrystallization is accounted for by comparing the
 1287 resolved shear stress in the crystal ($|\sum_s \tau_s \hat{\mathbf{b}}_s|$) to the applied stress (with
 1288 τ_s the shear stress on system s , and $\hat{\mathbf{b}}_s$ a unit vector in the direction of the
 1289 Burgers vector). If the ratio is smaller than a given value, and the disloca-
 1290 tion density higher than a given value, then the crystal size is halved and

1291 both new grains are rotated by a fixed $\Delta\theta$ of 5° . Grain growth occurs by
1292 normal grain growth according to (Gow, 1969; Alley et al., 1986) parabolic
1293 law ($D^2 - D_0^2 = Kt$). The grain growth factor K follows an Arrhenius-type
1294 dependence on the temperature. To take into account the grain growth as-
1295 sociated with the difference in dislocation-stored energy between the grain i
1296 and the average, this growth factor was modified into ($\tilde{K} = (E_{disl}^{av} - E_{disl}^i)K'$)
1297 with K' a constant depending on temperature and impurities.

1298 Migration recrystallization is included in the model by considering the bal-
1299 ance between grain-boundary energy, and stored energy associated with dis-
1300 locations (the stored energy is calculated following (Wenk et al., 1997), as
1301 just described, and translated into dislocation density). A crystal recrystal-
1302 lizes (i.e. is replaced by a crystal with initial dislocation density ρ_0) when
1303 the dislocation energy is higher than the grain-boundary energy. This as-
1304 sumption relies on the hypothesis that stored energy is released by normal
1305 grain growth (driven by GB energy), and that dynamic recrystallization only
1306 occurs if this relaxation is not efficient enough to decrease the dislocation
1307 density. The size of the new crystal is adjusted with the effective stress fol-
1308 lowing (Guillopé and Poirier, 1979; Jacka and Li, 1994) and its orientation
1309 is chosen at random in the range of the "softest" orientations in the applied
1310 stress state.

1311 Modeling results were obtained for comparison to a case similar to the GRIP
1312 ice core, with vertical compression, and rotation recrystallization domi-
1313 nating. The introduction of polygonization allows for the preferential re-
1314 moval of "hard" grains, which leads to a weaker fabric compared to the
1315 "no-recrystallization" case. In particular, when associated with the NNI
1316 formulation, the model is able to reproduce fabrics quite similar to those
1317 measured along the GRIP ice core at several depths. "Girdle-type" fabric

1318 similar to the experimental fabrics, results from the introduction of migra-
1319 tion recrystallization. However, parametrization remains weak, in particular
1320 the estimation of the dislocation density, and of the recrystallized grain ori-
1321 entations.

1322

1323 The last example presented here is the cellular automaton model for
1324 fabric development by Ktitarev et al. (2002) and Faria et al. (2002). The
1325 application was mostly to reproduce the fabric measured along deep ice
1326 cores, with the assumption of deformation under uniaxial compression. The
1327 cellular automaton (CA) frame is especially suitable for simulation of sys-
1328 tems represented by a certain number of cells, which are associated with
1329 generalized state variables and arranged in regular environment. The con-
1330 sidered material is a thin horizontal layer of ice located along the ice core,
1331 thin enough so that it is considered homogeneous in the vertical dimension.
1332 To discretize the problem according to the CA method, the authors took a
1333 one-dimensional lattice of equal cells representing the grains, described by
1334 their size, and their orientation. The basic dynamical quantity of the al-
1335 gorithm is the dislocation density. This density increases with deformation
1336 and depends on the orientation of the grain. Recrystallization mechanisms
1337 proceed when a critical value is reached. Normal grain growth is accounted
1338 for following Gow (1969) and is apparently the only growth mechanism asso-
1339 ciated with polygonization mechanisms. The increase in dislocation density
1340 is associated with the resolved shear stress on the basal system and the re-
1341 crystallization model developed in Montagnat and Duval (2000) is used to
1342 estimate the evolution of the density in relation with grain size and polygo-
1343 nization mechanisms. Rotation of grains is ruled by a kinematic equation
1344 based on the inelastic spin, assuming a compressive stress proportional to the

1345 depth along the core, and a linear dependence between the shearing rate of
1346 sliding on the basal system and the resolved shear stress. The time evolution
1347 was related to the depth along the core using the Dansgaard et al. (1993)
1348 relation. Following Duval and Castelnau (1995), migration recrystallization
1349 was only applied below 2800 m depth. During migration recrystallization,
1350 new grains were allowed to grow much faster by consuming up to ten cells
1351 at every time step, until it is impinged by another growing grain, or until it
1352 reaches the critical size of the steady state.

1353 The model was able to provide a good qualitative evolution of the grain
1354 size, by separating the influence of normal grain growth, polygonization and
1355 migration recrystallization similarly to what was suggested from the mea-
1356 surements along the GRIP ice core (Thorsteinsson et al., 1997; de la Chapelle
1357 et al., 1998). Concerning the fabric evolution, the model was able to pre-
1358 dict the evolution toward a single maximum, but the kinetics is too strongly
1359 influenced by the polygonization, and further by migration recrystallization.

1360

1361 *5.2. Dynamic recrystallization within full-field approaches*

1362 This section presents a coupling between a platform for structural change
1363 in materials (Elle) with the full-field FFT approach presented in Section 4.1,
1364 to predict the microstructure evolution of ice polycrystals during dynamic
1365 recrystallization. A critical step in the development of generic models linking
1366 plastic deformation and recrystallization is the incorporation of the interac-
1367 tion between intra- and intergranular heterogeneities of the micromechanical
1368 fields (i.e. strain rate and stress) and the recrystallization processes. Be-
1369 cause local rotations of the crystal lattice are controlled by local gradients of
1370 plastic deformation, heterogeneous distributions of lattice orientations are

1371 observed at the grain and subgrain scale, see Section 4. This has a strong
1372 influence on recrystallization as this is a process driven by the local gradi-
1373 ents of energy (e.g. grain boundary or stored strain energy). Traditional
1374 mean-field models used to predict microstructure evolution during recryst-
1375 tallization are based on a simplified description of the medium and cannot
1376 fully describe intragranular heterogeneities (Section 5.1). Therefore, explicit
1377 full-field approaches are required for a better understanding of dynamic re-
1378 crystallization and prediction of microstructure evolution at large strain.

1379

1380 *5.2.1. The Elle modeling platform*

1381 Elle is a platform for the numerical simulation of processes in rocks
1382 and grain aggregates, with particular focus on (micro-) structural changes
1383 (Jessell et al., 2001; Jessell and Bons, 2002; Bons et al., 2008; Piazzolo et al.,
1384 2010). The simulations act on an actual 2D image of the microstructure
1385 (Fig. 21.a). Elle is currently restricted to 2D cases although the underlying
1386 principles for 2D are equally valid in 3D (Becker et al., 2008), and therefore
1387 the approach could be converted for 3D simulations.

1388 The central philosophy of Elle is to enable the coupling of processes
1389 that act on the material, recognizing that the effect of one process may
1390 significantly alter that of a concurrent process. Dynamic recrystallization,
1391 for example, can greatly change crystallographic preferred orientations in
1392 mineral aggregates deforming by dislocation creep (Jessell, 1988a,b). Cou-
1393 pling of processes is achieved in Elle using the principle of operator splitting,
1394 whereby individual processes successively act on the model in isolation, for
1395 a small time step. This approach greatly simplifies coding, as the coupling
1396 between processes needs not be programmed itself, but emerges from their

1397 alternating effect on the model.

1398 Each process in Elle is an individual program or module. A shell-script
1399 takes the starting model and then passes it in a loop to the individual pro-
1400 cesses, which each in turn modify the model slightly. Each loop represents
1401 one time step. The user can freely determine the mix of processes that op-
1402 erate by choosing which ones to include in the loop. The relative activity
1403 of individual processes is determined by the parameters passed on to each
1404 process.

1405 The model is essentially defined by two types of nodes: boundary nodes
1406 (bnodes) and unconnected nodes (unodes) (Fig. 21.b). Bnodes define the
1407 boundaries of a contiguous set of polygons (termed flynnns). These flynnns
1408 typically represent single grains, but can also represent regions within a
1409 material, for example rock layers (Llorens et al., 2012). The boundaries of
1410 the flynnns are formed by straight segments that connect neighboring bnodes.
1411 One bnode can be connected by either two or three other bnodes. The use
1412 of bnodes and flynnns makes the model suitable for a range of Finite Element
1413 and front-tracking models.

1414 Unodes form a second layer of the model. These are nodes that do not
1415 necessarily have fixed neighborhood relationships and typically represent
1416 points within the material. Some processes are not amenable to be modeled
1417 with polygons, but are best simulated with a regular grid of unodes. The
1418 FFT code is an example. Nodes and flynnns can have a range of attributes
1419 assigned to them, such as c-axis orientation, boundary properties, etc.

1420 Elle uses fully wrapping boundaries. A flynn that touches one side of
1421 the model continues on the other side (Fig. 21.a). The model is thus effec-
1422 tively a unit cell that is repeated infinitely in all directions. Although Elle
1423 typically uses a square model, deformation may change the unit cell into a

1424 parallelogram shape.

1425 Elle now includes a large and ever growing number of process modules for
1426 a variety of processes that mostly relate to microstructural developments in
1427 mineral aggregates. Each process can essentially act on the model in only
1428 two ways: changing the position of a node (e.g. a bnode in case of grain
1429 boundary migration) or changing the value(s) of attributes of flynns or nodes
1430 (e.g. concentration at a unode in a diffusion simulation). Some of the most
1431 relevant current processes are:

1432 • Normal grain growth driven by the reduction of surface energy, and
1433 hence curvature of grain boundaries. This process was used by Roes-
1434 siger et al. (2011) to address the issue of the competition between
1435 grain growth and grain size reduction in the upper levels of polar ice
1436 caps (Mathiesen et al., 2004). Surface energy can be anisotropic, i.e.
1437 depending on the lattice orientation of the grains on either side of the
1438 boundary (Bons et al., 2001). Two-phase grain growth has been ap-
1439 plied to grain growth in rocks with a small proportion of melt (Becker
1440 et al., 2008) and to ice with air bubbles (Fig. 21)(Roessiger et al. this
1441 volume).

1442

1443 • The Finite Element module Basil is used for incompressible power-law
1444 viscous deformation (Barr and Houseman, 1996). Using viscosities
1445 that are assigned to flynns, it calculates the stress and velocity fields
1446 resulting from applied boundary conditions. It has been used to study
1447 the behaviour of rigid inclusions in a deforming matrix (Bons et al.,
1448 1997), the behaviour of deforming two-phase materials as a function of
1449 viscosity contrast and composition (Jessell et al., 2009) and for folding

1450 of layers (Llorens et al., 2012). The wrapping boundaries of the Elle
1451 model, in combination with continuous remeshing allows for arbitrarily
1452 high strains (Jessell et al., 2009). In combination with grain growth
1453 and dynamic viscosity, Jessell et al. (2005) studied strain localisation
1454 behaviour. Durand et al. (2004) investigated the influence of uniaxial
1455 deformation on grain size evolution in polar ice cores and its influence
1456 on ice dating methods.

1457 • Dynamic recrystallisation includes grain boundary migration driven
1458 by strain energy (dislocation density) and the formation of new grain
1459 boundaries by progressive subgrain rotation or polygonisation (Urai
1460 et al., 1986). In the next section (5.2.2) we will describe how these
1461 processes, employing a front-tracking model for grain-boundary mi-
1462 gration, are linked with the FFT approach (Griera et al., 2011, 2012;
1463 Piazzolo et al., 2012) to model the stress and strain-rate fields and the
1464 driving forces for recrystallization.

1465 • A final Elle module of potential relevance to ice is that developed by
1466 Schmatz (2010) for the interaction between migrating grain bound-
1467 aries and small particles (e.g. dust or clathrates). The particles are
1468 represented by unodes, which, when swept by a grain boundary, can
1469 latch onto that boundary. Particles can slow down grain boundary
1470 movement, but can also be dragged along and eventually be released
1471 by a grain boundary.

1472 Summarizing, Elle provides a large number of routines to simulate grain-
1473 scale processes in minerals and rocks, and hence in glacial or polar ice. The
1474 open and versatile code allows for more process modules to be added or
1475 existing ones to be tailored for application to ice. A significant advantage of

1476 the code is that it enables the investigation of the complex microstructural
1477 and mechanical effects of multiple, concurrent and coupled processes.

1478 *5.2.2. Coupling Elle platform to FFT approach*

1479 Most of the numerical approaches used to simulate deformation and mi-
1480 crostructural evolution of rocks and metals are based on combining defor-
1481 mation approaches based on the Finite Element Method with Monte Carlo,
1482 cellular automaton, phase field, network or level-set methods to simulate
1483 recrystallization (Jessell, 1988a,b; Raabe and Becker, 2000; Piazzolo et al.,
1484 2002, 2010, 2012; Solas et al., 2004; Battaile et al., 2007; Logé et al., 2008).
1485 An alternative to these methods is the numerical scheme used in this study
1486 based on the coupling between the crystal plasticity FFT-based code (Leben-
1487 sohn, 2001) (section 4.1) and the Elle modeling platform just described
1488 (Bons et al., 2008). Both codes have been previously explained and here
1489 we only concentrate on some particularities of the coupling between them.
1490 The FFT-based formulation is integrated within the Elle platform using
1491 a direct one-to-one mapping between data structures. The polycrystalline
1492 aggregate is discretized into a periodic, regular array of spaced and uncon-
1493 nected nodes (Fourier Points in the FFT and "unconnected nodes", unodes,
1494 in Elle; Fig. 21).

1495 Numerical simulation is achieved by iterative application of small time
1496 steps of each process. After numerical convergence of the FFT model, data is
1497 transferred to Elle assuming that the micromechanical fields are constant in
1498 the incremental time step. The position and material information of unodes
1499 are directly updated because they are equivalent to the Fourier points, while
1500 position of boundary nodes (bnodes) are calculated using the velocity field.
1501 Based on the evolution of the predicted local lattice rotation field, the dislo-

1502 cation density can be estimated using strain gradient plasticity theory (e.g.
1503 Gao et al. (1999); Brinckmann et al. (2006)) or using the dislocation density
1504 tensor or Nye tensor (Nye, 1953; Arsenlis and Parks, 1999; Pantleon, 2008).
1505 With this approach, only geometrical necessary dislocations required to en-
1506 sure strain compatibility are estimated. To simplify the problem, we use
1507 a scalar approach where all dislocations are assumed to be related to the
1508 basal plane. The lattice-orientation and dislocation-density fields provide
1509 the input parameters to predict recrystallization in the aggregate.

1510 Recrystallization is simulated by means of three main processes: nucle-
1511 ation, subgrain rotation and grain boundary migration. Using the kinematic
1512 and thermodynamic instability criteria of classical recrystallization theory
1513 (Humphreys and Hatherly, 2004; Raabe and Becker, 2000), nucleation is
1514 simulated by the creation of a small new, dislocation-free flynn when the
1515 local misorientation or dislocation density exceeds a defined threshold. The
1516 lattice orientation of the new grain is set to that of the critical unode. When
1517 a cluster of unodes within a grain share the same orientation that is different
1518 from the rest of the unodes in that grain, a new grain boundary is created,
1519 while preserving the lattice orientations of the unodes. A technical limita-
1520 tion is that nucleation of grains and subgrains is only allowed along grain
1521 boundaries. Nucleation within grains are therefore not possible.

1522 Grain boundary migration is described by a linear relationship between
1523 velocity (v) and driving force per unit area (Δf), by $v = M\Delta f$ where M
1524 corresponds to the grain boundary mobility, which has an Arrhenius-type
1525 dependency on temperature. Grain boundary curvature and stored strain
1526 energies are used as driving forces for grain boundary motion. For this

1527 situation, the driving force can be defined as

$$\Delta f = \Delta E - 2\gamma/r \quad (37)$$

1528 where ΔE is the difference of stored strain energy across the boundary, γ
1529 is the boundary energy and r is the local radius of curvature of the grain
1530 boundary. Stored strain energy is the energy per unit volume associated
1531 with lattice distortions and depends on the dislocation density (ρ) and dis-
1532 location type. Grain boundary motion is simulated using the free-energy
1533 minimization front-tracking scheme of (Becker et al., 2008). When an un-
1534 ode is swept by a moving grain boundary, it is assumed that dislocations
1535 are removed and the new lattice orientation is that of the nearest unode
1536 belonging to the growing grain.

1537 Following the Elle philosophy, each process runs individually, following a
1538 pre-established sequence. After all Elle processes have run, the unodes layer
1539 is used to define the new input microstructure to be deformed viscoplasti-
1540 cally by the FFT code. A drawback is that the unodes are not following a
1541 regular mesh, a requirement needed by the FFT approach. For this reason,
1542 as proposed by Lahellec et al. (2003), and later adapted in the context of
1543 Elle by Grier et al. (2011, 2012), a particle-in-cell method is used to remap
1544 all material and morphological information to a new regular computational
1545 mesh. In order to avoid unrealistic crystallographic orientations, these are
1546 not interpolated during remapping. The crystallographic orientation of a
1547 new Fourier Point that belongs to a specific grain is that of the nearest un-
1548 ode that belongs to the same grain. This allows to run numerical simulation
1549 up to large strains.

1550 *5.2.3. Application to creep experiments and natural ice*

1551 An example of numerical simulation using the FFT/Elle approach is
1552 shown in Fig. 22. The simulation is based on a creep experiment of poly-
1553 crystalline columnar ice. Samples and experimental conditions are those
1554 of (Montagnat et al., 2011) described in Section 4.1.2. The specimen was
1555 deformed at -10°C under uniaxial conditions with a constant load of 0.5
1556 MPa up to an axial strain of 4%. A thin section of the initial and the
1557 final microstructure was analyzed using the Automatic Ice Texture Ana-
1558 lyzer method (Russell-Head and Wilson, 2001) to obtain the local c-axis
1559 orientations. After a 4% of shortening, the onset of local recrystallization
1560 is evident in the experiment (Fig. 22a), in the form of irregular and ser-
1561 rated grain boundaries and small new grains that are preferentially located
1562 at triple junctions and along grain boundaries. Localized variations in the
1563 orientation of the basal plane form sharp and straight subgrain boundaries
1564 that indicate intracrystalline deformation. The experimental c-axis map was
1565 used as input for the FFT/Elle simulation. The experimental starting mi-
1566 crostructure was discretized into a grid of 256×256 Fourier points. As only
1567 the c-axis orientation is known, the other axes are given a random orienta-
1568 tion. Crystal plasticity is described with an incompressible rate-dependent
1569 equation for basal, prismatic and pyramidal slip (see Section 3). Critical
1570 resolved shear stress for basal slip was set 20 times lower than for non-basal
1571 systems. The physical properties used for recrystallization are as follows:
1572 mobility $M = 1 \times 10^{-10} \text{ m}^2\text{Kg}^{-1}\text{s}^{-1}$ (e.g. Nasello et al., 2005), isotropic
1573 boundary energy $\gamma = 0.065 \text{ Jm}^{-2}$ (Ketcham and Hobbs, 1969), shear mod-
1574 ulus $G = 3 \times 10^9 \text{ Pa}$ and critical dislocation density $\rho = 1 \times 10^{12} \text{ m}^{-2}$ (de la
1575 Chapelle et al., 1998). Pure shear boundary conditions were imposed with

1576 vertical constant strain rate of $-1 \times 10^{-8} \text{ s}^{-1}$ up to a 4% of strain in 1%
1577 increments.

1578 The computed orientation map and grain boundary misorientation are
1579 shown in Fig. 22b. Several features of the experiment are seen in the
1580 numerical simulation, such as the development of sharp misorientations or
1581 kink bands, bulging and serrated grain boundaries, and new grains at triple
1582 junction and grain boundaries. There is a good correlation between loca-
1583 tion of kink bands in the experiment and the simulation. However, the
1584 width of kink bands in the simulation is dependent on the numerical reso-
1585 lution. A relationship between grain boundary motion/nucleation and high
1586 dislocation-density regions is observed (Fig. 23). Variations in dislocation
1587 densities across grain boundaries lead to migration of these boundaries in
1588 the direction of the dislocation density gradient. However, some discrepan-
1589 cies are also seen, such as, for example, grain boundary motion (e.g. at the
1590 bottom-left part) that was not observed in the experiment. One explanation
1591 may be that low and high angle grain boundaries were not differentiated in
1592 the simulation and, therefore, both types had similar mobility.

1593

1594 A second example aims to show the strong effect recrystallization can
1595 have on the final microstructure. A $10 \times 10 \text{ cm}^2$ microstructure with 1600
1596 grains with random c-axis orientations (Fig. 24a) was deformed to 40%
1597 shortening in plane-strain pure shear. The values of mechanical (slip sys-
1598 tems, CRSS, etc) and recrystallization (mobility, surface energy, etc) prop-
1599 erties are similar to those of the model described before, but adjusted to a
1600 natural strain rate of 10^{-12} s^{-1} at about -30°C . Fig. 24b shows the c-axis and
1601 relative misorientation maps for an extreme case with no recrystallization
1602 (FFT only). Dominant red and purple colors indicate that the c-axis of crys-

1603 tallites are preferentially oriented at low angles to the shortening direction.
1604 Elongated grains are oriented parallel to the stretching direction. Remark-
1605 able differences are observed when recrystallization is activated (Fig. 24c).
1606 Grain boundaries are smooth and grains larger and more equidimensional.
1607 Despite the significant difference in microstructure, both simulations show a
1608 single maximum c-axis distribution at low angle to the shortening direction.
1609 The strong resemblance of the simulated microstructure with that of natural
1610 ice (Thorsteinsson et al., 1997; de la Chapelle et al., 1998; Weikusat et al.,
1611 2009) shows the strong potential of modeling of ice deformation based on
1612 an actual map of the microstructure.

1613 **6. Toward large scale ice flow modeling**

1614 A number of models have been developed in glaciology to simulate the
1615 flow of anisotropic ice and the strain-induced development of fabric within
1616 polar ice-sheets. Accounting for ice anisotropy in an ice-flow model implies
1617 to (i) build a macroscopic anisotropic flow law whose response will depend
1618 on the local fabric and (ii) have a proper description of the ice fabric at
1619 each node of the mesh domain and be able to model the fabric evolution as
1620 a function of the flow conditions. We hereafter present the main issues to
1621 address these two points.

1622 Due to the scale of these large ice-masses, the implementation of a poly-
1623 crystalline law must stay simple enough and numerically tractable. At
1624 present, full-field or even homogenization models presented previously are
1625 computationally too demanding and cannot realistically be used to estimate
1626 the mechanical response in an ice-sheet flow model. Here we present two ap-
1627 proaches to build a simple and efficient macroscopic law for polycrystalline

1628 ice. The first one is based on the concept of a scalar enhancement factor
1629 function so that the collinearity between the strain-rate and the deviatoric
1630 stress tensors is conserved (Placidi and Hutter, 2006), see Section 6.1. The
1631 second polycrystalline law is fully orthotropic and depends on six relative
1632 viscosities, function of the fabric (Gillet-Chaulet et al., 2005, 2006), see Sec-
1633 tion 6.2. Both models are phenomenological and must be calibrated using
1634 experimental or numerical results, as described below.

1635 With regards to other materials, the advantage of the hexagonal symme-
1636 try of ice is that the crystal rheology can be assumed transversally isotropic
1637 (only true for a linear rheology). Under this assumption, only one unit vector
1638 suffices to describe the lattice orientation, thus simplifying the mathemat-
1639 ical description of fabrics. With regards to other materials, the advantage
1640 of the hexagonal symmetry of ice is that only one unit vector suffices to de-
1641 scribe the lattice orientation, thus simplifying the mathematical description
1642 of fabrics. The discrete description of the fabric, *i.e.* a couple of angles for
1643 each crystal, would require too large a number of variables to be stored at
1644 each node of the domain mesh. Typical mesh size are hundreds of thousand
1645 nodes in 3D (Seddik et al., 2011) up to few millions for the most recent appli-
1646 cations (Gillet-Chaulet et al., 2012). The use of a parameterized orientation
1647 distribution function (ODF) would decrease the number of parameters, but
1648 evolution equations for these parameters to describe the fabric evolution
1649 cannot be obtained in a general case (Gagliardini et al., 2009). The ori-
1650 entation tensors, which describe the fabric at the macroscopic scale in a
1651 condensed way are more suitable. Five parameters are needed to describe
1652 an orthotropic fabric (the two eigenvalues of the second-order orientation
1653 tensor and the three Euler angles to specify the position of the material
1654 symmetry basis), and an evolution equation for the second-order orienta-

1655 tion tensor can be easily derived from the macroscopic stress and strain-rate
1656 fields.

1657 *6.1. Continuous Diversity and the CAFFE model*

1658 The CAFFE model (Continuum-mechanical Anisotropic Flow model based
1659 on an anisotropic Flow Enhancement factor) results from a suitable com-
1660 bination of two basic concepts: a power law description of ice rheology
1661 resembling the well-known Glen’s flow law (Glen, 1955); and a multiscale
1662 approach to model the evolution of the polycrystalline microstructure of ice
1663 based on the general theory of continuous diversity (Faria, 2001; Faria and
1664 Hutter, 2002; Faria et al., 2003).

1665 The ideas leading to the CAFFE model have been elaborated in a series
1666 of works by Luca Placidi and his collaborators (Placidi, 2004, 2005; Placidi
1667 and Hutter, 2005, 2006; Placidi et al., 2004). These ideas culminated in the
1668 definitive CAFFE formulation, presented by Placidi et al. (2010), in which
1669 the so-called enhancement factor of Glen’s flow law becomes a function of
1670 the material anisotropy (fabric), and the evolution of the latter is governed
1671 by an orientation-dependent mass balance equation derived from the theory
1672 of continuous diversity applied to glacier and ice-sheet dynamics (Faria,
1673 2006a,b; Faria et al., 2006).

1674 The greatest strength of the CAFFE model is its successful compromise
1675 between accuracy and flexibility, which allows one to upgrade existing com-
1676 puter models of isotropic ice-sheet dynamics based on Glen’s flow law into
1677 efficient anisotropic models, without profound changes in the original code.
1678 In fact, due to its relative simplicity, the CAFFE model has already been
1679 implemented in several numerical ice-flow simulations. For instance, it has
1680 been used by Seddik et al. (2008) and Bargmann et al. (2011) to simulate

1681 the ice flow at the site of the EPICA-DML drill site at Kohnen Station,
 1682 Dronning Maud Land, East Antarctica, while Seddik et al. (2011) used it
 1683 to simulate the ice flow in the vicinity of the Dome Fuji drill site in central
 1684 East Antarctica.

1685 In the following, we review the CAFFE formulation presented by Placidi
 1686 et al. (2010). The fundamental idea is to regard polycrystalline ice as a
 1687 "mixture" of lattice orientations, following the philosophy of the theory
 1688 of Mixtures with Continuous Diversity (MCD) proposed by Faria (2001,
 1689 2006a). Succinctly, a mixture with continuous diversity is a multicompo-
 1690 nent medium made up of an infinite number of mutually interacting species,
 1691 whose distinctive properties vary smoothly from one to another.

1692 In the case of polycrystalline ice, species are distinguished by their c-axis
 1693 orientations. Each point of the continuous body is interpreted as a represen-
 1694 tative volume element, which encompasses a large number of crystallites with
 1695 their own c-axis orientations. Each of such orientations is mathematically
 1696 identified with a point on the surface of the unit sphere \mathcal{S}^2 and represented
 1697 by a unit vector $\mathbf{n} \in \mathcal{S}^2$. As a consequence, for each species one can intro-
 1698 duce a mass density field $\varrho^*(\mathbf{x}, t, \mathbf{n})$, given at a certain position \mathbf{x} within the
 1699 polycrystal, and at time t , sometimes called orientational mass density, such
 1700 that, when integrated over the whole unit sphere, the usual mass density
 1701 field of the polycrystal (i.e. of the "mixture") results:

$$\varrho(\mathbf{x}, t) = \int_{\mathcal{S}^2} \varrho^*(\mathbf{x}, t, \mathbf{n}) d^2n, \quad (38)$$

1702 where d^2n ($= \sin \theta d\theta d\phi$ in spherical coordinates) is the infinitesimal solid
 1703 angle on the unit sphere \mathcal{S}^2 . The product $\varrho^*(\mathbf{x}, t, \mathbf{n}) d^2n$ is the mass fraction
 1704 of crystalline material in the volume element with c-axis directed towards
 1705 \mathbf{n} within the solid angle d^2n . Therefore, assuming that the material is

1706 incompressible, the mass (or volume) fraction ϱ^*/ϱ can be interpreted as
 1707 the usual orientation distribution function (ODF) in the context of materials
 1708 science (Bunge, 1993; Zhang and Jenkins, 1993; Raabe and Roters, 2004).
 1709 It should be remarked that in the glaciological literature the term "ODF"
 1710 sometimes refers to the relative number, instead of the mass (or volume)
 1711 fraction, of grains with a certain orientation.

1712 The time evolution of ϱ^* is governed by the balance equation of species
 1713 (orientational) mass

$$\frac{\partial \varrho^*}{\partial t} + \operatorname{div}(\varrho^* \mathbf{v}) + \operatorname{div}_{\mathbf{n}}(\varrho^* \mathbf{u}^*) = \varrho^* \Gamma^* \quad (39)$$

1714 with

$$\begin{aligned} \operatorname{div}_{\mathbf{n}}(\Phi^*) &= \operatorname{tr}[\operatorname{grad}_{\mathbf{n}}(\Phi^*)], \\ \operatorname{grad}_{\mathbf{n}}(\Phi^*) &= \frac{\partial \Phi^*}{\partial \mathbf{n}} - \left(\frac{\partial \Phi^*}{\partial \mathbf{n}} \cdot \mathbf{n} \right) \mathbf{n} \end{aligned} \quad (40)$$

1715 for any scalar-, vector- or tensor-valued field $\Phi^*(\mathbf{x}, t, \mathbf{n})$. In (39), $\mathbf{u}^*(\mathbf{x}, t, \mathbf{n})$
 1716 denotes a sort of "velocity" on the unit sphere (with $\mathbf{u}^* \cdot \mathbf{n} = 0$), called
 1717 orientational transition rate. Further, $\Gamma^*(\mathbf{x}, t, \mathbf{n})$ is the specific recrystal-
 1718 lization rate, which describes the rate of change of mass (per unit mass) of
 1719 one species into another one with different orientation. Integration of (39)
 1720 over the unit sphere \mathcal{S}^2 gives rise to the usual mass balance equation for the
 1721 polycrystal (i.e. the "mixture")

$$\begin{aligned} \frac{\partial \varrho}{\partial t} + \operatorname{div}(\varrho \mathbf{v}) &= 0 \quad \text{with} \\ \int_{\mathcal{S}^2} \varrho^* \Gamma^* \, d^2 n &= \int_{\mathcal{S}^2} \operatorname{div}_{\mathbf{n}}(\varrho^* \mathbf{u}^*) \, d^2 n = 0, \end{aligned} \quad (41)$$

1722 Notice that the first integral in (41) is a consequence of mass conservation,
 1723 while the second integral follows from Gauss' theorem.

1724 As shown by Faria (2001, 2006a) and Faria and Hutter (2002), the tran-
 1725 sition rate \mathbf{u}^* is governed by its own balance equation, involving couple

1726 stresses and body couples. In the development of the CAFFE model, how-
 1727 ever, an abridged approach has been adopted by postulating a constitutive
 1728 equation for the transition rate

$$\mathbf{u}^* = \mathbf{W}\mathbf{n} - \iota [\dot{\boldsymbol{\epsilon}}\mathbf{n} - (\mathbf{n} \cdot \dot{\boldsymbol{\epsilon}}\mathbf{n}) \mathbf{n}] - \frac{\lambda}{\varrho^*} \text{grad}_{\mathbf{n}}(\varrho^* H^*) \quad (42)$$

1729 where

$$\mathbf{W} = \frac{1}{2} (\text{grad } \mathbf{v} - (\text{grad } \mathbf{v})^T), \dot{\boldsymbol{\epsilon}} = \frac{1}{2} (\text{grad } \mathbf{v} + (\text{grad } \mathbf{v})^T) \quad (43)$$

1730 are the tensors of rotation and strain rate, respectively. The first term on
 1731 the right hand side of (42) represents a rigid-body rotation, while the second
 1732 term describes the process of strain-induced lattice rotation (Dafalias, 2001),
 1733 with $\iota > 0$ denoting the so-called "shape factor" of the theory of rotational
 1734 diffusion (Faria, 2001). According to Placidi et al. (2010), fabric evolution
 1735 simulations of the GRIP and EPICA-DML ice cores suggest that best results
 1736 are obtained for $0.6 > \iota > 0.4$. Finally, the third term on the right hand
 1737 side of (42) models rotation recrystallization as a diffusive process, with
 1738 $\lambda > 0$ being the orientational diffusivity and $H^*(\mathbf{x}, t, \mathbf{n})$ an orientational
 1739 ("chemical") potential, also called "hardness function" by Gödert (2003). In
 1740 principle H^* should be a constitutive function, but, based on microstructural
 1741 analyses of the NorthGRIP ice core (Durand et al., 2008), Placidi et al.
 1742 (2010) suggest that one may simply set $H^* = 1$.

1743 In the original application of the MCD theory to the flow of glaciers and
 1744 ice sheets (Faria, 2006b), the specific recrystallization rate Γ^* is regarded as
 1745 a dissipative variable. However, for simplicity, in the CAFFE model Placidi
 1746 (2004, 2005) has proposed the following relation between Γ^* and the strain

1747 rate

$$\Gamma^* = G(D^* - D), \quad \text{with} \quad (44)$$
$$D^* = 5 \frac{(\dot{\boldsymbol{\varepsilon}} \mathbf{n})^2 - (\mathbf{n} \cdot \dot{\boldsymbol{\varepsilon}} \mathbf{n})^2}{\text{tr}(\dot{\boldsymbol{\varepsilon}}^2)} \quad \text{and} \quad D = \frac{1}{\varrho} \int_{S^2} \varrho^* D^* d^2 n,$$

1748 where $G > 0$ is a material parameter, while $5/2 \geq D^* \geq 0$ and $5/2 \geq D \geq 0$
1749 are called the species and polycrystal "deformability", respectively.

1750 As remarked by Placidi et al. (2010), owing to the difficulties in determin-
1751 ing the values of the material parameters λ and G from experiments, they
1752 are usually determined by fitting numerical simulations of ice core fabrics
1753 and grain stereology. This concludes the description of the fabric evolution.

1754 As for the flow law, in contrast to the full stress–strain rate relation with
1755 tensorial fluidity (viscosity) predicted by the theory of continuous diversity
1756 (Faria, 2006b), the CAFFE model adopts a much simplified generalization
1757 of Glen's flow law:

$$\dot{\boldsymbol{\varepsilon}} = E(D) A(T) \sigma_{eq}^{n-1} \boldsymbol{\sigma}', \quad (45)$$

1758 where $\boldsymbol{\sigma}'$ is the deviatoric part of the Cauchy stress tensor $\boldsymbol{\sigma}$, σ_{eq} is the
1759 effective stress invariant, n is the power law exponent (usually set equal
1760 3), T is the temperature, and $A(T)$ is a temperature-dependent rate factor.
1761 Clearly, (45) implies that all anisotropy effects are contained in the scalar-
1762 valued, deformability-dependent flow enhancement factor $E(D)$, such that
1763 stress and strain rate are collinear and (45) reduces to the classical form of
1764 Glen's flow law when $E(D) \equiv \text{const.}$

1765 A detailed functional form for the enhancement factor $E(D)$ has been
1766 proposed by Seddik et al. (2008) and Placidi et al. (2010), which is con-
1767 tinuously differentiable at $D = 1$ and is compatible with the experimental

1768 results of Azuma (1995) and Miyamoto (1999)

$$E(D) = \begin{cases} (1 - E_{\min}) D^\zeta + E_{\min} & 1 \geq D \geq 0, \\ \frac{4D^2 (E_{\max} - 1) + 25 - 4E_{\max}}{21} & 5/2 \geq D > 1, \end{cases} \quad (46)$$

1769 with

$$\zeta = \frac{8}{21} \left(\frac{E_{\max} - 1}{1 - E_{\min}} \right), \quad E_{\max} \approx 10, \quad E_{\min} \approx 0.1. \quad (47)$$

1770 By introducing the orientation tensors (essentially equivalent to the
1771 dipole and quadrupole moments of ϱ^*/ϱ)

$$\mathbf{a}^{(2)} = \frac{1}{\varrho} \int_{\mathbb{S}^2} \varrho^* \mathbf{n} \otimes \mathbf{n} \, d^2n, \quad \mathbf{a}^{(4)} = \frac{1}{\varrho} \int_{\mathbb{S}^2} \varrho^* \mathbf{n} \otimes \mathbf{n} \otimes \mathbf{n} \otimes \mathbf{n} \, d^2n \quad (48)$$

1772 to reformulate the CAFFE flow law (45) in an explicitly anisotropic form

$$\dot{\boldsymbol{\varepsilon}} = \hat{E}(\boldsymbol{\sigma}') A(T) \sigma_{eq}^{n-1} \boldsymbol{\tau}, \quad (49)$$

1773 In plain words, (49) tells us that the CAFFE model can be applied to all
1774 anisotropies (fabrics) that can satisfactorily be represented by a multipole
1775 expansion up to fourth order. Fortunately, most anisotropies observed in
1776 glaciers and ice sheets.

1777 6.2. GOLF law and Elmer/Ice

1778 In this section, we present the anisotropic ice flow model developed at
1779 LGGE. This model has been used for various applications (Gillet-Chaulet
1780 et al., 2005, 2006; Durand et al., 2007; Martín et al., 2009; Ma et al., 2010).
1781 In this approach, the fabric is described using the second and fourth-order
1782 orientation tensors (48). In this continuum description of the fabric, the
1783 polycrystal represents the local behavior of a representative elementary ice
1784 volume. By assuming that the fourth-order orientation tensor $\mathbf{a}^{(4)}$ is given

1785 as a tensorial function of $\mathbf{a}^{(2)}$ (Gillet-Chaulet et al., 2005), the fabric can
 1786 be described in a very condensed way using $\mathbf{a}^{(2)}$ solely. By definition,
 1787 $\text{tr} \mathbf{a}^{(2)} = 1$, so that only the first two eigenvalues $a_1^{(2)}$ and $a_2^{(2)}$ and three
 1788 Euler angles are needed to completely define the fabric. As a consequence,
 1789 modeled fabrics are orthotropic, *i.e.* the c-axes distribution presents three
 1790 orthogonal symmetry planes. Although orthotropy is a simple form of the
 1791 most general anisotropy, it is thought to be a good compromise between
 1792 physical adequateness and simplicity. The second-order orientation tensor
 1793 allows to describe all the observed fabric patterns: for random c-axes dis-
 1794 tribution the diagonal entries of $\mathbf{a}^{(2)}$ are $a_{11}^{(2)} = a_{22}^{(2)} = a_{33}^{(2)} = 1/3$, for a
 1795 single maximum fabric with its maximum in the third direction, $a_{33}^{(2)} > 1/3$
 1796 and $a_{11}^{(2)} \approx a_{22}^{(2)} < 1/3$, and for a girdle type fabric in the plane (x_1, x_2) ,
 1797 $a_{33}^{(2)} < 1/3$ and $a_{11}^{(2)} \approx a_{22}^{(2)} > 1/3$. When the material symmetry axes are
 1798 those of the general reference frame, as for the three particular previous
 1799 fabrics, the non-diagonal entries of $\mathbf{a}^{(2)}$ are zero.

1800 The behavior of the polycrystal is described by the general orthotropic
 1801 linear flow law (GOLF, Gillet-Chaulet et al., 2005). In its initial form, ice
 1802 was assumed to behave as a linearly viscous orthotropic material. In more
 1803 recent works (Martín et al., 2009; Ma et al., 2010), the GOLF law has been
 1804 extended to a nonlinear form by adding an invariant in the anisotropic linear
 1805 law. The simple choice is either to add the second invariant of the strain
 1806 rate (Martín et al., 2009) or the second invariant of the deviatoric stress
 1807 (Pettit et al., 2007). No theoretical or experimental results are available
 1808 today to discard one of these two solutions, and other solutions based on
 1809 anisotropic invariants of the deviatoric stress and/or the strain rate are
 1810 also possible. In (Ma et al., 2010) approach, the nonlinearity of the law is
 1811 introduced through the second invariant of the deviatoric stress. With this

1812 definition, the anisotropy factors of the polycrystalline law for a given stress
 1813 are identical in the linear and nonlinear cases. In other words, for a given
 1814 fabric and a given state of stress, the corresponding strain rate relative to
 1815 the isotropic response is the same for the linear and nonlinear cases. Using
 1816 the strain-rate invariant in the same way as Martín et al. (2009) did, leads
 1817 to different anisotropy factors (as defined here) in the linear and nonlinear
 1818 cases. Therefore, the proposed expression of the nonlinear GOLF law is as
 1819 follows:

$$\sum_{r=1}^3 [\eta_r \text{tr}(\mathbf{M}_r \cdot \dot{\boldsymbol{\epsilon}}) \mathbf{M}'_r + \eta_{r+3} (\dot{\boldsymbol{\epsilon}} \cdot \mathbf{M}_r + \mathbf{M}_r \cdot \dot{\boldsymbol{\epsilon}})'] = 2A\sigma_{eq}^{n-1} \boldsymbol{\sigma}', \quad (50)$$

1820 where A is the temperature-dependent Glen's law parameter for isotropic ice.
 1821 The six dimensionless anisotropy viscosities $\eta_r(\mathbf{a}^{(2)})$ and $\eta_{r+3}(\mathbf{a}^{(2)})$ ($r = 1,$
 1822 $2, 3$) are functions of eigenvalues of the second-order orientation tensor $\mathbf{a}^{(2)}$,
 1823 which represent a measure of the anisotropy strength. The three structure
 1824 tensors \mathbf{M}_r are given by the dyadic products of the three eigenvectors of $\mathbf{a}^{(2)}$,
 1825 which then represent the material symmetry axes. In the method proposed
 1826 by Gillet-Chaulet et al. (2005), the six dimensionless viscosities $\eta_r(\mathbf{a}^{(2)})$ are
 1827 tabulated as a function of the fabric strength (*i.e.*, the $a_i^{(2)}$) using a micro-
 1828 macro model. When ice is isotropic, $\eta_r = 0$ and $\eta_{r+3} = 1$ ($r = 1, 2, 3$), and
 1829 Eq. (50) reduces to the isotropic Glen's flow law.

1830 Following Gillet-Chaulet et al. (2005), the six dimensionless viscosities
 1831 $\eta_r(\mathbf{a}^{(2)})$ are tabulated using the visco-plastic self-consistent model (VPSC,
 1832 Castelnau et al., 1996a, 1998), see Section 3. The two crystal parameters
 1833 in the VPSC model used to tabulate the GOLF law were chosen so that
 1834 the experimentally observed polycrystal anisotropy is reproduced. Gillet-
 1835 Chaulet et al. (2005) use the shear-strain rates ratio for a polycrystal with
 1836 a single maximum fabric and an isotropic polycrystal both experiencing

1837 the same shear stress. This anisotropy factor in shear is hereafter noted
1838 k_s and, according to the experimental results of Pimienta et al. (1987), its
1839 value is approximately $k_s = 10$. In other words, the VPSC parameters
1840 are chosen so that the response under simple shear of a polycrystal with a
1841 single maximum fabric is k_s times easier to deform than the corresponding
1842 isotropic polycrystal. The experimental results of Pimienta et al. (1987) also
1843 indicate that an isotropic polycrystal is much easier to deform than a single
1844 maximum fabric polycrystal experiencing the same uniaxial compressional
1845 stress. These experiments allow to define a second anisotropy factor for
1846 uniaxial compressional stress, which is noted k_c . A value $k_c = 0.4$ is in
1847 accordance with the experimental results of Pimienta et al. (1987). As
1848 discussed before, the anisotropy factors k_s and k_c are independent of Glen's
1849 flow law exponent n with the adopted nonlinear formulation.

1850 Assuming that recrystallization processes do not occur and that the ice
1851 fabric is induced solely by deformation, the evolution of the second-order
1852 orientation tensor $\mathbf{a}^{(2)}$ can be written as

$$\frac{D\mathbf{a}^{(2)}}{Dt} = \mathbf{W} \cdot \mathbf{a}^{(2)} - \mathbf{a}^{(2)} \cdot \mathbf{W} - (\mathbf{C} \cdot \mathbf{a}^{(2)} + \mathbf{a}^{(2)} \cdot \mathbf{C}) + 2\mathbf{a}^{(4)} : \mathbf{C}, \quad (51)$$

1853 where \mathbf{W} is the spin tensor defined as the antisymmetric part of the velocity
1854 gradient. The tensor \mathbf{C} is defined as

$$\mathbf{C} = (1 - \alpha)\dot{\boldsymbol{\varepsilon}} + \alpha k_s A \sigma_{eq}^{n-1} \boldsymbol{\sigma}'. \quad (52)$$

1855 The *interaction parameter* α controls the relative weighting of the strain
1856 rate $\dot{\boldsymbol{\varepsilon}}$ and the deviatoric stress $\boldsymbol{\sigma}'$ in the fabric evolution Eq. (51). When
1857 $\alpha = 0$, the fabric evolution is solely controlled by the state of strain rate,
1858 whereas in the case where $\alpha = 1$ the fabric evolves under the influence of
1859 the deviatoric stress solely. In between, as for the VPSC, both the strain

1860 rate and deviatoric stress contribute to the fabric evolution. In what fol-
1861 lows, the interaction parameter is $\alpha = 0.06$ in accordance with the crystal
1862 anisotropy and the VPSC model used to derive the polycrystal behaviour
1863 (Gillet-Chaulet et al., 2005). In Eq. (51), the fourth-order orientation ten-
1864 sor is evaluated assuming a closure approximation giving $\mathbf{a}^{(4)}$ as a tensorial
1865 function of $\mathbf{a}^{(2)}$ (Gillet-Chaulet et al., 2005).

1866 The anisotropic polycrystalline law described above and the associated
1867 fabric evolution equations have been implemented in the Finite Element
1868 code Elmer/Ice, the glaciological part of the open source Finite Element
1869 software Elmer developed by CSC (<http://www.elmerfem.org/>). Ice flow
1870 (velocity and isotropic pressure) are obtained solving the anisotropic Stokes
1871 equations and coupled with the fabric evolution equation (51) and the upper
1872 free surface equation in the case of transient simulations. In Gillet-Chaulet
1873 et al. (2006), the model was applied to synthetic geometries in order to
1874 show the influence of coupling the Stokes and fabric evolution equations on
1875 the flow of ice over a bumpy bedrock. In Durand et al. (2007), the model
1876 was used to explain the fabric evolution in the Dome C ice core, in the
1877 framework of the EPICA project. The authors showed that to explain the
1878 fabric evolution at Dome C, shear stress must be invoked. The model was
1879 also applied to evaluate the value of the ad-hoc enhancement factor that
1880 should be incorporated in large-scale isotropic ice-sheet flow model in Ma
1881 et al. (2010). In Martín et al. (2009), the anisotropic ice flow model was
1882 applied to explain observed shapes of isochrones below ridges or domes.

1883 **7. Synthesis and perspectives**

1884 Applications of ice mechanical behavior modeling extend from below the
1885 single-crystal scale to the ice sheet scale. Upwards, this scale range far ex-
1886 ceeds that of engineering material sciences but is similar to the geological
1887 one. Within this scale range, many physical processes come into play, some
1888 of which are not yet very well described. Furthermore, there exist strong in-
1889 teractions between these processes that create bridges between the different
1890 levels of complexity. Modeling of ice has strongly benefited from advances
1891 in materials science. In return, as shown by the results presented in this pa-
1892 per, the contribution of the ice community to the theoretical understanding
1893 and modeling of the mechanical behavior of anisotropic materials is signif-
1894 icant. With the large viscoplastic anisotropy of the ice crystal, ice is now
1895 considered a model material. The advances presented here may equally well
1896 be applied to, for example, mantle flow, where the anisotropy due to fabric
1897 (CPO) development in olivine is thought to play a significant role (Tommasi
1898 et al., 2009; Long and Becker, 2010).

1899 The presented modeling methods are basically of two types; some that
1900 aim to precisely reproduce the physical mechanisms as observed experimen-
1901 tally, and some with a more phenomenological approach. Going through
1902 scales, it clearly appears that individual dislocation interactions cannot be
1903 taken into account at the scale of the polycrystal imbedded in a glacier envi-
1904 ronment. Nevertheless, modeling at the scale of dislocation interactions pro-
1905 vides a better estimate of the interactions between slip systems at the single
1906 crystal scale, which, in turn, is essential to reproduce an accurate mechanical
1907 response of the polycrystal with mean-field and full-field approaches. Fur-
1908 thermore, full-field approaches are necessary to validate the approximations

1909 made using mean-field models, as they provide the "exact" (in a numerical
1910 sense) response of the specimen with a real microstructure, integrating the
1911 inter- and intra-granular interactions. Finally, large-scale flow models are
1912 now getting to a sufficient level of complexity to be able to take into account
1913 and represent the anisotropy associated with the fabrics induced by the flow
1914 conditions. To do so, they integrate mean-field approaches that correctly
1915 reproduce the viscoplastic anisotropy and a non-linear mechanical behavior.

1916 A summary of the main domains of application, advantages, and limita-
1917 tions of the main modeling tools presented in the paper is given on tables
1918 2, 3 and 4

1919 Much progress has recently been made in the modeling of dynamic re-
1920 crystallization processes and their interactions with flow anisotropy. Never-
1921 theless, due to the complexity of the physical processes involved, to jump
1922 the gap between scales is a strong challenge. The field dislocation mechanics
1923 approach appears very promising to associate the internal stress field and
1924 dislocation arrangements to the nucleation and grain boundary migration
1925 mechanisms. However, field dislocation mechanics cannot yet be applied to
1926 scales larger than the polycrystal. Full-field models, including the FFT-Elle
1927 coupling, have the same scale limitation, but may play an important role
1928 in parameterizing small-scale processes (dislocation glide, grain boundary
1929 migration, etc.) for mean-field models. They are also important tools to
1930 test models of mechanical and microstructural evolution.

1931 Compared to other minerals, ice shows remarkably strong transient be-
1932 havior (Duval et al., 1983; Castelnau et al., 2008b). Continuum flow models,
1933 such as Glen law (Glen, 1955) have so far not been able to incorporate the
1934 resulting mechanical complexity of polycrystalline ice deformation. Only
1935 recently have mechanical models reached a level of sophistication to address

1936 transient behavior. This development is promising and probably highly rel-
1937 evant in cases where ice flow changes at rates for where both elastic and
1938 viscoplastic behavior may interact. In particular, this concerns the very
1939 topical subject of ice shelves, ice streams or extra-terrestrial ice submitted
1940 to tide forcing. Which model will be able to correctly take into account
1941 these transient, and event cyclic behavior, and at which scale?

1942 A next step will likely be the multi-scale coupling of models of increas-
1943 ing complexity. We can expect dislocation dynamics and field dislocation
1944 mechanics to provide the local criteria for slip system interactions, nucle-
1945 ation, grain boundary migration as local input to full-field approaches that
1946 will be further used in interaction with mean-field approaches to calibrate
1947 dynamic recrystallization variables influencing the mechanical response and
1948 fabric development.

1949 An interesting example of such model interweaving is given by the large-
1950 scale flow modeling presented in this paper. Nevertheless, a strong effort
1951 is still required concerning the flow law of ice and its dependency on fab-
1952 rics (CPO) and strain. Recent velocity measurements in Greenland (Gillet-
1953 Chaulet et al., 2011) questioned the relevance of a stress exponent equal
1954 to three as classically considered for large scale flow modeling (for instance
1955 Paterson (1994); Hooke (2005); Greve and Blatter (2009), ...). Owing to
1956 the variety of processes that accommodate strain along an ice core path,
1957 one could also expect several regimes to occur with depth, as suggested by
1958 some authors (see for instance Lipenkov et al. (1989); Faria et al. (2009);
1959 Pettit et al. (2011)). Such modeling - observation comparisons mainly raise
1960 the complexity of the physical processes involved that can probably not be
1961 summarized in a single universal law.

1962 **8. Acknowledgement**

1963 Financial support by the French "Agence Nationale de la Recherche"
1964 is acknowledged (project ELVIS, #ANR-08-BLAN-0138). Together with
1965 support from institutes INSIS and INSU of CNRS, and UJF - Grenoble
1966 1, France. PDB and JR gratefully acknowledge funding by the German
1967 Research Foundation (DFG, project BO-1776/7). The authors gratefully
1968 acknowledge the ESF Research Networking Programme Micro-Dynamics of
1969 Ice (MicroDice).

1970

1971 **References**

1972 Acharya, A.. A model of crystal plasticity based on the theory of contin-
1973 uously distributed dislocations. *Journal of the Mechanics and Physics of*
1974 *Solids* 2001;49(4):761 – 784.

1975 Acharya, A., Roy, A.. Size effects and idealized dislocation microstructure
1976 at small scales: Predictions of a phenomenological model of mesoscopic
1977 field dislocation mechanics: Part I. *Journal of the Mechanics and Physics*
1978 *of Solids* 2006;54(8):1687 – 1710.

1979 Alley, R.B.. *Fabrics in polar ice sheets - Development and prediction.*
1980 *Science* 1988;240:493–495.

1981 Alley, R.B.. Flow-law hypotheses for ice-sheet modeling. *J Glaciol*
1982 1992;38(129):245–255.

1983 Alley, R.B., Perepezko, J.H., Bentley, C.R.. Grain growth in polar ice: I.
1984 theory. *J Glaciol* 1986;32(112):415–424.

- 1985 Arsenlis, A., Parks, D.M.. Crystallographic aspects of geometrically-
1986 necessary and statistically-stored dislocation density. *Acta Materialia*
1987 1999;47:1597–1611.
- 1988 Ashby, M.F., Duval, P.. the creep of polycrystalline ice. *Cold Reg Sc Tech*
1989 1985;11:285–300.
- 1990 Azuma, N.. A flow law for anisotropic ice and its application to ice sheets.
1991 *Earth and Planetary Science Letters* 1994;128(3â“4):601 – 614.
- 1992 Azuma, N.. A flow law for anisotropic polycrystalline ice under uniaxial
1993 compressive deformation. *Cold Reg Sci Technol* 1995;23:137–147.
- 1994 Azuma, N., Higashi, A.. Formation processes of ice fabric pattern in ice
1995 sheets. *Ann Glaciol* 1985;6:130–134.
- 1996 Bargmann, S., Seddik, H., Greve, R.. Computational modeling of flow-
1997 induced anisotropy of polar ice for the EDML deep drilling site, Antarc-
1998 tica: the effect of rotation recrystallization and grain boundary migration.
1999 *Int J Numer Anal Meth Geomech* 2011;;DOI: 10.1002/nag.1034.
- 2000 Barnes, P., Tabor, D., Walker, J.. The friction and creep of polycrystalline
2001 ice. *Proceeding of the Royal Society of London Series A, Mathematical*
2002 *and Physical Sciences* 1971;324(1557):127–155.
- 2003 Barr, T., Houseman, G.. Deformation fields around a fault embed-
2004 ded in a non-linear ductile medium. *Geophysical Journal International*
2005 1996;125:473–490.
- 2006 Battaile, C., Counts, W., Wellman, G., Buchheit, T., Holm, E.. Simulat-
2007 ing grain growth in a deformed polycrystal by coupled finite-element and

- 2008 microstructure evolution modeling. *Metallurgical and Materials Transactions A* 2007;38:2513–2522. 10.1007/s11661-007-9267-6.
2009
- 2010 Becker, J.K., Bons, P.D., Jessell, M.W.. A new front-tracking method to
2011 model anisotropic grain and phase boundary motion in rocks. *Computers*
2012 & *Geosciences* 2008;34:201–212.
- 2013 Bobeth, M., Diener, G.. Static and thermoelastic field fluctuations in
2014 multiphase composites. *JMech Phys Solids* 1987;35:137–149.
- 2015 Boehler, J.P., Aoufi, L.E., Raclin, J.. On experimental testing methods
2016 for anisotropic materials. *Res Mech* 1987;21:73–95.
- 2017 Bons, P.D., Barr, T.D., ten Brink, C.E.. The development of delta-clasts
2018 in non-linear viscous materials: a numerical approach. *Tectonophysics*
2019 1997;270:29–41.
- 2020 Bons, P.D., Jessell, M.W., Evans, L., Barr, T.D., Stüwe, K.. Modelling
2021 of anisotropic grain growth in minerals. *Geological Society of America*
2022 *Memoir* 2001;193:39–49.
- 2023 Bons, P.D., Koehn, D., Jessell, M.W.. Lecture notes in earth sciences.
2024 In: Bons, P., Koehn, D., Jessell, M., editors. *Microdynamic Simulation*.
2025 Springer, Berlin; number 106; 2008. 405pp.
- 2026 Bornert, M., Masson, R., Ponte Castañeda, P., Zaoui, A.. Second-
2027 order estimates for the effective behaviour of viscoplastic polycrystalline
2028 materials. *J Mech Phys Solids* 2001;49:2737–2764.
- 2029 Bornert, M., Ponte Castañeda, P.. Second-order estimates of
2030 the self-consistent type for viscoplastic polycrystals. *ProcRSocLond*
2031 1998;A454:3035–3045.

- 2032 Bouchez, J.L., Duval, P.. The fabric of polycrystalline ice deformed in sim-
2033 ple shear : experiments in torsion, natural deformation and geometrical
2034 interpretation. *Textures and microstructures* 1982;5:171–190.
- 2035 Brenner, R., Béchade, J.L., Castelnau, O., Bacroix, B.. Thermal creep of
2036 Zr-Nb1%-O alloys: experimental analysis and micromechanical modelling.
2037 *J Nucl Mater* 2002a;305:175–186.
- 2038 Brenner, R., Castelnau, O., Badea, L.. Mechanical field fluctuations in
2039 polycrystals estimated by homogenization techniques. *ProcR SocLond*
2040 2004;A460(2052):3589–3612.
- 2041 Brenner, R., Lebensohn, R.A., Castelnau, O.. Elastic anisotropy and yield
2042 surface estimates. *Int J Solids Struct* 2009;46:3018–3026.
- 2043 Brenner, R., Masson, R., Castelnau, O., Zaoui, A.. A “quasi-elastic”
2044 affine formulation for the homogenized behaviour of nonlinear viscoelastic
2045 polycrystals and composites. *Eur J Mech A/Solids* 2002b;21:943–960.
- 2046 Brinckmann, S., Siegmund, T., Huang, Y.. A dislocation density based
2047 strain gradient model. *International Journal of Plasticity* 2006;22:1784–
2048 1797.
- 2049 Budd, W., Jacka, T.. A review of ice rheology for ice sheet modelling.
2050 *Cold Reg Sci Technol* 1989;16:107–144.
- 2051 Buiron, D., Chappellaz, J., Stenni, B., Frezzoti, M., Baumgartner, M.,
2052 Capron, E., Landais, A., Lemieux-Dudon, B., Masson-Delmotte, V.,
2053 Montagnat, M., Parrenin, F., Schilt, A.. TALDICE-1 age scale of the
2054 Talos Dome deep ice core, East Antarctica. *Climate of the Past* 2011;7:1–
2055 16.

- 2056 Bunge, H.J.. *Texture Analysis in Materials Science*. 3rd ed. Goettingen:
2057 Cuvillier, 1993.
- 2058 Castelnau, O., Blackman, D.K., Becker, T.W.. Numerical simulations of
2059 texture development and associated rheological anisotropy in regions of
2060 complex mantle flow. *Geophys Res Let* 2009;36(L12304).
- 2061 Castelnau, O., Blackman, D.K., Lebensohn, R.A., Ponte-Castañeda, P..
2062 Micromechanical modeling of the viscoplastic behavior of olivine. *Journal*
2063 *of Geophysical Research* 2008a;113:B09202.
- 2064 Castelnau, O., Brenner, R., Lebensohn, R.A.. The effect of strain het-
2065 erogeneity on the work-hardening of polycrystals predicted by mean-field
2066 approaches. *Acta Materialia* 2006;54:2745–2756.
- 2067 Castelnau, O., Canova, G.R., Lebensohn, R.A., Duval, P.. Modelling vis-
2068 coplastic behavior of anisotropic polycrystalline ice with a self-consistent
2069 approach. *Acta Materialia* 1997;45(11):4823 – 4834.
- 2070 Castelnau, O., Cordier, P., Lebensohn, R.A., Merkel, S., Raterron, P..
2071 Microstructures and rheology of the earth’s upper mantle inferred from a
2072 multiscale approach. *Comptes Rendus Physique* 2010a;11(3-4):304 – 315.
2073 *Computational metallurgy and scale transitions*.
- 2074 Castelnau, O., Duval, P.. Simulations of anisotropy and fabric development
2075 in polar ices. *Ann Glaciol* 1994;20:277–282.
- 2076 Castelnau, O., Duval, P., Lebensohn, R.A., Canova, G.. Viscoplas-
2077 tic modeling of texture development in polycrystalline ice with a self-
2078 consistent approach : Comparison with bound estimates. *J Geophys Res*
2079 1996a;101(6):13,851–13,868.

2080 Castelnau, O., Duval, P., Montagnat, M., Brenner, R.. Elastoviscoplas-
2081 tic micromechanical modeling of the transient creep of ice. *Journal of*
2082 *Geophysical Research Solid Earth* 2008b;113(B11203).

2083 Castelnau, O., Lebensohn, R.A., Ponte Castañeda, P., Blackman, D..
2084 *Earth Mantle Rheology Inferred from Homogenization Theories*; ISTE. p.
2085 55–70.

2086 Castelnau, O., Shoji, H., Mangeney, A., Milsch, H., Duval, P., Miyamoto,
2087 A., Kawada, K., Watanabe, O.. Anisotropic behavior of GRIP ices
2088 and flow in Central Greenland. *Earth and Planetary Science Letters*
2089 1998;154(1-4):307 – 322.

2090 Castelnau, O., Thorsteinsson, T., Kipfstuhl, J., Duval, P., Canova, G.R..
2091 *Modelling fabric development along the GRIP ice core, central Greenland.*
2092 *Ann Glaciol* 1996b;23:194–201.

2093 Chaboche, J.L.. A review of some plasticity and viscoplasticity constitutive
2094 theories. *International Journal of Plasticity* 2008;24:1642–1693.

2095 de la Chapelle, S., Castelnau, O., Lipenkov, V., Duval, P.. Dy-
2096 namic recrystallization and texture development in ice as revealed by the
2097 study of deep ice cores in Antarctica and Greenland. *J Geophys Res*
2098 1998;103(B3):5091–5105.

2099 Chevy, J., Fressengeas, C., Lebyodkin, M., Taupin, V., Bastie, P.,
2100 Duval, P.. Characterizing short-range vs. long-range spatial correlations
2101 in dislocation distributions. *Acta Materialia* 2010;58(5):1837 – 1849.

2102 Chevy, J., Louchet, F., Duval, P., Fivel, M.. Creep behaviour of ice

- 2103 single crystals loaded in torsion explained by dislocation cross-slip. *Phil*
2104 *Mag Let* 2012;92(6):262–269. In press.
- 2105 Chevy, J., Montagnat, M., Duval, P., Fivel, M., Weiss, J.. Dislocation
2106 patterning and deformation processes in ice single crystal deformed by
2107 torsion. *Proc 11th Int Conf Phys & Chem of Ice 2007*;:142–146.
- 2108 Cochard, J., Yonenaga, I., Gouttebroze, S., MHamdi, M., Zhang, Z.L..
2109 Constitutive modeling of intrinsic silicon monocrystals in easy glide. *Jour-*
2110 *nal of Applied Physics* 2010;107(3):033512–033512–9.
- 2111 Dafalias, Y.F.. Orientation distribution function in non-affine rotations. *J*
2112 *Mech Phys Solids* 2001;49:2493–2516.
- 2113 Dahl-Jensen, D., Gundestrup, N.S.. Constitutive properties of ice at Dye
2114 3, Greenland. In: *The physical basis of ice sheet modelling*. Vancouver
2115 *Symposium; IAHS; volume 170; 1987. p. 31–43.*
- 2116 Dansgaard, W., Johnsen, S.J., Clausen, H.B., Dahl-Jensen, D., Gun-
2117 destrup, N.S., Hammer, C.U., Hvidberg, C.S., Steffensen, J.P.,
2118 Sveinbjörnsdóttir, A.E., Jouzel, J., Bond, G.. Evidence for general insta-
2119 bility of past climate from a 250 kyr ice-core record. *Nature* 1993;364:218–
2120 220.
- 2121 De Botton, G., Ponte Castañeda, P.. Variational estimates for the creep
2122 behaviour of polycrystals. *Proc R Soc Lond* 1995;A 448:121–142.
- 2123 Durand, G., Gillet-Chaulet, F., Svensson, A., Gagliardini, O., Kipfstuhl,
2124 S., Meyssonier, J., Parrenin, F., Duval, P., Dahl-Jensen, D., Azuma,
2125 N.. Change of the ice rheology with climatic transitions. Implication on

- 2126 ice flow modelling and dating of the EPICA Dome C core. *Climates of*
2127 *the Past* 2007;3:155–167.
- 2128 Durand, G., Graner, F., Weiss, J.. Deformation of grain boundaries in
2129 polar ice. *EPL (Europhysics Letters)* 2004;67(6):1038.
- 2130 Durand, G., Persson, A., Samyn, D., Svensson, A.. Relation between
2131 neighbouring grains in the upper part of the NorthGRIP ice core - Implica-
2132 tions for rotation recrystallization. *Earth and Planet Sc Let* 2008;265:666–
2133 671.
- 2134 Duval, P.. Lois du fluage transitoire ou permanent de la glace polycristalline
2135 pour divers états de contraintes. *Ann Geophys* 1976;32(4):335–350.
- 2136 Duval, P.. Anelastic behaviour of polycrystalline ice. *J Glaciol*
2137 1978;21(85):621–628.
- 2138 Duval, P.. Creep and fabrics of polycrystalline ice under shear and com-
2139 pression. *J Glaciol* 1981;27(95):129–140.
- 2140 Duval, P., Arnaud, L., Brissaud, O., Montagnat, M., de La Chapelle, S..
2141 Deformation and recrystallization processes of ice from polar ice sheets.
2142 *Ann Glaciol* 2000;30:83–87.
- 2143 Duval, P., Ashby, M., Anderman, I.. Rate controlling processes in the
2144 creep of polycrystalline ice. *J Phys Chem* 1983;87(21):4066–4074.
- 2145 Duval, P., Castelnau, O.. Dynamic recrystallization of ice in polar ice
2146 sheets. *J Physique IV (suppl J Phys III)*, C3 1995;5:197–205.
- 2147 Duval, P., Le Gac, H.. Does the permanent creep-rate of polycrystalline
2148 ice increase with crystal size? *Journal of Glaciology* 1980;25:151–157.

2149 Duval, P., Montagnat, M.. Comment on "Superplastic deformation of
2150 ice: experimental observations" by D.L. Goldsby and D.L. Kohlstedt. J
2151 Geophys Res 2002;107:(2082)1–4.

2152 Duval, P., Montagnat, M., Grennerat, F., Weiss, J., Meyssonier, J.,
2153 Philip, A.. Creep and plasticity of glacier ice: a material science perspec-
2154 tive. Journal of Glaciology 2010;56(200):1059–1068.

2155 Eshelby, J.. The determination of the elastic field of an ellipsoidal inclusion,
2156 and related problems. Proc R Soc London Ser A 1957;241:376–396.

2157 Faria, S.H.. Mixtures with continuous diversity: general theory and appli-
2158 cation to polymer solutions. Continuum Mechanics and Thermodynamics
2159 2001;13(2):91–120.

2160 Faria, S.H.. Creep and recrystallization of large polycrystalline masses. I.
2161 General continuum theory. Royal Society of London Proceedings Series
2162 A 2006a;462(2069):1493–1514.

2163 Faria, S.H.. Creep and recrystallization of large polycrystalline masses. III:
2164 Continuum theory of ice sheets. Royal Society of London Proceedings
2165 Series A 2006b;462:2797–2816.

2166 Faria, S.H., Freitag, J., Kipfstuhl, S.. Polar ice structure and the integrity
2167 of ice-core paleoclimate records. Quat Sci Rev 2010;29(1):338–351.

2168 Faria, S.H., Hutter, K.. A systematic approach to the thermodynamics of
2169 single and mixed flowing media with microstructure. Part I: balance equa-
2170 tions and jump conditions. Continuum Mech Thermodyn 2002;14(5):459–
2171 481.

- 2172 Faria, S.H., Kipfstuhl, S., Azuma, N., Freitag, J., Hamann, I., Murshed,
2173 M.M., Kuhs, W.F.. The multiscale structure of Antarctica. Part I: inland
2174 ice. *Low Temp Sci* 2009;68:39–59.
- 2175 Faria, S.H., Kremer, G.M., Hutter, K.. On the inclusion of recrystal-
2176 lization processes in the modeling of induced anisotropy in ice sheets: a
2177 thermodynamicist’s point of view. *Ann Glaciol* 2003;37(1):29–34.
- 2178 Faria, S.H., Kremer, G.M., Hutter, K.. Creep and recrystallization of
2179 large polycrystalline masses. II. Constitutive theory for crystalline media
2180 with transversely isotropic grains. *Royal Society of London Proceedings*
2181 *Series A* 2006;462(2070):1699–1720.
- 2182 Faria, S.H., Ktitarev, D., Hutter, K.. Modelling evolution of anisotropy
2183 in fabric and texture of polar ice. *Ann Glaciol* 2002;35:545–551.
- 2184 Faria, S.H., Weikusat, I., Azuma, N.. The microstructure of polar ice. *J*
2185 *Struct Geol* this issue;
- 2186 Fressengeas, C.. *La mécanique des champs de dislocations*. Hermès Sciences,
2187 2010.
- 2188 Gagliardini, O., Gillet-Chaulet, F., Montagnat, M.. A review of anisotropic
2189 polar ice models: from crystal to ice-sheet flow models. In: Hondoh, T.,
2190 editor. *Physics of Ice Core Records II*. Supplement Issue of *Low Temper-*
2191 *ature Science*, Hokkaido University; volume 68; 2009. p. 149–166.
- 2192 Gammon, P., Kiefte, H., Clouter, M.. Elastic constants of ice samples by
2193 Brillouin spectroscopy. *J Phys Chem* 1983;87:4025–4029.
- 2194 Gao, H., Huang, Y., Nix, W.D., Hutchinson, J.W.. Mechanism-based

- 2195 strain gradient plasticity – I. theory. *Journal of the Mechanics and Physics*
2196 *of Solids* 1999;47(6):1239 – 1263.
- 2197 Gillet, F., Durand, G.. Ice-sheet advance in Antarctica. *Nature*
2198 2010;467:794–795.
- 2199 Gillet-Chaulet, F., Gagliardini, O., Meyssonier, J., Montagnat, M.,
2200 Castelnau, O.. A user-friendly anisotropic flow law for ice-sheet mod-
2201 elling. *J Glaciol* 2005;41(172):3 – 14.
- 2202 Gillet-Chaulet, F., Gagliardini, O., Meyssonier, J., Zwinger, T., Ruoko-
2203 lainen, J.. Flow-induced anisotropy in polar ice and related ice-sheet flow
2204 modelling. *J Non-Newtonian Fluid Mech* 2006;134:33–43.
- 2205 Gillet-Chaulet, F., Gagliardini, O., Seddik, H., Nodet, M., Durand, G.,
2206 Ritz, C., Zwinger, T., Greve, R., Vaughan, D.G.. Greenland ice sheet
2207 contribution to sea-level rise from a new-generation ice-sheet model. *The*
2208 *Cryosphere* 2012;6(6):1561–1576.
- 2209 Gillet-Chaulet, F., Hindmarsh, R.C.A., Corr, H.F.J., King, E.C., Jenk-
2210 ins, A.. In-situ quantification of ice rheology and direct measurement of
2211 the Raymond effect at Summit, Greenland using a phase-sensitive radar.
2212 *Geophys Res Lett* 2011;38(24).
- 2213 Gilormini, P.. A critical evaluation for various non-linear extensions of the
2214 self-consistent model. In: Pineau, A., Zaoui, A., editors. *IUTAM Symp.*
2215 *on Micromechanics of Plasticity and Damage of Multiphase Materials.*
2216 *Klower Acad. Publ., Sèvres, France; 1995. p. 67–74.*
- 2217 Glen, J.. The creep of polycrystalline ice. *Proc Roy Soc London*
2218 1955;A228:519–538.

- 2219 Gödert, G.. A mesoscopic approach for modelling texture evolution of polar
2220 ice including recrystallization phenomena. *Ann Glaciol* 2003;37:23–28.
- 2221 Goldsby, D.L., Kohlstedt, D.L.. Grain boundary sliding in fine-grained ice
2222 I. *Scripta Mater* 1997;37(9):1399–1406.
- 2223 Gow, A.. On the rate of growth of grains and crystals in south polar firn.
2224 *J Glaciol* 1969;8:241–252.
- 2225 Grennerat, F., Montagnat, M., Castelnau, O., Vacher, P., Moulinec, H.,
2226 Suquet, P., Duval, P.. Experimental characterization of the intragran-
2227 ular strain field in columnar ice during transient creep. *Acta Materialia*
2228 2012;60(8):3655–3666.
- 2229 Greve, R., Blatter, H.. *Dynamics of Ice Sheets and Glaciers*. Berlin:
2230 Springer, 2009.
- 2231 Griera, A., Bons, P.D., Jessell, M.W., Lebensohn, R.A., Evans, L.,
2232 Gomez-Rivas, E.. Strain localization and porphyroclast rotation. *Geology*
2233 2011;39:275–278.
- 2234 Griera, A., Llorens, M.G., Gomez-Rivas, E., Bons, P.D., Jessell, M.W.,
2235 Evans, L.A., Lebensohn, R.A.. Numerical modelling of porphyroclast and
2236 porphyroblast rotation in anisotropic rocks. *Tectonophysics* 2012;587:4–
2237 29. In press.
- 2238 Guillopé, M., Poirier, J.. Dynamic recrystallization during creep of single-
2239 crystalline halite: an experimental study. *J Geophys Res* 1979;84:5557–
2240 5567.
- 2241 Gundestrup, N., Hansen, B.L.. Bore-hole survey at Dye 3, South Green-
2242 land. *Journal of Glaciology* 1984;30:282–288.

- 2243 Hamman, I., Weikusat, C., Azuma, N., Kipfstuhl, S.. Evolution of crystal
2244 microstructure during creep experiments. *J Glaciol* 2007;53(182):479–489.
- 2245 Hershey, A.V.. The elasticity of an isotropic aggregate of anisotropic cubic
2246 crystals. *J Appl Mech* 1954;21:236–240.
- 2247 Higashi, A., Koinuma, S., Mae, S.. Bending creep of ice single crystals.
2248 *Jpn J Appl Phys* 1965;4:575–582.
- 2249 Hooke, R.L.. *Principles of Glacier Mechanics*. 2nd ed. Cambridge: Cam-
2250 bridge University Press, 2005.
- 2251 Humphreys, F.J., Hatherly, M.. *Recrystallization and related annealing*
2252 *phenomena*. Second ed. Pergamon, Oxford, 2004.
- 2253 Hutchinson, J.. Creep and plasticity of hexagonal polycrystals as related
2254 to single crystal slip. *Metall Trans* 1977;8A(9):1465–1469.
- 2255 Idiart, M.I., Moulinec, H., Ponte Castañeda, P., Suquet, P.. Macro-
2256 scopic behavior and field fluctuations in viscoplastic composites: Second-
2257 order estimates versus full-field simulations. *Journal of the Mechanics and*
2258 *Physics of Solids* 2006;54(5):1029 – 1063.
- 2259 Jacka, T.. Investigations of discrepancies between laboratory studies on
2260 the flow of ice: density, sample shape and size and grain size. *Annals of*
2261 *Glaciology* 1994;19:146–154.
- 2262 Jacka, T.H., Li, J.. The steady-state crystal size of deforming ice. *Ann*
2263 *Glaciol* 1994;20:13–18.
- 2264 Jacka, T.H., Maccagnan, M.. Ice crystallographic and strain rate

- 2265 changes with strain in compression and extension. *Cold Reg Sci Tech-*
2266 *nol* 1984;8:269–286.
- 2267 Jessell, M.W.. Simulation of fabric development in recrystallizing ag-
2268 gregates. 1. Description of the models. *Journal of Structural Geology*
2269 1988a;10:771–778.
- 2270 Jessell, M.W.. Simulation of fabric development in recrystallizing ag-
2271 gregates. 2. Example model runs. *Journal of Structural Geology*
2272 1988b;10:779–793.
- 2273 Jessell, M.W., Bons, P. D., Evans, L., Barr, T., Stüwe, K.. Elle: the
2274 numerical simulation of metamorphic and deformation microstructures.
2275 *Computers & Geosciences* 2001;27:17–30.
- 2276 Jessell, M.W., Bons, P.D.. The numerical simulation of microstructure.
2277 *Geol Soc, London, Spec Publ* 2002;200:137–147.
- 2278 Jessell, M.W., Bons, P.D., Griera, A., Evans, L.A., Wilson, C.J.L.. A
2279 tale of two viscosities. *Journal of Structural Geology* 2009;31:719–736.
- 2280 Jessell, M.W., Siebert, E., Bons, P.D., Evans, L., Piazzolo, S.. A new
2281 type of numerical experiment on the spatial and temporal patterns of
2282 localization of deformation in a material with a coupling of grain size and
2283 rheology. *Earth and Planetary Science Letters* 2005;239:309–326.
- 2284 Jones, S., Glen, J.. The mechanical properties of single crystals of pure
2285 ice. *J Glaciol* 1969;8(54):463–473.
- 2286 Kanit, T., Forest, S., Galliet, I., Mounoury, V., Jeulin, D.. Determination
2287 of the size of the representative volume element for random composites:
2288 statistical and numerical approach. *Int J Solids Struct* 2003;40:3647–3679.

- 2289 Ketcham, W.M., Hobbs, P.V.. An experimental determination of the
2290 surface energies of ice. *Philosophical Magazine* 1969;19:1161–1173.
- 2291 Kipfstuhl, S., Faria, S.H., Azuma, N., Freitag, J., Hamann, I., Kauf-
2292 mann, P., Miller, H., Weiler, K., Wilhelms, F.. Evidence of dynamic
2293 recrystallization in polar firn. *J Geophys Res* 2009;114:B05204.
- 2294 Kipfstuhl, S., Hamann, I., Lambrecht, A., Freitag, J., Faria, S.H.,
2295 Grigoriev, D., Azuma, N.. Microstructure mapping: a new method for
2296 imaging deformation induced microstructural features of ice on the grain
2297 scale. *J Glaciol* 2006;52(178):398–406.
- 2298 Kreher, W.. Residual stresses and stored elastic energy of composites and
2299 polycrystals. *JMechPhys Solids* 1990;38:115–128.
- 2300 Kröner, E.. Berechnung der elastischen Konstanten des Vielkristalls aus
2301 den Konstanten des Einkristalls. *Z Phys* 1958;151:504–518.
- 2302 Kröner, E.. Self-consistent scheme and graded disorder in polycrystal elas-
2303 ticity. *J Phys F: Metal Phys* 1978;8:2261–2267.
- 2304 Ktitarev, D., Gödert, G., Hutter, K.. Cellular automaton model for
2305 recrystallization, fabric, and texture development in polar ice. *Journal of*
2306 *Geophysical Research (Solid Earth)* 2002;107(B8).
- 2307 Lahellec, N., Michel, J., Moulinec, H., Suquet, P.. Analysis of inho-
2308 mogeneous materials at large strains using fast fourier transforms. In:
2309 Miehe, C., editor. *IUTAM Symposium on Computational Mechanics of*
2310 *Solid Materials at Large Strains*. Kluwer Ac. Pub. Dordrecht; 2003. p.
2311 247–258.

- 2312 Lahellec, N., Suquet, P.. Effective behavior of linear viscoelastic compos-
2313 ites: a time-integration approach. *Int J Solids Struct* 2006;44:507–529.
- 2314 Lahellec, N., Suquet, P.. On the effective behavior of nonlinear inelastic
2315 composites: I. Incremental variational principles. *J Mech Phys Solids*
2316 2007;55:1932–1963.
- 2317 Laws, N.. Thermo-statics of composite materials. *J Mech Phys Solids*
2318 1973;21(9).
- 2319 Laws, N., McLaughlin, R.. Self-consistent estimates for the vis-
2320 coelastic creep compliances of composite materials. *Proc R Soc Lond*
2321 1978;A353:251–273.
- 2322 Lebensohn, R.A.. N-site modeling of a 3D viscoplastic polycrystal using
2323 Fast Fourier Transform. *Acta Materialia* 2001;49(14):2723 – 2737.
- 2324 Lebensohn, R.A., Brenner, R., Castelnau, O., Rollett, A.D.. Orientation
2325 image-based micromechanical modelling of subgrain texture evolution in
2326 polycrystalline copper. *Acta Materialia* 2008;56(15):3914 – 3926.
- 2327 Lebensohn, R.A., Castelnau, O., Brenner, R., Gilormini, P.. Study of the
2328 antiplane deformation of linear 2-D polycrystals with different microstruc-
2329 tures. *International Journal of Solids and Structures* 2005;42(20):5441 –
2330 5459.
- 2331 Lebensohn, R.A., Kanjarla, A.K., Eisenlohr, P.. An elasto-viscoplastic
2332 formulation based on fast Fourier transforms for the prediction of mi-
2333 cromechanical fields in polycrystalline materials. *International Journal of*
2334 *Plasticity* 2012;32(0):59 – 69.

- 2335 Lebensohn, R.A., Liu, Y., Ponte-Castañeda, P.. Macroscopic prop-
2336 erties and field fluctuations in model power-law polycrystals: full-field
2337 solutions versus self-consistent estimates. Proc Royal Soc Lond A
2338 2004a;460(2045):1381–1405.
- 2339 Lebensohn, R.A., Liu, Y., Ponte-Castañeda, P.. On the accuracy of the
2340 self-consistent approximation for polycrystals: comparison with full-field
2341 numerical simulations. Acta Materialia 2004b;52(18):5347–5361.
- 2342 Lebensohn, R.A., Montagnat, M., Mansuy, P., Duval, P., Meysson-
2343 nier, J., Philip, A.. Modeling viscoplastic behavior and heterogeneous
2344 intracrystalline deformation of columnar ice polycrystals. Acta Materialia
2345 2009;57(5):1405 – 1415.
- 2346 Lebensohn, R.A., Tomé, C.N.. A self-consistent viscoplastic model: pre-
2347 diction of rolling textures of anisotropic polycrystals. Mat Sci and Engin,
2348 A 1993;175:71–82.
- 2349 Lebensohn, R.A., Tomé, C.N., Ponte-Castañeda, P.. Self-consistent mod-
2350 elling of the mechanical behaviour of viscoplastic polycrystals incorporat-
2351 ing intragranular field fluctuations. Phil Mag 2007;87(28):4287–4322.
- 2352 Letouzé, N., Brenner, R., Castelnau, O., Béchade, J.L., Mathon, M.H..
2353 Residual strain distribution in Zircaloy-4 measured by neutron diffraction
2354 and estimated by homogenization techniques. Scripta Mat 2002;47:595–
2355 599.
- 2356 Lipenkov, V.Y., Barkov, N.I., Duval, P., Pimienta, P.. Crystalline
2357 texture of the 2083m ice core at Vostok Station, Antarctica. J Glaciol
2358 1989;35(121):392–398.

- 2359 Lipenkov, V.Y., Salamatin, A.N., Duval, P.. Bubbly-ice densification in
2360 ice sheets: II. Applications. *J Glaciol* 1997;43(145):397–407.
- 2361 Liu, Y., Gilormini, P., Ponte Castañeda, P.. Variational self-consistent
2362 estimates for texture evolution in viscoplastic polycrystals. *Acta Mater*
2363 2003;51:5425–5437.
- 2364 Liu, Y., Ponte Castañeda, P.. Second-order theory for the effective be-
2365 havior and field fluctuations in viscoplastic polycrystals. *Journal of the*
2366 *Mechanics and Physics of Solids* 2004;52(2):467 – 495.
- 2367 Lliboutry, L., Duval, P.. Various isotropic and anisotropic ices found in
2368 glacier and polar ice caps and their corresponding rheologies. *Annales*
2369 *Geophysicae* 1985;3(2):207–224.
- 2370 Llorens, M.G., Bons, P.D., Griera, A., Gomez-Rivas, E., Evans, L.A.. Sin-
2371 gle layer folding in simple shear. *Journal of Structural Geology* 2012;(0):–.
- 2372 Logé, R., Bernacki, M., Resk, H., Delannay, L., Dignonnet, H., Chastel,
2373 Y., Coupez, T.. Linking plastic deformation to recrystallization in metals
2374 using digital microstructures. *Philosophical Magazine* 2008;88:3691–3712.
- 2375 Long, M., Becker, T.. Mantle dynamics and seismic anisotropy. *Earth and*
2376 *Planetary Science Letters* 2010;297:341–354.
- 2377 Ma, Y., Gagliardini, O., Ritz, C., Gillet-Chaulet, F., Durand, G.,
2378 Montagnat, M.. Enhancement factors for grounded ice and ice shelves
2379 inferred from an anisotropic ice-flow model. *Journal of Glaciology*
2380 2010;56(199):805–812.
- 2381 Mandel, J.. *Mécanique des milieux continus*. Paris, France: Gauthier-
2382 Villars, 1966.

- 2383 Mangeney, A., Califano, F., Castelnau, O.. Isothermal flow of an
2384 anisotropic ice sheet in the vicinity of an ice divide. *J Geophys Res*
2385 1996;101(12):28,189–28,204.
- 2386 Mangeney, A., Califano, F., Hutter, K.. A numerical study of anisotropic,
2387 low Reynolds number, free surface flow of ice sheet modeling. *J Geophys*
2388 *Res* 1997;102(B10):22,749–22,764.
- 2389 Mansuy, P., Meyssonier, J., Philip, A.. Localization of deformation in
2390 polycrystalline ice: experiments and numerical simulations with a simple
2391 grain model. *Computational Materials Science* 2002;25(1-2):142–150.
- 2392 Mansuy, P., Philip, A., Meyssonier, J.. Identification of strain hetero-
2393 geneities arising during deformation of ice. *Ann Glaciol* 2000;30:121–126.
- 2394 Martín, C., Gudmundsson, G.H., Pritchard, H.D., Gagliardini, O.. On
2395 the effects of anisotropic rheology on ice flow, internal structure, and the
2396 age-depth relationship at ice divides. *J Geophys Res* 2009;114:F04001.
- 2397 Masson, R., Bornert, M., Suquet, P., Zaoui, A.. An affine formulation
2398 for the prediction of the effective properties of nonlinear composites and
2399 polycrystals. *Journal of the Mechanics and Physics of Solids* 2000;48(6-
2400 7):1203 – 1227.
- 2401 Masson, R., Zaoui, A.. Self-consistent estimates for the rate-dependent
2402 elastoplastic behaviour of polycrystalline materials. *J Mech Phys Solids*
2403 1999;47:1543–1568.
- 2404 Mathiesen, J., Ferkinghoff-Borg, J., Jensen, M., Levinsen, M., Olesen,
2405 P., Dahl-Jensen, D., Svensson, A.. Dynamics of crystal formation in the
2406 Greenland NorthGRIP ice cores. *Journal of Glaciology* 2004;50:325–328.

- 2407 Mellor, M., Testa, R.. Creep of ice under low stress. *Journal of Glaciology*
2408 1969;8:147–152.
- 2409 Michel, J.C., Moulinec, H., Suquet, P.. Effective properties of composite
2410 materials with periodic microstructure: a computational approach. *Comp*
2411 *Meth Appl Mech Engng* 1999;**172**:109–143.
- 2412 Michel, J.C., Moulinec, H., Suquet, P.. A computational method based on
2413 augmented lagrangians and fast Fourier transforms for composites with
2414 high contrast. *Comput Model Eng Sci* 2000;1:79–88.
- 2415 Michel, J.C., Moulinec, H., Suquet, P.. A computational scheme for linear
2416 and non-linear composites with arbitrary phase contrast. *International*
2417 *Journal for Numerical Methods in Engineering* 2001;52(1-2).
- 2418 Miguel, M.C., Vespignani, A., Zapperi, S., Weiss, J., Grasso, J.R.. Inter-
2419 mittent dislocation flow in viscoplastic deformation. *Nature* 2001;410:667–
2420 671.
- 2421 Miyamoto, A.. Mechanical properties and crystal textures of Greenland
2422 deep ice cores. Ph.D. thesis; Hokkaido University; Sapporo; 1999.
- 2423 Molinari, A., Canova, G., Ahzi, S.. A self-consistent approach of the large
2424 deformation polycrystal viscoplasticity. *Acta Metall* 1987;35:2983–2994.
- 2425 Montagnat, M., Blackford, J.R., Piazzolo, S., Arnaud, L., Lebensohn,
2426 R.A.. Measurements and full-field predictions of deformation hetero-
2427 geneities in ice. *Earth and Planetary Science Letters* 2011;305(1-2):153 –
2428 160.
- 2429 Montagnat, M., Buiron, D., Arnaud, L., Broquet, A., Schlitz, P.,
2430 Jacob, R., Kipfstuhl, S.. Measurements and numerical simulation of

- 2431 fabric evolution along the Talos Dome ice core, Antarctica. *Earth and*
2432 *Planetary Science Letters* 2012;357-358(0):168 – 178.
- 2433 Montagnat, M., Durand, G., Duval, P.. Recrystallization processes in
2434 granular ice. *Supp Issue Low Temperature Science* 2009;68:81–90.
- 2435 Montagnat, M., Duval, P.. Rate controlling processes in the creep of polar
2436 ice, influence of grain boundary migration associated with recrystalliza-
2437 tion. *Earth Planet Sc Lett* 2000;183:179–186.
- 2438 Montagnat, M., Weiss, J., Chevy, J., Duval, P., Brunjail, H., Bastie, P.,
2439 Gil Sevillano, J.. The heterogeneous nature of slip in ice single crystals
2440 deformed under torsion. *Philosophical Magazine* 2006;86(27):4259–4270.
- 2441 Morgan, V.. High-temperature ice creep tests. *Cold Reg Sc Tech*
2442 1991;19:295–300.
- 2443 Moulinec, H., Suquet, P.. A numerical method for computing the overall
2444 response of nonlinear composites with complex microstructure. *Computer*
2445 *Methods in Applied Mechanics and Engineering* 1998;157(1-2):69 – 94.
- 2446 Nebozhyn, M., Gilormini, P., Ponte Castañeda, P.. Variational self-
2447 consistent estimates for cubic viscoplastic polycrystals : the effects of
2448 grain anisotropy and shape. *J Mech Phys Solids* 2001;49:313–340.
- 2449 Nye, J.. Some geometrical relations in dislocated crystals. *Acta Materialia*
2450 1953;1:153–162.
- 2451 Pantleon, W.. Resolving the geometrically necessary dislocation content
2452 by conventional electron backscattering diffraction. *Scripta Materialia*
2453 2008;58(11):994 – 997.

- 2454 Paterson, W.S.B.. The physics of glaciers. Pergamon, Oxford, 1994.
- 2455 Pettit, E.C., Thorsteinsson, T., Jacobson, P., Waddington, E.D.. The role
2456 of crystal fabric in flow near an ice divide. *J Glaciol* 2007;53(181):277–288.
- 2457 Pettit, E.C., Waddington, E.D., Harrison, W.D., Thorsteinsson, T., Els-
2458 berg, D., Morack, J., Zumberge, M.A.. The crossover stress, anisotropy
2459 and the ice flow law at Siple Dome, West Antarctica. *Journal of Glaciol-*
2460 *ogy* 2011;57(201):39–52.
- 2461 Piazzolo, S., Bons, P.D., Jessell, M.W., Evans, L., Passchier, C.W.. Dom-
2462 inance of microstructural processes and their effect on microstructural
2463 development: insights from numerical modelling of dynamic recrystalliza-
2464 tion. *Geol Soc, London, Spec Publ* 2002;200:149–170.
- 2465 Piazzolo, S., Borthwick, V., Griera, A., Montagnat, M., Jessell, M.W.,
2466 Lebensohn, R.A., Evans, L.. Substructure dynamics in crystalline ma-
2467 terials: New insight from in situ experiments, detailed EBSD analysis of
2468 experimental and natural samples and numerical modelling. *Materials*
2469 *Science Forum* 2012;715-716:502–507.
- 2470 Piazzolo, S., Jessell, M.W., Bons, P.D., Evans, L., Becker, J.K.. Numerical
2471 simulations of microstructures using the Elle platform: A modern research
2472 and teaching tool. *Journal of the Geological Society of India* 2010;75:110–
2473 127.
- 2474 Pimienta, P., Duval, P., Lipenkov, V.Y.. Mechanical behaviour of
2475 anisotropic polar ice. In: *International Association of Hydrological Sci-*
2476 *ences, Publication 170. Symposium on The Physical Basis of Ice Sheet*
2477 *Modelling, Vancouver; 1987. p. 57–66.*

- 2478 Placidi, L.. Thermodynamically consistent formulation of induced
2479 anisotropy in polar ice accounting for grain rotation, grain-size evolution
2480 and recrystallization. Ph.D. thesis; Darmstadt University of Technology;
2481 Darmstadt; 2004. Available at <http://elib.tu-darmstadt.de/diss/000614/>.
- 2482 Placidi, L.. Microstructured continua treated by the theory of mixtures.
2483 Ph.D. thesis; University of Rome, La Sapienza; Rome; 2005.
- 2484 Placidi, L., Faria, S.H., Hutter, K.. On the role of grain growth, recrystallization, and polygonization in a continuum theory for anisotropic ice sheets. *Ann Glaciol* 2004;39:49–52.
- 2487 Placidi, L., Greve, R., Seddik, H., Faria, S.H.. Continuum-mechanical, anisotropic flow model, based on an anisotropic flow enhancement factor (CAFFE). *Continuum Mech Thermodyn* 2010;22(3):221–237.
- 2490 Placidi, L., Hutter, K.. An anisotropic flow law for incompressible polycrystalline materials. *Zeitschrift für Angewandte Mathematik und Physik (ZAMP)* 2005;57:160–181. 10.1007/s00033-005-0008-7.
- 2493 Placidi, L., Hutter, K.. Thermodynamics of polycrystalline materials treated by the theory of mixtures with continuous diversity. *Continuum Mechanics and Thermodynamics* 2006;17(6):409–451.
- 2496 Ponte Castañeda, P.. The effective mechanical properties of nonlinear isotropic composites. *J Mech Phys Solids* 1991;39:45–71.
- 2498 Ponte-Castañeda, P., Suquet, P.. Nonlinear composites. *Advance in Applied Mechanics* 1998;34:171–302.

- 2500 Ponte Castañeda, P.. Exact second-order estimates for the effective me-
2501 chanical properties of nonlinear composite materials. *J Mech Phys Solids*
2502 1996;44:827–862.
- 2503 Ponte Castañeda, P.. Second-order homogenization estimates for nonlinear
2504 composites incorporating field fluctuations. I – Theory. *J Mech Phys*
2505 *Solids* 2002;50:737–757.
- 2506 Raabe, D., Becker, R.C.. Coupling of a crystal plasticity finite-element
2507 model with a probabilistic cellular automaton for simulating primary
2508 static recrystallization in aluminium. *Modelling and Simulation in Mate-*
2509 *rials Science and Engineering* 2000;8(4):445.
- 2510 Raabe, D., Roters, F.. Using texture components in crystalplasticity finite
2511 element simulations. *Int J Plasticity* 2004;20:339–361.
- 2512 Ricaud, J.M., Masson, R.. Effective properties of linear viscoelastic het-
2513 erogeneous media: Internal variables formulation and extension to ageing
2514 behaviours. *Int J Solids Struct* 2009;46:1599–1606.
- 2515 Roessiger, J., Bons, P.D., Grier, A., Jessell, M.W., Evans, L., Montag-
2516 nat, M., Kipfstuhl, S., Faria, S.H., Weikusat, I.. Competition between
2517 grain growth and grain size reduction in polar ice. *Journal of Glaciology*
2518 2011;57:942–948.
- 2519 Rolland du Roscoat, S., King, A., Philip, A., Reischig, P., Ludwig, W.,
2520 Flin, F., Meyssonier, J.. Analysis of snow microstructure by means
2521 of x-ray diffraction contrast tomography. *Advances Engineering Materials*
2522 2011;13:128–135.

- 2523 Russell-Head, D.S., Wilson, C.J.L.. Automated fabric analyser system for
2524 quartz and ice. *J Glaciol* 2001;24(90):117–130.
- 2525 Sanchez-Hubert, J., Sanchez-Palencia, E.. Sur certains problèmes
2526 physiques d’homogénéisation donnant lieu à des phénomènes de relax-
2527 ation. *Comptes Rendus Acad Sc Paris* 1978;A286:903–906.
- 2528 Sauter, F., Leclercq, S.. Modeling of the non-monotonous viscoplastic
2529 behavior of uranium dioxide. *J Nucl Mater* 2003;322:1–14.
- 2530 Schmatz, J.. Grain boundary – fluid inclusion interaction in rocks and
2531 analogues. Ph.D. thesis; RWTH-Aachen, Germany; 2010.
- 2532 Schulson, E.M., Duval, P.. *Creep and Fracture of Ice*. Cambridge University
2533 Press, 2009.
- 2534 Seddik, H., Greeve, R., Placidi, L., Hamann, I., Gagliardini, O.. Applica-
2535 tion of a continuum-mechanical model for the flow of anisotropic polar ice
2536 to the EDML core, Antarctica. *Journal of Glaciology* 2008;54(187):631–
2537 642.
- 2538 Seddik, H., Greve, R., Zwinger, T., Gillet-Chaulet, F., Gagliardini, O..
2539 Simulations of the Greenland ice sheet 100 years into the future with the
2540 full Stokes model Elmer/Ice. *J Glaciol* 2012;58(209):427–440.
- 2541 Seddik, H., Greve, R., Zwinger, T., Placidi, L.. A full stokes ice flow
2542 model for the vicinity of Dome Fuji, Antarctica, with induced anisotropy
2543 and fabric evolution. *The Cryosphere* 2011;5(2):495–508.
- 2544 Solas, D., Gerber, P., Baudin, T., Penelle, R.. Monte Carlo method
2545 for simulating grain growth in 3D. influence of lattice site arrangements.
2546 *Materials Science Forum* 2004;467 - 470:1117–1122.

- 2547 Sotin, C., Tobie, G., J., W.. Europa after Galileo; The University of
2548 Arizona Press, Tucson, AZ. p. 85–118.
- 2549 Suquet, P.. In: Sanchez-Palencia, E., Zaoui, A., editors. Homogenization
2550 Techniques for Composite Media. Springer Berlin / Heidelberg; volume
2551 272 of *Lecture Notes in Physics*; 1987. p. 193–198.
- 2552 Suquet, P., Moulinec, H., Castelnau, O., Montagnat, M., Lahellec, N.,
2553 Grennerat, F., Duval, P., Brenner, R.. Multi-scale modeling of the
2554 mechanical behavior of polycrystalline ice under transient creep. *Proceeda*
2555 *IUTAM 2011*;In press.
- 2556 Taupin, V., Richeton, T., Chevy, J., Fressengeas, C., Weiss, J., Louchet,
2557 F., Miguel, M.. Rearrangement of dislocation structures in the aging of
2558 ice single crystals. *Acta Materialia* 2008;56(7):1555 – 1563.
- 2559 Taupin, V., Varadhan, S., Chevy, J., Fressengeas, C., Beaudoin, A.J.,
2560 Montagnat, M., Duval, P.. Effects of size on the dynamics of dislocations
2561 in ice single crystals. *Phys Rev Lett* 2007;99(15):155507.
- 2562 Taylor, G.. Plastic strain in metals. *J Inst Met* 1938;62:307–324.
- 2563 Thorsteinsson, T.. Fabric development with nearest-neighbor interaction
2564 and dynamic recrystallization. *J Geophys Res* 2002;107(B1).
- 2565 Thorsteinsson, T., Kipfstuhl, J., Miller, H.. Textures and fabrics in the
2566 GRIP ice core. *J Geophys Res* 1997;102(C12):26,583–26,600.
- 2567 Tommasi, A., Knoll, M., Vauchez, A., Signorelli, J., Thoraval, C., Logé,
2568 R.. Structural reactivation in plate tectonics controlled by olivine crystal
2569 anisotropy. *Nature Geoscience* 2009;2(6):423–427.

- 2570 Urai, J., Means, W., Lister, G.. Dynamic recrystallization of minerals.
2571 In: Mineral and Rock Deformation: Laboratory Studies. Hobbs, B.E. and
2572 Heard, H.C.; Geophysical Monograph; 1986. p. 161–200.
- 2573 Vacher, P., Dumoulin, S., Morestin, F., Mguil-Touchal, S.. Bidimensional
2574 strain measurement using digital images. Proceedings of the Institution of
2575 Mechanical Engineers, Part C: Journal of Mechanical Engineering Science
2576 1999;213(8):811–817.
- 2577 Van der Veen, C.J., Whillans, I.M.. Flow law for glacier ice: comparison
2578 of numerical predictions and field measurements. Journal of Glaciology
2579 1990;36:324–339.
- 2580 Van der Veen, C.J., Whillans, I.M.. Development of fabric in ice. Cold
2581 Reg Sci Technol 1994;22(2):171–195.
- 2582 Varadhan, S., Beaudoin, A., Fressengeas, C.. Coupling the dynamic of
2583 statistically distributed and excess dislocations. Proc of Science 2006;SM-
2584 PRI2005, 004:1–11.
- 2585 Verdier, M., Fivel, M., Groma, I.. Mesoscopic scale simulation of disloca-
2586 tion dynamics in fcc metals: principles and applications. Modelling Simul
2587 Mat Sci Eng 1998;6:755–770.
- 2588 Vu, Q.H., Brenner, R., Castelnau, O., Moulinec, H., Suquet, P.. A
2589 self-consistent estimate for linear viscoelastic polycrystals with internal
2590 variables inferred from the collocation method. Modelling and Simulation
2591 in Materials Science and Engineering 2012;20(2):024003.
- 2592 Weertman, J.. Creep of ice. In: Whalley, E., Jones, S., Gold, L.,

- 2593 editors. *Physics and Chemistry of Ice*. Roy. Soc. Canada, Ottawa; 1973.
2594 p. 320–337.
- 2595 Weikusat, I., Kipfstuhl, S., Faria, S.H., Azuma, N., Miyamoto, A.. Sub-
2596 grain boundaries and related microstructural features in EDML (Antarc-
2597 tica) deep ice cores. *J Glaciol* 2009;55(191):461–472.
- 2598 Weiss, J., Grasso, J.R.. Acoustic emission in single crystals of ice. *Journal*
2599 *of Physical Chemistry B* 1997;101(32):6113–6117.
- 2600 Weiss, J., Grasso, J.R., Miguel, M.C., Vespignani, A., Zapperi, S..
2601 Complexity in dislocation dynamics: experiments. *Materials Science and*
2602 *Engineering: A* 2001;309–310(0):360 – 364. *Dislocations 2000: An Inter-*
2603 *national Conference on the Fundamentals of Plastic Deformation*.
- 2604 Weiss, J., Marsan, D.. Three-dimensional mapping of dislo-
2605 cation avalanches: Clustering and space/time coupling. *Science*
2606 2003;299(5603):89–92.
- 2607 Weiss, J., Miguel, M.C.. Dislocation avalanche correlations. *Materials*
2608 *Science and Engineering A* 2004;387-389:292 – 296. *13th International*
2609 *Conference on the Strength of Materials*.
- 2610 Weiss, J., Montagnat, M.. Long-range spatial correlations and scaling in
2611 dislocation and slip patterns. *Philosophical Magazine* 2007;87(8-9):1161–
2612 1174.
- 2613 Wenk, H.R., Canova, G., Bréchet, Y., Flandin, L.. A deformation-
2614 based model for recrystallization of anisotropic materials. *Acta Mater*
2615 1997;45(8):3283–3296.

- 2616 Willis, J.R.. Variational and related methods for the overall properties of
2617 composites. *Adv Appl Mech* 1981;21:2–78.
- 2618 Wilson, C., Burg, J., Mitchell, J.. The origin of kinks in polycrystalline
2619 ice. *Tectonophysics* 1986;127:27–48.
- 2620 Wilson, C., Zhang, Y.. Comparison between experiment and com-
2621 puter modelling of plane strain simple shear ice deformation. *J Glaciol*
2622 1994;40(134):46–55.
- 2623 Zhang, Y., Jenkins, J.T.. The evolution of the anisotropy of a polycrys-
2624 talline aggregate. *J Mech Phys Solids* 1993;41:1213–1243.

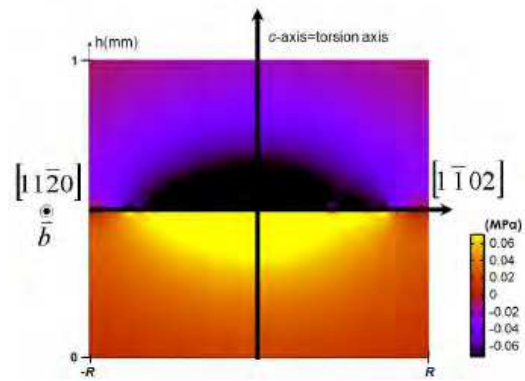


Figure 1: Map of the resolved shear stress in the prismatic system for a torsion boundary made of basal screw dislocations. The cylinder diameter is 1 mm, and the maximum applied stress is 0.1 MPa. From (Chevy et al., 2012)

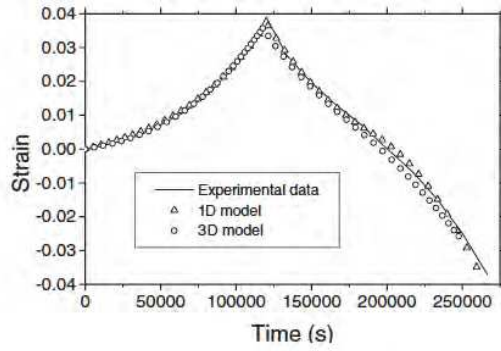


Figure 2: Creep curves in forward and reverse torsion from experiments on single crystals, obtained by 1D and 3D FDM models. From (Taupin et al., 2007)

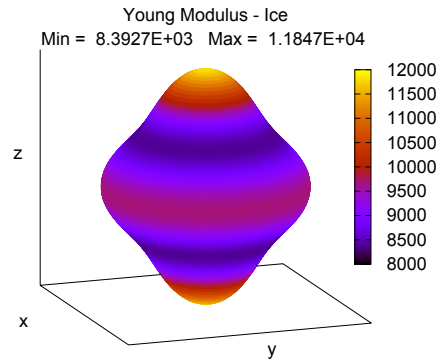


Figure 3: Young's modulus in [MPa] of an ice single crystal with its c-axis aligned with z, at -16°C .

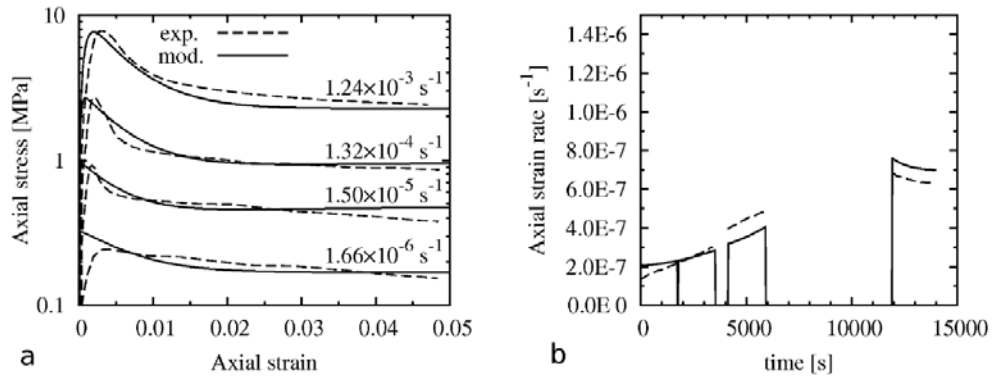


Figure 4: Behavior of an ice single crystal deformed by basal slip. a) Predictions of the model, based on Eq. (6) and with parameters given in Table 1, in comparison with the experimental data of Weertman (1973). Axial strain rates are indicated. b) Prediction of the model in comparison with the results of the recovery tests of Taupin et al. (2008). Temperature is -10°C . From (Suquet et al., 2011)

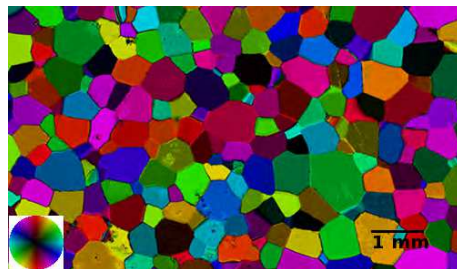


Figure 5: Typical 2D microstructure of an ice polycrystal grown in the laboratory. The color wheel gives the color-code for the c-axis orientation.

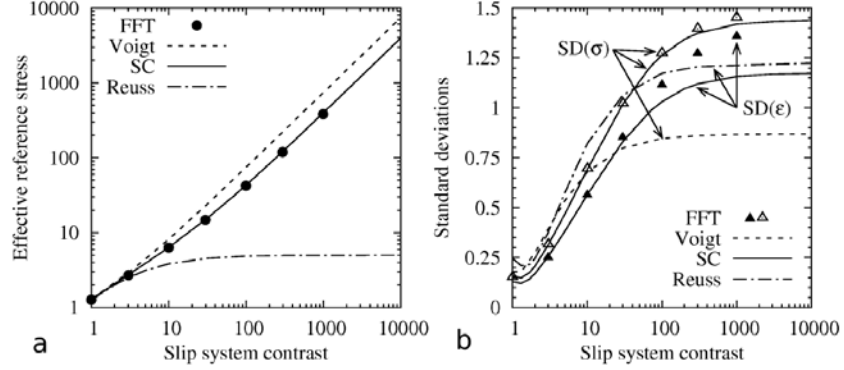


Figure 6: Full-field vs. mean-field behavior for ice polycrystals with random fabric, for a linear viscous behavior ($n = 1$) and various viscoplastic anisotropy (or slip system contrasts) at the grains level. a) Effective flow stress $\bar{\sigma}_0$. b) Standard deviation of equivalent stress and strain rate, normalized by $\bar{\sigma}_{eq}$ and $\bar{\dot{\epsilon}}_{eq}$, respectively, characterizing field heterogeneities at the polycrystal scale. Results from the linear SC scheme are compared to reference numerical solutions provided by the FFT approach. Reuss and Voigt bounds are also indicated. Note that, for these bounds, standard deviations of stress and strain rate, respectively, do vanish.

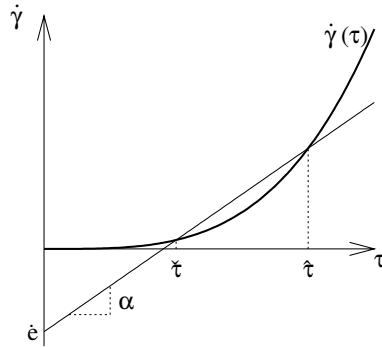


Figure 7: Schematic representation of the linearization between the shear rate ($\dot{\gamma}$) and the stress (τ), to illustrate Eq. (21).

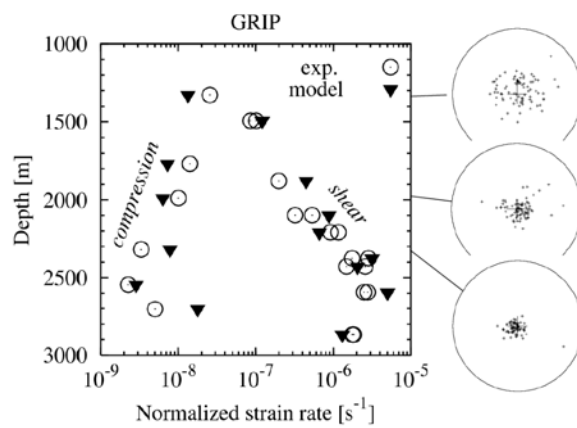


Figure 8: Stationary creep behavior at -10°C calculated by the affine SC model, and compared to experimental data obtained on anisotropic specimens from the GRIP ice core. The c -axis pole figures on the right show an increasing concentration of c -axes towards the *in situ* vertical direction from the surface of the ice sheet down to $\sim 2600\text{m}$ depth. Experimental data from Castelnau et al. (1998) are expressed for a stress of 1MPa using a stress sensitivity $n = 3$. Points on the left hand side reflect the (hard) behavior under vertical compression, whereas data on the right correspond to (soft) horizontal shear.

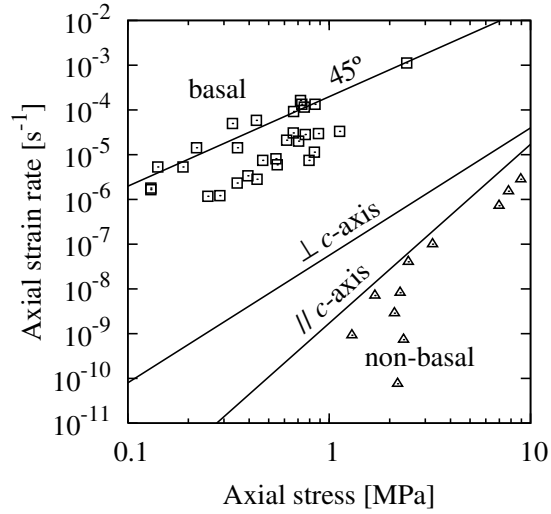


Figure 9: Stationary creep behavior of single crystals at -10°C input in the AFF SC model to get results of Fig. 8 (lines), compared to the data set compiled by Duval et al. (1983) (symbols). Results are indicated for uniaxial compression at 45° from the c -axis (activation of basal slip), as well as for compression perpendicular (activation of prismatic slip) and parallel (activation of pyramidal systems) to the c -axis. From (Castelnau et al., 2008b)

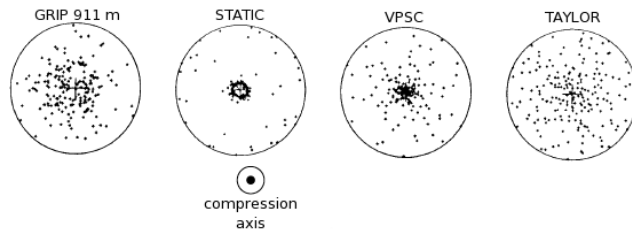


Figure 10: Comparison between fabrics measured along the GRIP ice core (911 m depth), simulated by the static (Reuss), VPSC-tangent, and Taylor (Voigt) approaches.

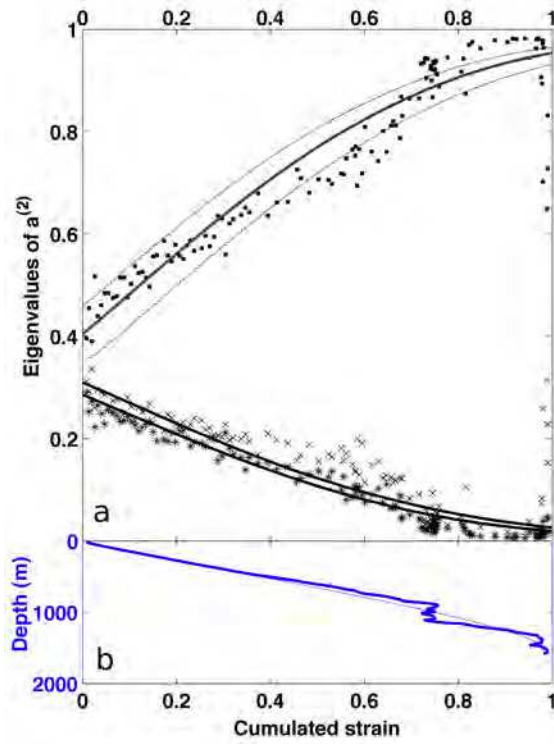


Figure 11: a) Evolution of the eigenvalues of the orientation tensor $\mathbf{a}^{(2)} = \mathbf{c} \otimes \mathbf{c}$ of the fabric along the Talos Dome ice core, as a function of the cumulated compressive strain. Lines = VP-SO model results, dashed line represents the range of fabric evolution modeled with variation of the initial orientation tensor eigenvalue from isotropic (bottom line), as measured at 18 m (central line), more concentrated than measured (top line). Dots, crosses and plus = measurements performed with the Automatic Ice Texture Analyzer (Russell-Head and Wilson, 2001). b) Cumulated in-situ compressive strain as a function of depth as model by the TALDICE-1 chronology (full line) (Buiron et al., 2011).

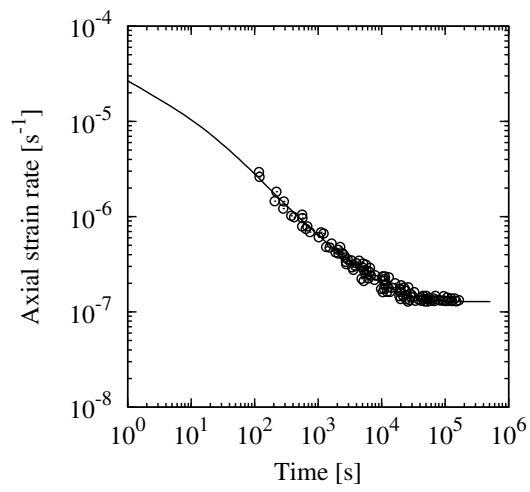


Figure 12: Transient creep response of isotropic ice under an uniaxial compressive stress of 1 MPa predicted with the affine elasto-viscoplastic extension of the self-consistent scheme (line). Model results are compared to the data of Ashby and Duval (1985), expressed for the same loading conditions (points). Strain hardening of prismatic and pyramidal slip systems is taken into account. From (Castelnau et al., 2008b)

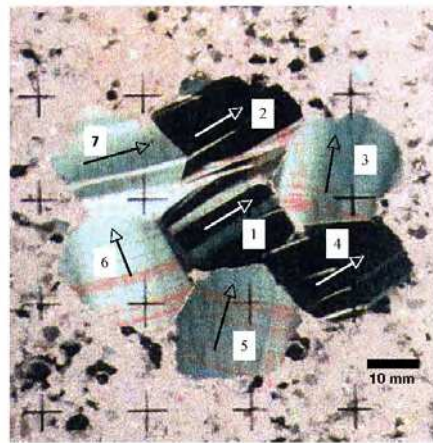


Figure 13: Photograph of a compression creep specimen (after (Mansuy et al., 2000)) between crossed polarizers, after a deformation of 6.6×10^{-2} at -10°C . The corresponding strain rate was $6.0 \times 10^{-8} \text{ s}^{-1}$. The compression direction is vertical in the plane of the photograph. The mean size of each hexagonal grain was 20 μm . Black and white arrows indicate the initial c-axis orientations. Kink bands appear as abrupt changes in color parallel to the c-axis, shear bands are perpendicular to the c-axis direction.

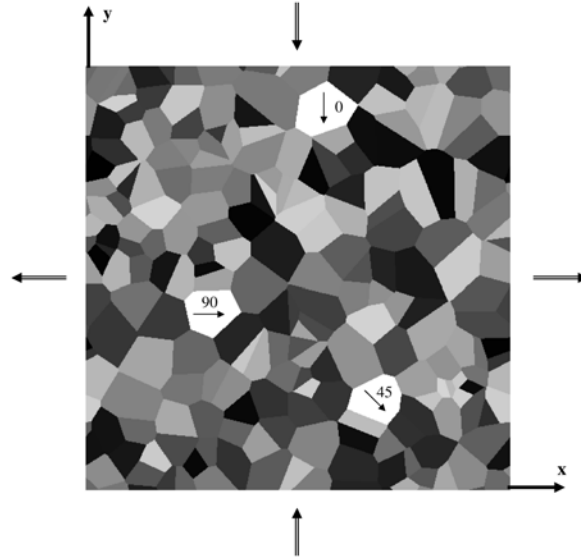


Figure 14: Unit cell containing the cross-sections of 200 columnar grains generated by Voronoi tessellation. The three hand-picked orientations: $(0^\circ, 90^\circ, 0^\circ)$, $(45^\circ, 90^\circ, 0^\circ)$ and $(90^\circ, 90^\circ, 0^\circ)$, and the extension and shorting directions are also indicated.

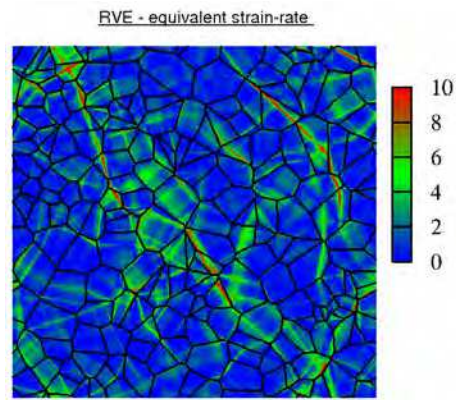


Figure 15: Predicted equivalent strain-rate field over the entire unit cell of Fig. 14, normalized with respect to the average equivalent strain rate ($\dot{\epsilon}_{eq} = 1.15 \times 10^{-8} \text{s}^{-1}$).

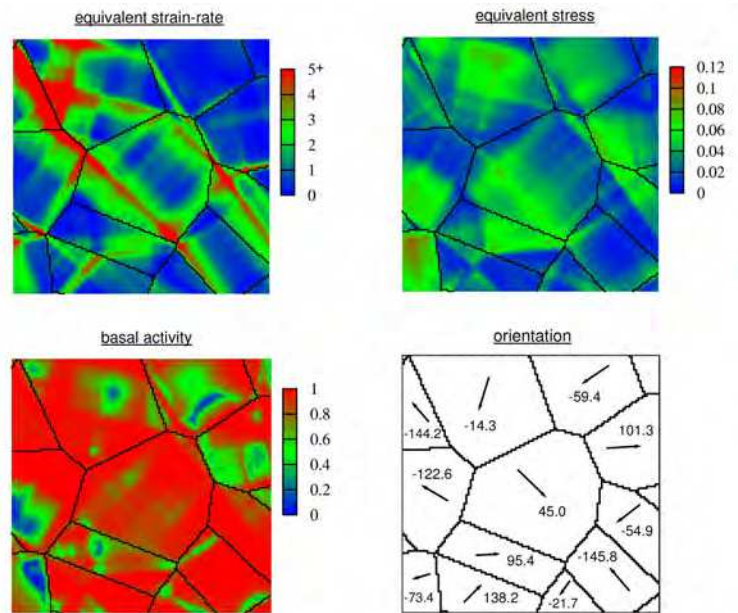


Figure 16: Predicted fields of equivalent strain rate (normalized to $\dot{\epsilon}_{eq}$), equivalent stress (in units of τ^{bas}), relative basal activity, and map of neighbor orientations, for the 45 deg grain and its surroundings.

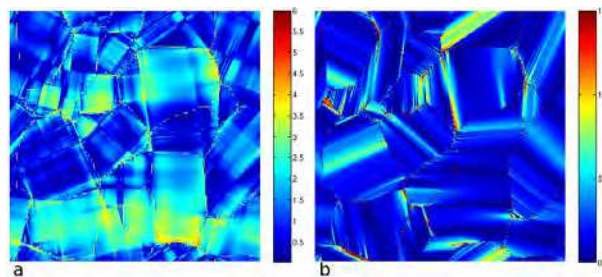


Figure 17: a) Predicted equivalent stress field (in units of τ^{bas}), and b) the misorientation, compared with initial orientation, obtained after 1% strain in a laboratory made microstructure. From (Montagnat et al., 2011)

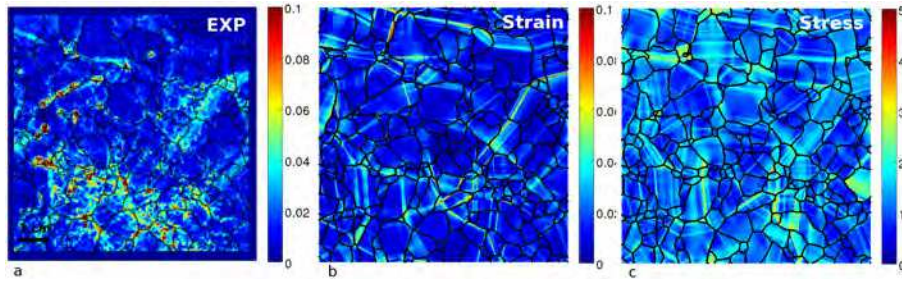


Figure 18: a) Strain field measured experimentally, b) simulated, and c) stress field simulated, after 0.85 % of axial compression. Experimental resolution is about 75×75 pixels, the modeling one is 1024×1024 pixels. From (Grennerat et al., 2012)

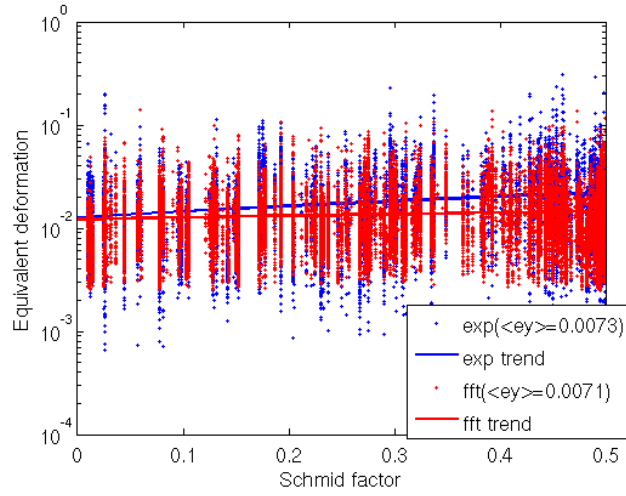


Figure 19: Equivalent strain as a function of the Schmid factor (as a proxy of the orientation). Experimental results are in blue, modeling results in red. Each point is one pixel of the microstructure. The macroscopic strain was 0.7%. From (Grennerat et al., 2012)

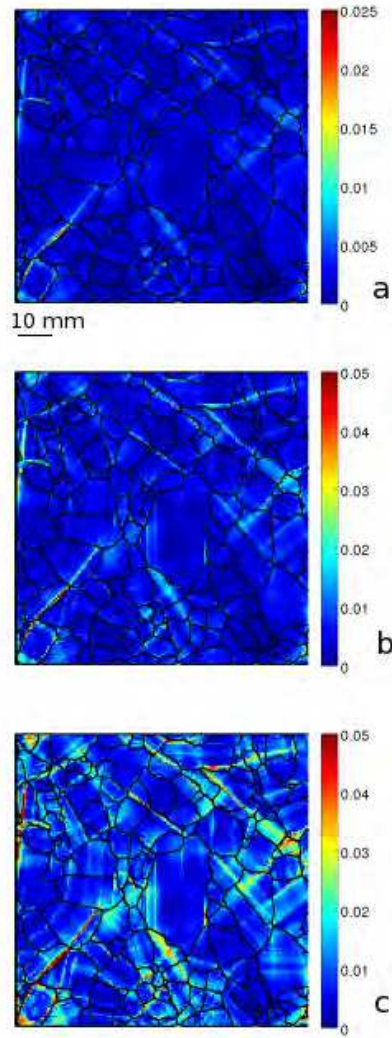


Figure 20: Evolution of the FFT-simulated equivalent strain field during the transient creep of a "2D-1/2" sample of ice, after (a) 0.15%, (b) 0.35% and (c) 0.60% compressive strain (see Grennerat et al. (2012)).

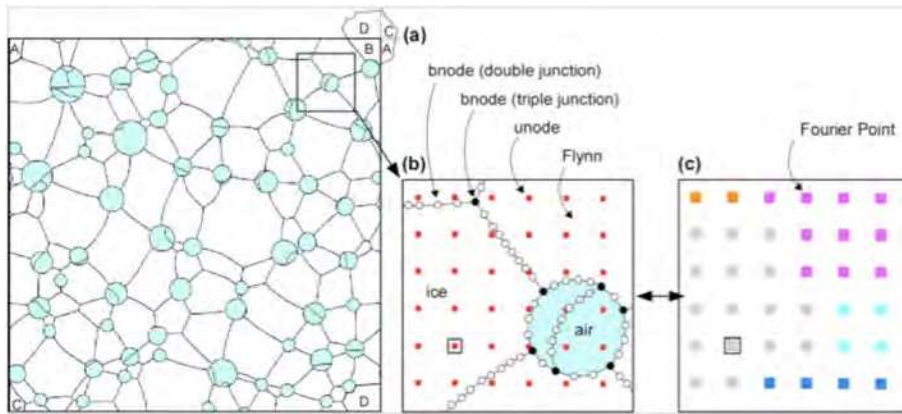


Figure 21: (a) Example of an Elle model: ice (white) with air bubbles (pale blue) (Roesiger et al., this volume). The Elle model has fully wrapping boundaries and grains A to D are in fact one single grain. (b) Close-up showing that grains are defined by flynns (polygons), themselves defined by straight segments that connect boundary nodes (bnodes). A second layer of unconnected nodes (unodes) can be added to keep track of material points. (c) For the FFT module, the microstructure is discretized into a periodic, regular mesh of Fourier Points defined by a characteristic lattice orientation. A direct mapping between unodes layer and Fourier points is established between both codes.

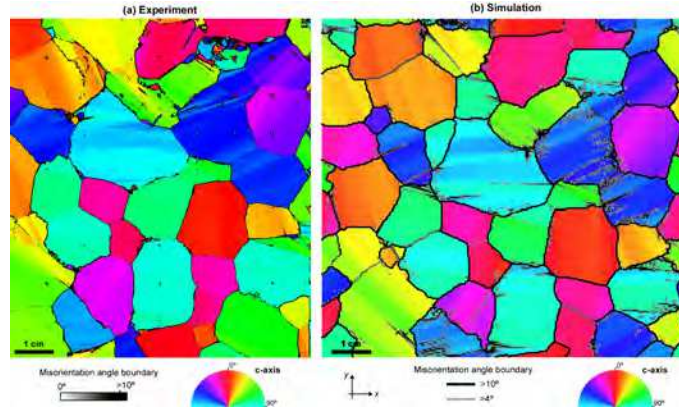


Figure 22: Comparison of (a) physical experiment and (b) numerical simulation after a vertical shortening of 4%. A qualitative equivalence between experiment and simulations is observable, such as correspondence of kink-bands or discontinuous subgrain boundaries at sharp grain boundaries asperities. Colors indicate the orientation of the c-axis respect to the sample reference. Misorientation angle between nodes are indicated in grey ($> 4^\circ$) and black ($> 10^\circ$). Triangular patches seen in the experiment are due to erroneous misfit during Automatic Ice Texture Analyzer acquisition.

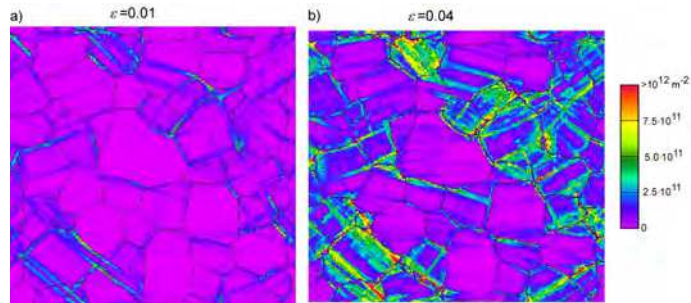


Figure 23: Dislocation density maps after (a) 1% and (b) 4% of shortening. Grain microstructure is indicated by dark lines. Serrated and bulging grain boundaries develop due to grain boundary migration into regions of high dislocation density. New recrystallized grains develop preferentially at triple points and along grain boundaries. Low dislocation densities are typically observed at bulge areas and new grains.

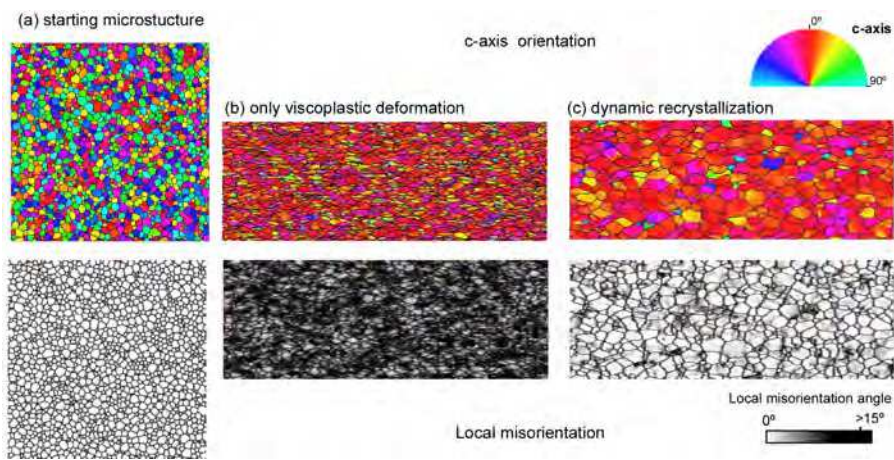


Figure 24: Numerical simulation of polar ice microstructure using the FFT/Elle scheme. (a) Starting microstructure. (b) 40% vertical shortening with only viscoplastic deformation. (c) 40% shortening with viscoplastic deformation coupled with recrystallization. Top row shows c-axis orientations in color and local misorientation in grey. Bottom row shows local misorientation only. C-axis orientation distributions are shown in lower-hemisphere stereoplots.

	τ_{ini}	τ_{sta}	$\dot{\gamma}_0$	n	c	d	e
Basal	0.1	0.022	10^{-6}	2	9	60	0.0003
Prismatic	0.13	1.5	10^{-6}	2.85	9	60	0.0003
Pyramidal	3.875	3.875	10^{-6}	4	9	60	0.0003

Hardening matrix:

	Basal	Prismatic	Pyramidal
Basal	70	125	0
Prismatic	125	110	0
Pyramidal	0	0	0

Table 1: Material parameters used in the full-field simulations for single crystals of ice at $-10^\circ C$. Units are MPa and s^{-1} .

Model	Scale	Type	Applications	Advantages	Limitations
DD	Single crystal (mesoscopic)	Finite Element (FE)	Dislocation dynamics and interactions	Solve physics of plasticity at the dislocation scale - Provide slip system activities and interactions	Computing time-intensive. Small samples. Simplified configurations
FDM	Single to poly-crystal	Full-field (FE)	Plasticity modeling taking into account heterogeneous internal stress field associated with dislocations	Length scaling, makes the link between the complexity of the dislocation field dynamics and the macroscopic behavior - Provide intra-crystalline fields	Computing time-intensive - Limited number of grains
VPSC	Polycrystal	Mean-field	Provides effective visco-plastic behavior of polycrystals, based on a given single-crystal behavior	Texture-induced polycrystal anisotropy, texture evolution for secondary creep, can reach large strains	Very limited information on intra-crystalline fields, elasticity and recrystallization neglected
EVPC	Polycrystal	Mean-field	Provides effective elasto-visco-plastic behavior at polycrystal level, based on known single-crystal behavior	Captures texture-induced anisotropy during transient creep regime	Very limited information on intra-crystalline fields, limited to small strains

Table 2: Summary of techniques application domains, interest and limitations. DD: Dislocation Dynamics, FDM: Field Dislocation Mechanics, VPSC: Homogenized Polycrystal Visco-Plasticity, EVPC: Homogenized Polycrystal Elasto-Visco-Plasticity

Model	Scale	Type	Applications	Advantages	Limitations
VPSC + DRX	Polycrystal	Mean-field	DRX mechanisms with phenomenological laws, fabric evolution	Fast to run for high strain - easily adaptable to various DRX laws	Too simplified description of DRX mechanisms. No account for intra-crystalline fields
VPFFT	Polycrystal	Full-field	Provides effective visco-plastic behavior and local intra- crystalline fields, 2D and 3D	Microstructural effects on local fields distribution in the secondary creep regime	Microstructure evolution at large strains can only be captured in a crude way. No elasticity and DRX
EVPFFT	Polycrystal	Full-field	Provides effective elasto-visco-plastic behavior and local intra-crystalline fields, 2D and 3D	Microstructural effects on local fields distribution and their evolution during transient creep	Limited to small strains, no microstructure evolution yet, no DRX
VPFFT - Elle	Polycrystal	Full-field	Provides local intra-crystalline fields and microstructure evolution in 2D	Couple local field predictions to DRX mechanisms in the secondary creep regime	No account for local field evolution during transient creep. Limited to 2D (Elle). Rough update of the dislocation field during DRX

Table 3: Summary of techniques application domains, interest and limitations. DRX: dynamic recrystallization, VPFFT: FFT-based formulation for Visco-Plastic polycrystals , EVPFFT: FFT-based formulation for Elasto-Visco-Plastic polycrystals

Model	Scale	Type	Applications	Advantages	Limitations
Mixture with Continuous Diversity (MCD)	Large scale	General continuum theory	General overview of the interactions between microstructure evolution, DRX and ice flow	Effects of microstructure and its evolution via internal variables. Secondary and tertiary creep regimes. Thermodynamically consistent	Mathematically complex. Not implemented numerically yet
CAFEE	Large Scale	Continuum model	Provides effective visco-plastic behavior on the large scale, including fabric development	Captures the effects of fabric development in the secondary and tertiary creep regimes, easy to implement	Stress and strain rate are colinear (scalar effective viscosity). Limited to fabrics represented by a multipole expansion up to fourth order only.
GOLF law	Polycrystal	Phenomenological orthotropic non-linear law	Provides orthotropic viscous behavior and fabric development	Efficient, easy-to-use and able to reproduce the response of micro-macro models	Orthotropic fabric restricted to the assumed closure approximation. Non-linear case not validated against micro-macro models yet
Elmer/Ice	Large scale	FE code including GOLF and CAFEE law	Flow of anisotropic polar ice and its fabric evolution	Fabric evolution consistent with the stress field and strain-rate field	Can not be used to simulate the localization of the deformation (diffusion of the fabric induced by interpolation)

Table 4: Summary of techniques application domains, interest and limitations. DRX: dynamic recrystallization